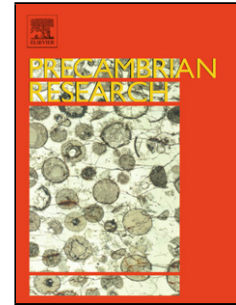


## Accepted Manuscript

Title: Palaeotectonic setting of the south-eastern Kédougou-Kéniéba Inlier, West Africa: new insights from igneous trace element geochemistry and U-Pb zircon ages

Author: James S. Lambert-Smith David M. Lawrence  
Wolfgang Müller Peter J. Treloar



PII: S0301-9268(15)00348-4  
DOI: <http://dx.doi.org/doi:10.1016/j.precamres.2015.10.013>  
Reference: PRECAM 4384

To appear in: *Precambrian Research*

Received date: 14-1-2015  
Revised date: 7-10-2015  
Accepted date: 17-10-2015

Please cite this article as: Lambert-Smith, J.S., Lawrence, D.M., Müller, W., Treloar, P.J., Palaeotectonic setting of the south-eastern Kédougou-Kéniéba Inlier, West Africa: new insights from igneous trace element geochemistry and U-Pb zircon ages, *Precambrian Research* (2015), <http://dx.doi.org/10.1016/j.precamres.2015.10.013>

This is a PDF file of an unedited manuscript that has been accepted for publication. As a service to our customers we are providing this early version of the manuscript. The manuscript will undergo copyediting, typesetting, and review of the resulting proof before it is published in its final form. Please note that during the production process errors may be discovered which could affect the content, and all legal disclaimers that apply to the journal pertain.

1 Palaeotectonic setting of the south-eastern Kédougou-Kéniéba Inlier, West  
2 Africa: new insights from igneous trace element geochemistry and U-Pb  
3 zircon ages

4 James S. Lambert-Smith<sup>1\*</sup>; David M. Lawrence<sup>2</sup>; Wolfgang Müller<sup>3</sup>; Peter J. Treloar<sup>1</sup>

5 <sup>1</sup>School of Geography, Geology and the Environment, Kingston University London, Kingston upon  
6 Thames, Surrey, KT1 2EE, UK

7 <sup>2</sup>Randgold Resources Ltd, 3rd Floor, Unity Chambers, 28 Halkett Street, St Helier, Jersey, JE24W

8 <sup>3</sup>Department of Earth Sciences, Royal Holloway, University of London, Egham, Surrey, TW20 0EX

9 \*Corresponding author (Telephone: +44 (0) 208417 9000 Ext. 62880; Email: J.S.Lambert-  
10 Smith@kingston.ac.uk)

11 Abstract

12 New U-Pb zircon ages and geochemistry from the eastern Kédougou-Kéniéba Inlier are presented and  
13 integrated with published data to generate a revised tectonic framework for the westernmost Birimian  
14 terranes. The Falémé Volcanic Belt and Kofi Series are highly prospective, hosting several multi-million ounce  
15 gold deposits and a significant iron ore resource, but remain under-researched. It is therefore important to  
16 constrain the fundamental geological setting.

17 The igneous rocks of the eastern Kédougou-Kéniéba Inlier are dominantly of high-K calc-alkaline affinity,  
18 with fractionated REE patterns and negative Nb-Ta anomalies. The plutonic rocks in the Falémé Belt are  
19 dioritic to granodioritic in composition, with moderately fractionated REE patterns and metaluminous A/CNK  
20 signatures. Felsic, peraluminous granite stocks, dykes and plutons with fractionated REE patterns and  
21 negative Eu, Ti and P anomalies intruded both the Falémé Belt and Kofi Series. Albitisation masks the affinity

22 of some units, although use of the Th-Co diagram shows that prior to albitisation, all igneous units belonged  
23 to the high-K calc-alkaline series. New U-Pb age data for the Boboti and Balangouma plutons indicate  
24 crystallisation at  $2088.5 \pm 8.5$  Ma and at  $2112 \pm 13$  Ma, respectively. Inherited zircons in the Boboti pluton  
25 indicate magmatic activity in the Falémé Belt at  $2218 \pm 83$  Ma coincided with the oldest dated units in the  
26 Mako Belt to the West.

27 Systematic changes in Dy/Yb, Sm/La, Nb/Zr, Rb concentration, Eu-anomaly and  $\epsilon\text{Nd}_t$  over  $\sim 200$  Ma reveal  
28 that the tectonic setting in the KKI evolved from a volcanic island arc environment to an active continental  
29 margin. Crustal thickening, as a result of a shift to collisional tectonic setting, combined with magmatic  
30 differentiation, led to the generation of peraluminous, granitic melts with a significant crustal component. A  
31 small suite of more basic intrusive and extrusive rocks on the eastern margin of the Dialé-Daléma basin are  
32 highly metaluminous and display limited LILE enrichment, with normalised HREE values close to unity. The  
33 Daléma igneous rocks may have formed in an extensional back arc, related to the arc system.

## 34 Key Words

35 Kédougou-Kéniéba Inlier; Birimian; geochemistry; U-Pb zircon ages; palaeotectonic setting

## 36 1 Introduction

37 The Birimian terranes of the West African Craton are considered to be an important record of crustal  
38 growth in the Palaeoproterozoic (Boher et al., 1992; Doumbia et al., 1998; Gasquet et al., 2003). The exact  
39 tectonic setting and geodynamic processes that gave rise to the Birimian terranes remain a subject of  
40 debate. In part this is because of the complex nature of the terranes, but also due to gaps in the geochemical  
41 and chronological datasets. The Kédougou-Kéniéba Inlier (KKI; Figure 1) represents the westernmost outcrop  
42 of the Birimian in the Leo-Man shield, and is separated from the majority of the Palaeoproterozoic terranes  
43 by the overlying Neoproterozoic sandstones of the Taoudeni Basin. The western part of the KKI is well  
44 studied, with most attention given to the Mako Volcanic Belt (MVB; Figure 1) in Eastern Senegal (e.g., Debat

45 et al., 1984; Abouchami et al., 1990; Ledru et al., 1991; Dia, et al., 1997; Diallo, 2001; Gueye et al., 2008;  
46 Ngom et al., 2009; Treloar et al., 2014). By comparison, the eastern KKI (the Falémé Volcanic Belt and Kofi  
47 Series; Figure 1) is under-researched, despite hosting several world-class Au deposits, including the Loulo,  
48 Goukoto, Sadiola and Tabakoto gold mines all of which are situated east of the Senegal-Mali Shear Zone  
49 (SMSZ; Bassot and Dommaget, 1986; Dommaget et al., 1993; Lawrence et al., 2013a and b). In addition to  
50 Au mineralisation, several magnetite-skarn deposits are hosted in the Falémé Volcanic Belt (FVB; Schwartz  
51 and Melcher, 2004). The KKI is clearly a highly prospective region in the Birimian; it is therefore important to  
52 constrain the fundamental geological setting.

53 The majority of geochemical studies in the KKI have focused on the tholeiitic lavas and belt-hosted  
54 granitoid plutons in the MVB (Debat et al., 1984; Abouchami et al., 1990; Boher et al., 1992; Diallo, 2001;  
55 Pawlig et al., 2006). Schwartz and Melcher (2004) published a geochemical study of the FVB, which  
56 concentrated on the genesis of the skarn-style iron ore deposits. However, neither the extensive  
57 Balangouma pluton in the north of the belt (Figure 2), or the numerous minor stocks and dykes throughout  
58 the FVB and Kofi Series have been studied geochemically. These lithologies are dominantly unaltered by  
59 hydrothermal processes, with well-preserved primary textures, despite greenschist facies metamorphism.  
60 However, some rocks in the area have been albitised due to hydrothermal fluid-rock interactions. This may  
61 hide the true tectonic and petrogenetic affinity of these lithologies, leading to incorrect conclusions as to  
62 their genesis.

63 Here we use new geochronological and geochemical datasets, combined with published data, to  
64 construct an improved geotectonic framework for the KKI, with an emphasis on the Falémé Volcanic Belt and  
65 Kofi Series. We aim to integrate trace element geochemistry with geochronology to show the secular  
66 evolution of Birimian magmas from primitive island arc granitoids to evolved syn-collisional granites. This  
67 reflects the shift from an ocean island arc setting to an accretionary regime with associated crustal  
68 thickening. In addition we aim to examine the key geochemical characteristics of altered igneous lithologies

69 and show that Na-rich igneous rocks in the KKI are the product of albitisation of high-K calc-alkaline  
70 lithologies.

## 71 2 Geology of the Birimian of West Africa

72 The West African Craton (WAC) consists of Archaean and Palaeoproterozoic terranes; stable since ~2 Ga,  
73 they provide a valuable record of crustal growth processes and contain notable mineral wealth. The WAC is  
74 divided into three domains: 1) The Reguibat Rise in northern Africa; 2) The Leo-Man Rise in sub-Saharan  
75 West Africa and, 3) The Kayes and Kédougou-Kéniéba Inliers in the Sahel region, North West of the Leo-Man  
76 Rise. The Reguibat and Leo-Man rises both share contacts with Archaean continental nuclei and are  
77 collectively referred to as the Baoulé-Mossi Domain. The Birimian terranes consist of narrow, linear to  
78 arcuate, N to NNE trending volcanic belts, separated by broad sedimentary basins. The volcanic rocks are  
79 interpreted to be the base of the sequence, with coeval to slightly younger metasedimentary rocks (Béziat et  
80 al., 2000; Pouclet et al, 2006; Roddaz et al., 2007). The terranes were accreted and cratonised during a  
81 period of SE to NW directed crustal shortening, metamorphism and magmatic accretion from 2120 to 2080  
82 Ma known as the Eburnean orogeny (Bonhomme, 1962; Oberthür et al., 1998; Feybesse et al., 2006). Peak  
83 metamorphic conditions were reached in the Ashanti belt of Ghana at ~2100 Ma based on U-Pb ages of  
84 metamorphic titanite (Oberthür et al., 1998). Peak metamorphic conditions are widely reported as  
85 amphibolite facies (500–600°C; 4–6 kbar; John et al., 1999; White et al., 2013), although greenschist facies  
86 assemblages are dominant across the region (Hirdes et al., 1996).

87 The volcanic belts consist of tholeiitic lavas and associated mafic intrusions interbedded with minor  
88 sequences of immature sedimentary, volcanoclastic and carbonate rocks. The sedimentary basins comprise  
89 isoclinally folded and deformed sequences of greywacke, argillite and arkose with calc-alkaline volcanic  
90 sequences. Extensive suites of plutonic rocks have intruded both units, and range in composition from  
91 tholeiitic gabbro to high-K calc-alkaline granite. The majority of plutonic rocks are grouped by their host

92 terranes; i.e. 'belt-' and 'basin-type', and a post-Eburnean K-rich series (Leube et al., 1990; Hirdes et al.,  
93 1992).

94 The Birimian terranes formed over a period of ~180 Ma, between 2266 and 2088 Ma (Perrouy et al.,  
95 2012; White et al., 2014 and references therein; Parra-Avila et al., 2015). This period is divided into two  
96 phases, the age and terminology of each differs throughout the Birimian. In South western Ghana the  
97 Eburnean I (2266-2150 Ma) precedes the Eburnean II (2216-2088 Ma) (Allibone et al., 2002). In northern  
98 Ghana, the earlier event is referred to as the Eoeburnean (2195–2150 Ma) and the latter as the Eburnean  
99 (2148–2090 Ma) (de Kock et al., 2011). In Burkina Faso the Eburnean (2130 – 1980 Ma) is preceded by the  
100 Tangaeen event (2170-2130 Ma) (Tshibubudze et al., 2009; Hein, 2010). Broadly speaking, the earlier event,  
101 in each case, consists of volcanism, granitoid emplacement and fold, thrust tectonics. This is followed by  
102 emplacement of younger granitoids, strike-slip deformation and mineralisation in the latter event. U-Pb  
103 zircon ages show that the Eburnean I encompasses early volcanism, between  $2266 \pm 2$  and  $2132 \pm 3$  Ma  
104 (Taylor et al., 1992; Loh et al., 1999), and early plutonism, from  $2213 \pm 3$  to  $2151 \pm 7$  Ma (Dia et al., 1997;  
105 Gueye et al., 2007; White et al., 2014 and references therein). Tshibubudze et al., (in press) suggest that the  
106 three early events are broadly the same tectonic event. U-Pb dating of detrital zircons shows that  
107 sedimentation was coeval with magmatism in the volcanic belts, from  $2135 \pm 5$  Ma in Ghana (Oberthür et al.,  
108 1998; Davis et al., 1994) and from  $2164.7 \pm 0.9$  Ma in the KKI (Hirdes and Davis et al., 2002). The Eburnean  
109 represents the final phase of magmatism in Ghana, where basin-type plutons were intruded between  $2116 \pm$   
110  $2$  and  $2088 \pm 1$  Ma (U-Pb zircon) (Hirdes et al., 1992; Davis et al., 1994).

111 Though there are variations, models for crustal growth in the Birimian largely involve the development  
112 of juvenile volcanic arc magmas in an oceanic setting (Sylvester and Attoh, 1992; Dia et al., 1997; Pawlig et  
113 al., 2006; Soumaila et al., 2008; Baratoux et al., 2011). Recent P-T-t reconstructions in metasedimentary  
114 rocks record blueschist-facies metamorphic conditions diagnostic of subduction environments (Ganne et al.,  
115 2011).

### 116 3 Lithostratigraphy of the KKI

117 The stratigraphy of the KKI from west to east consists of: 1) bimodal volcanics intruded by numerous  
118 plutonic complexes in the MVB; 2) detrital sedimentary rocks of the Dialé-Daléma basin, which are intruded  
119 by the Saraya batholith; 3) calc-alkaline volcanoclastic rocks of the FVB and; 4) siliciclastic sedimentary rocks  
120 of the Kofi Series, unconformably overlain by Neoproterozoic sedimentary rocks to the east (Figure 1). Age  
121 data for the KKI are summarised in Table 1.

#### 122 3.1 The Mako Volcanic Belt

123 The MVB is a NNE trending ~20-40 km wide band of bimodal volcanic rocks which crop out in the west of  
124 the KKI. They are overlain to the west by the Pan-African Mauritanides belt. The Main Transcurrent Shear  
125 Zone (MTZ) marks the eastern edge of the MVB, with the Dialé-Daléma basin to the east (Figure 2). The  
126 lowermost units in the west consist of thick flows of massive and pillowed tholeiitic basalt. These are  
127 associated with dolerites and gabbros and intercalated with thin felsic tuffs, pyroclastites, rhyolites and  
128 minor clastic and carbonaceous sedimentary rocks (Dioh et al., 2006), which become more prominent to the  
129 east. The age of the Mako tholeiitic basalts is poorly constrained. Dia (1988) reported a whole-rock Pb-Pb  
130 age of  $2195 \pm 118$  Ma. Given this large error, the upper age limit for the Sandikounda amphibolite-gneiss  
131 complex (SAG; Figure 1) is interpreted to be the younger age limit for their eruption as it intrudes the lava  
132 sequences. The volcanic sequence is capped by andesitic lava, tuff and pyroclastic rocks (Dia, et al., 1997;  
133 Ngom et al., 2009). An andesite flow in the east of the MVB yielded a Sm-Nd whole-rock age of  $2160 \pm 16$  Ma  
134 (Boher et al., 1992).

135 The MVB is intruded by a plutonic complex known as the Kakadian batholith (Dia, 1985; Hirdes and  
136 Davis, 2002; Dioh et al., 2006; Gueye et al., 2007). The batholith is composed of three units in the north  
137 (Figure 1); 1) the Sandikounda amphibolite-gneiss complex (SAG); 2) the Sandikounda Layered Plutonic  
138 Complex (SLPC); and 3) the Laminia-Kaourou Plutonic Complex (LKPC). The south of the batholith is known as  
139 the Badon batholith. The SAG consists of tonalitic to dioritic gneiss containing amphibolite enclaves. This is  
140 the oldest unit in the north of the batholith. U-Pb data indicate crystallisation at  $2205 \pm 15$  Ma (Gueye et al.,

141 2007). The SLPC crystallised between  $2171 \pm 9$  and  $2158 \pm 8$  Ma (Pb-Pb and U-Pb zircon data; Dia et al., 1997;  
142 Goujou et al., 2010), and is composed of layered hornblende-gabbro, diorite, migmatite and hornblendite,  
143 with xenoliths of wherlite and pyroxenite. Elements of the SLPC intruded the SAG (Gueye et al., 2008). The  
144 LKPC consists of the Laminia and Kaourou plutons. Tonalite and granodiorite of the Laminia pluton were  
145 emplaced at  $2138 \pm 12$  and  $2105 \pm 8$  Ma (Pb-Pb zircon data; Dia et al., 1997; Gueye et al., 2008). The  
146 porphyritic monzogranite of the Kaourou pluton is younger at  $2079 \pm 6$  Ma (Pb-Pb zircon data; Dia et al.,  
147 1997). Both plutons contain xenoliths of Mako volcanic rocks and the SLPC (Dia et al., 1997). The Badon  
148 batholith is composed of biotite-granodiorite; magmatic emplacement occurred at a similar time to the SAG  
149 at  $2198 \pm 2$  Ma (Pb-Pb zircon data; Gueye et al., 2007). To the south east of the Badon batholith, the Mako  
150 belt was intruded by the Soukouta granite-granodiorite complex at  $2142 \pm 7$  Ma (U-Pb zircon; Delor et al.,  
151 2010). Delor et al., (2010) and Goujou et al., (2010) dated (U-Pb zircon) a series of granitic plutons, which  
152 intruded the MVB between  $2142 \pm 7$  Ma and  $2102 \pm 8$  Ma. The minor Mamakono and Tinkoto plutons  
153 intruded the MVB at  $2076 \pm 3$  Ma and  $2074 \pm 5$  Ma, respectively (U-Pb and Pb-Pb zircon data; Hirdes and  
154 Davis, 2002; Gueye et al., 2007). Ar-Ar and K-Ar studies on hornblende by Gueye et al. (2007) showed that  
155 the SAG and Tinkoto plutons cooled to  $\sim 550$  °C by  $2112 \pm 12$  Ma and  $2051 \pm 16$  Ma, respectively. The Badon  
156 batholith cooled to below  $\sim 300$ °C at  $2098 \pm 20$  Ma (Ar-Ar and K-Ar in biotite; Gueye et al., 2007).

### 157 3.2 The Dialé-Daléma series

158 Cropping out to the east of the MVB, the Dialé-Daléma series consists of a thick sequence of isoclinally  
159 folded volcanoclastic, siliciclastic and minor carbonate rocks centrally intruded by the Saraya Batholith  
160 (Hirdes and Davis, 2002; Gueye et al., 2008; Figure 1). The dominant volcanoclastic component of the Dialé-  
161 Daléma sediments suggests that they represent a lateral facies equivalent of the MVB. Subordinate basalts  
162 are interbedded in the westernmost sequence (Diallo, 2001), where the youngest detrital zircons yield a  
163 maximum U-Pb age of  $2165 \pm 0.9$  Ma (Hirdes and Davis, 2002). The Saraya batholith consists of several  
164 plutonic bodies, composed of biotite-muscovite-adamellite granite. These bodies were emplaced between



165 2079 ± 2 Ma and 2061 ± 15 Ma (U-Pb zircon and monazite) and place a lower limit on sedimentation in the  
166 Dialé-Dalemé Basin (Hirdes and Davis, 2002; Delor et al., 2010).

### 167 3.3 The Falémé Volcanic Belt

168 The Falémé Volcanic Belt crops out to the east of the Daléma basin (Hirdes and Davis, 2002; Lawrence et  
169 al., 2103a). The FVB is a ~16 km wide NNE trending belt of volcanic and intrusive rocks. Outcrop is dominated  
170 by plutonic rocks, consisting of two plutonic complexes, each >100 km<sup>2</sup>: 1) the Balangouma pluton in the  
171 north; and 2) the Boboti pluton in the centre and south of the belt. Several smaller plutons crop out in the  
172 southern and eastern regions of the FVB, including the South Falémé (Hirdes and Davis, 2002) and  
173 Garabourea plutons (Figure 2). The volcanic sequences comprise pillowed andesite flows, subordinate  
174 rhyodacite lavas and pyroclastic rocks. These are interbedded with volcanoclastic rocks, wackes and  
175 carbonate rocks (Hirdes and Davis, 2002; Schwartz and Melcher, 2004). Magnetite skarn deposits are hosted  
176 in several of the smaller plutons and carbonate rocks (Schwartz and Melcher, 2004). Limited age data are  
177 available for the volcanic sequence in the FVB. U-Pb zircon ages date a several volcanic and sub-volcanic  
178 rhyolite units at 2099 ± 4 Ma, 2082 ± 8 Ma and 2064 ± 30 Ma, with inheritance at 2155 ± 34 Ma (Hirdes and  
179 Davis, 2002). Further U-Pb zircon geochronological data from the Boboti pluton and the South Falémé  
180 tonalite show ages of 2080.2 ± 0.9 Ma and 2081.5 ± 1.1 Ma, respectively (Hirdes and Davis, 2002).

### 181 3.4 The Kofi Series

182 The Senegal-Mali Shear Zone (SMSZ) is a sinistral brittle-ductile shear zone that forms a 1-10 km  
183 wide N-S trending corridor of varying deformation styles, and separates the Kofi Series from the FVB.  
184 Secondary and higher order splays off the SMSZ host the major Au deposits in the Kofi Series, including Gara,  
185 Yalea, Sadiola, Yatela and Goukoto (Dommanget, et al., 1993; Lawrence et al., 2013a and b). The Kofi Basin  
186 is made up of detrital sedimentary and carbonate rocks and breccias intruded by minor mafic dykes and  
187 small intermediate to felsic stocks. The sedimentary rocks in the Kofi Series are dominantly wackes, with end  
188 member sandstone (rare) and argillite (common). Wackes and argillites are typically interbedded on a small  
189 scale (10s cm), although both rock types occur as thicker units (10s m), with gradational changes from quartz

190 wacke through to argillite common. The siliciclastic component of wackes varies between quartz and  
191 feldspar rich, with clasts showing a large range in size (fine sand to pebbles) and shape (angular to well  
192 rounded). Certain packages of quartz wacke, particularly in the west of the series have been intensely  
193 tourmalinised (Lawrence et al., 2013a), while others have been albitised. The Kofi Series is carbonate-rich to  
194 the west, with proximity to the Falémé Volcanic Belt (Figure 1). These carbonate rocks are dominantly  
195 dolomitic marls. Silicic clasts are composed of fine grained and sub angular quartz and feldspar. All  
196 sedimentary lithologies in the Kofi Series show poly-phase deformation generated during the Eburnean  
197 orogeny (Dabo and Aïfa, 2010). The igneous rocks that intruded the Kofi Series include dolerite to  
198 monzodiorite dykes and small stocks of quartz feldspar porphyry. Two larger plutons of monzogranite  
199 composition also intruded the Kofi Series, namely the Gamaye and Yatea plutons.

200 The age of deposition in the Kofi Series is constrained by detrital zircons and intrusive plutonic rocks.  
201 Tourmalinized quartz wacke at the Gara deposit include a detrital zircon dated by Pb-Pb at  $2093 \pm 7$  Ma  
202 (Boher et al., 1992). An older, deltaic deposit on the margin of the FVB yields a U-Pb detrital zircon age of  
203  $2125 \pm 27$  Ma (Boher et al., 1992), though it is unclear whether this belongs to the Kofi Series or the FVB. The  
204 Gamaye pluton has been dated at  $2045 \pm 27$  Ma using the Rb-Sr whole-rock isochron method, providing a  
205 broad lower age limit for sedimentation (Bassot and Cean-Vachette, 1984).

## 206 4 Methods

### 207 4.1 Mineral chemistry and petrography

208 Major and trace-element mineral compositions were determined using an Oxford Instruments X-ACT  
209 Energy Dispersive System (EDS) detector mounted on a Zeiss EVO 50 Scanning Electron Microscope (SEM) at  
210 Kingston University London. EDS operation employed an accelerating voltage of 20 kV, a beam current of 1.5  
211 na, and a detector process time of 4. Data collection and reduction was handled using the Oxford  
212 Instruments INCA analytical suite. The detection limit for all elements was approximately 0.20 wt %.

## 213 4.2 Geochemistry

214 Geochemical sample preparation and analyses were conducted at Kingston University. Rock pulps were  
215 desiccated overnight at 60 °C, then tested for loss on ignition (LOI) at 900 °C. 0.25 g of each sample was  
216 mixed with 1.25 g of lithium metaborate ( $\text{LiBO}_2$ ) flux and fused in graphite crucibles at 1050 °C. The melt was  
217 then dissolved in 150 ml of 0.5M nitric acid ( $\text{HNO}_3$ ), filtered, and diluted to a concentration of 0.3M  $\text{HNO}_3$ .

218 Analysis of major elements was conducted using a JY Ultima 2C inductively coupled plasma atomic  
219 emission spectrometer (ICP-AES). Standard reference materials: GSJ JR2 (rhyolite), USGS BCR-2 (basalt),  
220 USGS AVG-2 (andesite) and USGS BHVO-2 (basalt), were prepared and run as unknowns to monitor accuracy  
221 and precision. Measured values were within 3 % of the recommended values and the precision was better  
222 than 3 % (1 SD). USGS W-2 (Centerville diabase) was analysed every five samples to monitor instrumental  
223 drift.

224 Analysis of trace and rare earth elements (REEs) employed an Agilent 7500c quadrupole inductively  
225 coupled plasma mass spectrometer (ICP-MS). Samples, standards and blanks were prepared as above, and  
226 then diluted x25 in 0.5 % HCl and 1 %  $\text{HNO}_3$ . Instrumental drift was monitored by regular analysis of a 10 ppb  
227 multi-element solution. Accuracy and precision were determined from analysis of the standard reference  
228 materials: USGS AGV-2, GSJ JR-2, USGS BHVO-2, USGS BCR-2, GSJ JP-1, GSJ JA-2, TDB, WMG-1, GH, BR, Bt-  
229 Mica-Fe and Phl-Mica-Mg. Total accuracy was <3 % and precision was <4% (1SD).

## 230 4.3 Geochronology

231 Laser ablation inductively coupled mass spectrometry (LA-ICP-MS) was conducted on magmatic zircons  
232 from four samples of the Falémé Volcanic Belt. Zircons were separated using conventional methods at  
233 Kingston University. Zircons were mounted in 25 mm epoxy resin blocks, polished, and examined under  
234 SEM-CL to identify internal zonation and mineral inclusions.

235 LA-ICP-MS analysis was conducted at the Department of Earth Sciences, Royal Holloway University of  
236 London using a 193 nm excimer laser-ablation system featuring a two-volume Laurin LA cell coupled to an

237 Agilent 7500ce quadrupole ICP-MS (Müller et al., 2009) (Table 2). Using GeoStar software, ~150 spots  
238 analysis points of both unknowns (~100) and reference materials (standards; ~50) were selected, which  
239 comprise one 'run'. The primary standard GJ-1 (600.7 Ma, based on Jackson et al., 2004) was analysed every  
240 seventh analysis to monitor both downhole as well as long-term elemental fractionation. Acquisition time  
241 was 30 seconds per spot with 15 seconds background before and after, pulse rate was 5 Hz, spot size was 34  
242  $\mu\text{m}$  and laser fluence on target (energy density) was  $3 \text{ J/cm}^2$ . The standards Temora-2 ( $416.78 \pm 0.33\text{Ma}$ ;  
243 Black et al., 2004), 91500 ( $1065.4 \pm 0.3 \text{ Ma}$ ; Wiedenbeck et al., 1995), Mud Tank ( $732 \pm 5 \text{ Ma}$ ; Black and  
244 Gulson, 1978) and Plešovice ( $337.13 \pm 0.37 \text{ Ma}$ ; Sláma et al., 2008) were analysed as unknowns in order to  
245 ensure accuracy and reproducibility. Reduction of raw analytical data was performed using the Lolite  
246 software package® (Paton et al., 2010) in Wavemetrics Igor Pro® by applying exponential downhole  
247 fractionation and long-term spline data derived from the primary standard to both unknowns and secondary  
248 standards; no common-Pb correction was required. Approximate U, Th, Pb concentrations and Th/U-ratios  
249 are based on using the generally fewer 91500 analyses as calibration standard. Isochron diagrams,  
250 concordia, discordia and weighted mean U-Pb and Pb-Pb ages were calculated using the Isoplot 4.15 Excel  
251 macro (Ludwig, 2003).

252 Analyses of four international zircon standards were conducted to assess the accuracy and precision of  
253 the instrument. Thirty seven analyses of Plešovice yielded a concordant age of  $336.1 \pm 1.4\text{Ma}$  (MSWD=0.73);  
254 this gives an error of 0.3 % and precision of 0.8 % (2 SD). Twenty nine analyses of the 91500 standard yielded  
255 a concordant age of  $1053.8 \pm 8.7 \text{ Ma}$  (MSWD=0.9); this gives an error of 1.1 % and precision of 1.7 % (2 SD).  
256 Seventeen analyses of Temora-2 yielded a weighted average age of  $410.7 \pm 2.6 \text{ Ma}$  (MSWD=1.2), with error  
257 of 1.5 % and precision of 1.3 % (2 SD). Mud Tank yielded a concordant age of  $715 \pm 11 \text{ Ma}$  (MSWD=0.74);  
258 with error of 2.3 % and precision of 3.1 % (2 SD). Low U concentration in Mud Tank may contribute to higher  
259 error and uncertainty. The unknowns contained significantly higher concentrations of U; therefore Mud Tank  
260 can be disregarded when calculating accuracy and precision. Long-term reproducibility of  $^{238}\text{U}/^{206}\text{Pb}$  ages  
261 based on Plesovice and 91500 zircons is  $\pm 1.5 \%$  (2 RSD). Analytical data for zircon standards is presented in  
262 Table 3.

## 263 5 Petrographic data

### 264 5.1 The Falémé Volcanic Rocks

265 The earliest volcanism in the FVB is recorded by fine-grained porphyritic andesites that crop out in the  
266 Kabe West area, south of the Balangouma pluton. These plagioclase-amphibole porphyries contain abundant  
267 euhedral albite (15 %) and amphibole (15 %) phenocrysts (0.5-2 mm). The groundmass is made up of finer,  
268 bladed albite (60 %) with minor anhedral quartz (5 %). Albite is strongly sericitised (5 %) and amphibole is  
269 replaced by actinolite. Along the eastern margin of the Boboti pluton, porphyritic and equigranular andesite  
270 overlies albitised sub-volcanic diorite (Figure 3A). The andesites contain albite phenocrysts (10 %) and a  
271 groundmass of albite (65 %) and actinolite (25 %), with accessory rutile, ilmenite, apatite and zircon. The  
272 diorite is equigranular, medium to coarse-grained and richer in amphibole (35 %) and rutile than the  
273 andesite.

### 274 5.2 The Daléma Suite

275 This small suite of intrusive and extrusive rocks crop out over  $\sim 3 \text{ km}^2$  on the eastern margin of the Dialé-  
276 Daléma basin, west of the Balangouma pluton. In this location, a fine-grained porphyritic basaltic-andesite  
277 (Figure 3B) contains phenocrysts of plagioclase (10 %), olivine (10 %) and trace clinopyroxene. Plagioclase is  
278 dominant and occurs as 0.5 to 3 mm laths and rare coarse tabular crystals. Olivine is fine to medium grained  
279 and subhedral, with embayments and inclusions of the groundmass common. The groundmass (75 %) is very  
280 fine and contains a high proportion of magnetite (5 %), with plagioclase, olivine and accessory pyrite. To the  
281 north, a phaneritic gabbroic diorite (Figure 3C) contains phenocrysts of oligoclase (50 %) ( $\text{An}_{23}$ ) (up to 7 mm),  
282 magnesio-hornblende and tschermakite (35 %) (Both  $\sim 1.5 \text{ cm}$ ). These are replaced by biotite (10 %) and  
283 minor chlorite with associated ilmenite and titanite. Minor quartz and K-feldspar ( $\sim 5 \%$ ) occur in the  
284 groundmass, with allanite, chalcopyrite, apatite, pyrite, gypsum and zircon. In the same locality, a gabbroic  
285 diorite porphyry (Figure 3D) contains 1-6 mm, subhedral phenocrysts of oligoclase (10 %), biotite (5 %) and  
286 actinolite (5 %). The groundmass is composed of oligoclase (32 %) ( $\text{An}_{22}$ ), biotite (5 %), amphibole (40 %) and  
287 quartz (2-3 %), with minor clinopyroxene, K-feldspar, zircon and apatite.

### 288 5.3 The Balangouma Pluton

289 The Balangouma pluton occupies the majority (~200 km<sup>2</sup>) of the northern FVB and is composed of  
290 intermediate to felsic lithologies. The northern lobe of the pluton crops out to the north west of the Gara  
291 mine has been sheared out along the SMSZ. The main unit varies slightly in composition between  
292 monzodiorite, monzonite, quartz monzonite and granodiorite, but the bulk of the pluton is a coarse-grained,  
293 mesocratic quartz monzodiorite (Figure 3E). This contains coarse (5-7 mm) K-feldspar (2 %) and ~1 mm  
294 oligoclase (5 %) (An<sub>26</sub>) phenocrysts. These minerals are also present in the medium grained groundmass (13  
295 % and 25 %, respectively) together with biotite (26 %), quartz (9 %), augite (5 %) (Wo<sub>30</sub>En<sub>40</sub>Fs<sub>30</sub>) and  
296 hornblende (5 %). Pyroxenes and amphiboles are partially chloritised (10 %). Accessory phases include  
297 apatite, titanite, zircon and Cr-rich haematite. This unit is cross cut by 20-30 cm wide aplite dykes (Figure 3G)  
298 composed of medium grained intergrown plagioclase (10 %), K-feldspar (35 %) and quartz (50 %). Fine-  
299 grained (<100 µm) biotite (2 %) emphasises a weak shear fabric. Similar units crop out throughout the pluton  
300 as meter-scale stocks.

### 301 5.4 The Boboti Pluton

302 The Boboti pluton (~187 km<sup>2</sup>) makes up the central intrusive complex of the FVB. Schwartz and Melcher,  
303 (2004) and Dioh et al., (2006) describe the Boboti pluton as a clinopyroxene-hornblende-bearing  
304 granodiorite. Field mapping and sampling from outcrop in the southern Boboti pluton has revealed it to be  
305 more complex and composed of a number of intermediate to felsic intrusive stocks. Lithologies range in  
306 composition from diorite to monzogranite.

307 The southern body of the pluton is a coarse porphyritic quartz monzodiorite with 7-8 mm phenocrysts of  
308 albite (5 %), and ~2 mm phenocrysts of biotite and pyroxene (1 %) (Figure 4A). The groundmass is composed  
309 of sericitized albite (35 %), K-feldspar (25 %), quartz (10 %), clino- and orthopyroxene (10 %), biotite (9 %)  
310 and actinolite (3 %). Pyroxenes have been largely replaced by titanite (1 %) and V-Cr-bearing magnetite (1  
311 %). Accessory phases include apatite, ilmenite, chalcopyrite, monazite and zircon. Minor bodies of  
312 monzogranite (Figure 4B), ~1-2 km<sup>2</sup> in extent, intruded the centre of the southern Boboti pluton. These are

313 equigranular (400 - 600  $\mu\text{m}$ ) with rare 2-3 mm plagioclase phenocrysts. Quartz (31 %), albite (32 %) and K-  
314 feldspar (29 %) make up the groundmass, with minor intergrown muscovite (1 %) and biotite (1 %). Unevenly  
315 distributed clusters of <100  $\mu\text{m}$  euhedral tourmaline (1 %) grains are present throughout the rock. Accessory  
316 minerals include epidote, ilmenite, zircon, apatite and titanite. Extensive outcrops of porphyritic pyroxene-  
317 bearing quartz diorite (Figure 4C) occur to the west (Sample BOP4 in Figure 2). This is medium to coarse-  
318 grained with 4 mm albite phenocrysts (7 %), with finer biotite (1 %) and actinolite phenocrysts (<1 %). The  
319 groundmass is composed of albite (70 %), quartz (5 %), clino- and orthopyroxene (6 %), biotite (4 %),  
320 actinolite (2 %) and K-feldspar (1 %). Pyroxene grains contain abundant inclusions of titanite (2 %) and  
321 magnetite (1 %). Accessory phases include apatite, chalcopyrite, monazite and zircon.

## 322 5.5 Minor Falémé Intrusive rocks

323 To the south of the Balangouma pluton several small plutons crop out just north of the Kouroudiako  
324 magnetite skarn deposit in the Kabe West target area (Figures 2, 4D and 4E). These consist of medium to  
325 coarse-grained quartz diorite with minor carbonate-chlorite-epidote alteration and magnetite-pyrite  
326 mineralisation. Phenocrysts of plagioclase (1-6 mm) and actinolite (~1 mm) occur within a fine to medium  
327 grained groundmass of plagioclase, K-feldspar, quartz, biotite and minor orthopyroxene. To the west, several  
328 medium-grained dioritic plutons host a magnetite skarn deposit at Karakaene Ndi. These have a hiatal  
329 seriate texture, with medium to coarse-grained albite, biotite, actinolite and quartz in the groundmass.  
330 Biotite and actinolite replace primary hornblende. All the diorite plutons in this area have been albitised  
331 (feldspars have been altered to albite), with the characteristic assemblage of carbonate-chlorite-haematite  
332 in the groundmass.

333 The south Falémé pluton, south east of the Boboti pluton, is exposed along the Falémé River. It consists  
334 of albitised diorites, magmatic breccias, and a small suite of diorites. Fine-grained diorite porphyry contains  
335 phenocrysts of coarse euhedral albite (~1 cm) and medium-grained, subhedral actinolite. The groundmass  
336 comprises plagioclase and actinolite with accessory rutile.

## 337 5.6 Igneous rocks of the Kofi Series

### 338 5.6.1 The Yatea granite and North Gara stock

339 The Yatea granite, which crops out in the east of the Kofi Series, is of similar affinity to a small stock  
340 which crops out just north of the Gara mine. Both bodies are pink coloured, medium-grained (1-3 mm)  
341 monzogranite (Figure 4F). Orthoclase and microcline (45 %) are dominant over plagioclase (up to 25 %). The  
342 mafic assemblage is dominated by biotite (<10 %). Accessory phases include magnetite, monazite and  
343 titanite.

### 344 5.6.2 The Gamaye pluton

345 The Gamaye pluton is the largest igneous body exposed in the Kofi Series (~138 km<sup>2</sup>). It is composed of  
346 monzogranite (Figure 4G), which is porphyritic in the south and equigranular in the north. The pluton is  
347 cross-cut by tourmaline bearing pegmatite dykes. The northern part of the pluton is composed of phaneritic  
348 monzogranite. The mineralogy consists of medium grained (200 - 500 µm), subhedral albite (35 %), K-  
349 feldspar (30 %), quartz (27 %) and biotite (8 %). Accessory minerals include muscovite, allanite and apatite  
350 (200 - 400 µm), zircon, rutile and magnetite. Tourmaline is disseminated in 1-5 cm halos around pegmatite  
351 dykes. Feldspars are weakly sericitized. This unit becomes porphyritic ~15 km to the SE (MOU2; Figure 2). K-  
352 feldspar forms subhedral poikilitic phenocrysts (up to 7 mm), and contains inclusions of quartz, plagioclase  
353 and biotite. Sub-rounded, 1 to 15 cm mafic enclaves are present throughout the unit. A series of coarse-  
354 grained pegmatite dykes cross cut the pluton. These are 1-30 cm wide and composed of 10-15 mm albite,  
355 quartz and K-feldspar, and ~200 µm muscovite. Some dykes contain very coarse (up to 8 mm) tourmaline  
356 crystals. These are typically subhedral, with inclusions of quartz and apatite. Thin (1-2 mm) tourmaline veins  
357 cross cut the dykes.

### 358 5.6.3 Minor intrusive rocks in the Kofi Series

359 The Kofi Series is intruded by numerous discordant dykes (typically <5 m) and small (sub-km scale)  
360 plutons. Some units are extremely fine-grained. These minor igneous units are typically intermediate, diorite



361 to quartz monzodiorite in composition, though mafic dykes are also present. Many lithologies have been  
362 albitised to variable degrees.

363 Small stocks of biotite-quartz-feldspar porphyry (QFP; Figure 4H) occur in the vicinity of the Gamaye  
364 pluton. Quartz (16 %), plagioclase (16 %) and K-feldspar (2 %) phenocrysts are up to 8 mm, while biotite  
365 phenocrysts (6 %) measure ~1 mm. The groundmass (~60 % of the rock) is composed of <20 µm mineral  
366 phases (likely quartz, plagioclase, k-feldspar and biotite). Feldspars show weak to moderate sericite  
367 alteration. Intensely albitised QFP stocks occur near the Baqata and Kolya target areas (Figure 2). These  
368 contain coarse (up to 7 mm) relict phenocrysts of quartz and feldspar, the latter having been replaced by  
369 glomeroblastic albite. The groundmass is composed of secondary <100 µm albite with interstitial ankerite  
370 and very fine –grained haematite. Albite is weakly sericitized.

371 Medium to coarse grained quartz monzodiorite dykes have intruded the footwall of the Goukoto  
372 deposit. These contain phenocrysts of plagioclase (5 %) and amphibole (replaced by actinolite) in a  
373 groundmass of plagioclase (60 %), k-feldspar (5 %), quartz (10 %), actinolite (10 %) and biotite (10 %).  
374 Accessory phases include augite (primary), apatite, tourmaline, ilmenite, rutile, monazite and chromite. In  
375 addition, dykes of medium grained diorite occur throughout the Kofi Series. The mineralogy consists of  
376 plagioclase (75 %), biotite (20 %) and K-feldspar (5 %) with accessory rutile and pyrite. It is possible that  
377 these were originally monzodiorite dykes which have undergone weak albitisation.

378 Mafic dykes 0.5 to 13 m wide have intruded the wall-rock at both the Gara and Yalea Au deposits. These  
379 are discontinuous, deformed and metamorphosed, forming sharp contacts with the host sediments. The  
380 intensity of alteration makes primary compositions difficult to identify.

#### 381 5.6.4 Hydrothermal albitite

382 Albitite crops out primarily at two localities within the Kofi Series, one at Baqata on the Bambadji permit  
383 and one 15 km to north, in the Falémé River, near Kolya. In outcrop the unit is massive and blocky, with no  
384 definable sedimentary or igneous textures. The lithology is composed dominantly of equigranular albite (85-

385 95 %) with accessory quartz, chlorite, apatite, rutile, allanite, zircon and biotite. Chlorite is associated with  
386 fractures cross cutting the groundmass. It is likely that this unit is the result of extreme alteration of an  
387 igneous protolith and therefore represents the most intense example of the sodic alteration seen in this  
388 region.

#### 389 5.6.5 Post-Birimian dolerite dykes

390 These dolerite dykes cross cut all lithologies in the KKI and show no clear evidence of deformation or  
391 hydrothermal alteration. These are more continuous than the Birimian dykes and vary in thickness from 2-  
392 200 m. Mineralogy consists of bytownite ( $An_{71-79}$ ), clinopyroxene and rare orthopyroxene. Similar dykes  
393 elsewhere in the WAC belong to the 200 Ma Central Atlantic Magmatic Province (CAMP; Jessell et al., 2015)  
394  $\pm$ . Though some CAMP-aged dykes are no doubt present, the mafic dykes in the KKI are dominantly older.  
395 Mafic dyke swarms with ages of  $\sim$ 1350-1400 Ma are most abundant, but ages of  $\sim$ 900 Ma and 1150 Ma are  
396 also present (K-Ar whole-rock data; Delor et al., 2010).

## 397 6 Geochemistry

398 A total of 42 fresh (unaltered) and albitised whole-rock samples were analysed for major and trace  
399 element concentrations. Only samples with minimal weathered crust and hydrothermal alteration were  
400 selected for analysis, with the exception of 14 samples of albitised igneous rocks. These were included to  
401 investigate the geochemical characteristics of the regional sodic alteration. All trace element data has been  
402 normalized against Normal-Mid Ocean Ridge Basalt concentrations (N-MORB; data from Sun and  
403 McDonough, 1989). Whole rock geochemical data is summarised in tables 4, 5, 6 and 7.

404 The geochemical data from the FVB and Kofi Series show a suite of igneous rocks with high-K calc-  
405 alkaline affinities (Figure 5A and B) with compositions ranging from gabbroic through to granitic (Figure 6).  
406 The FVB is dominated by large plutons of intermediate composition, with metaluminous A/CNK values  
407 (mean = 0.8; Figure 7), relatively little REE fractionation (mean La/Lu = 22.3) and very minor Eu anomalies  
408 ( $Eu/Eu^* = 0.9$ ; Figure 8). The small suite of felsic stocks that intruded the Balangouma and Boboti plutons are

409 more evolved ( $\text{SiO}_2 > 73\%$ ), with moderately fractionated REE patterns (mean  $\text{La/Lu} = 50$ ), peraluminous  
410  $\text{A/CNK}$  values (mean  $= 1.2$ ) and more distinct negative Eu anomalies (mean  $\text{Eu/Eu}^* = 0.6$ ; Figure 8C). By  
411 comparison to the FVB, the Kofi Series contains less exposure of igneous rock. These are dominantly highly  
412 fractionated (mean  $\text{La/Lu} = 113$ ), peraluminous (mean  $\text{A/CNK} = 1.1$ ) granites of similar affinity to the minor  
413 felsic stocks of the FVB. Minor dykes and plutons of more intermediate compositions are largely albitised;  
414 these exhibit metaluminous  $\text{A/CNK}$  values (mean of 0.99) and relatively little REE fractionation ( $\text{La/Lu}$  of  
415 19.9). The rocks of the Daléma igneous suite form a separate group, consisting of unevolved gabbros and  
416 dolerites with highly metaluminous  $\text{A/NK}$  and  $\text{A/CNK}$  values (Figure 7) and low  $\text{La/Lu}$  ratios (mean  $= 9.4$ ).

417 All samples show enrichment in the light ion lithophile (LILE) elements, with granitic samples showing  
418 considerably higher enrichment in both the Kofi Series and the FVB (Figure 8). All rocks from both terranes  
419 show consistent negative Nb and Ta anomalies (Figure 8D to F). In addition, granitic rocks from the Falémé  
420 Belt and Kofi Series show pronounced negative Ti and P anomalies (Figure 8F).

421 Albitised samples show consistently high  $\text{Na}_2\text{O}$  concentrations (mean  $= 7.8$  wt. %), with correspondingly  
422 low concentrations of most other major elements, most notably  $\text{K}_2\text{O}$  (mean  $= 0.6$  wt. %). As a result of this,  
423 the albitised samples lie in the tholeiitic series of the  $\text{K}_2\text{O}$  versus  $\text{SiO}_2$  diagram (Figure 5A) and also  
424 consistently plot above the alkaline-sub-alkaline divide on the TAS diagram (Figure 6); unaltered samples are  
425 consistently of sub-alkali affinity. Use of the Th-Co diagram of Hastie et al. (2007) reveals that the albitised  
426 samples should indeed belong to the calc-alkaline and high-K calc-alkaline series (Figure 5B), as do the  
427 unaltered rocks of the eastern KKI.  $\text{A/NK}$  values in albitised rocks are significantly lower than in unaltered  
428 rocks, yet  $\text{A/CNK}$  values are unperturbed (Figure 7). This reflects albitisation of both plagioclase (loss of  $\text{Ca}^{2+}$ )  
429 and K-feldspar (loss of  $\text{K}^+$ ), and likely replacement of other alkali-bearing mineral species (e.g. biotite).  
430 Albitised rocks plot in the alkaline field of the TAS diagram as a direct result of Na metasomatism.

431 7 LA-ICP-MS U-Pb Zircon Geochronology

## 432 7.1 Boboti Pluton

## 433 7.1.1 BOP1A

434 Sample BOP1A was obtained from the Southern part of the Boboti pluton. This unit is a coarse quartz  
435 monzodiorite with albite, biotite and pyroxene phenocrysts (Figure 4A). A total of 71 zircon grains were  
436 analysed (84 spots in total). These were stubby, subhedral, fine-grained (<150  $\mu\text{m}$ ) and highly fractured.  
437 Growth zones revealed under SEM-CL are well developed in some grains and almost absent in others (Figure  
438 9A, B, C and D). A systematic relationship between zonation, apparent age and the degree of discordance  
439 was not observed. Forty three analyses produced concordant ages within a  $2\sigma$  error ellipse (Figure 10A); 19  
440 of these were highly concordant (Figure 10B and C). The majority of the data (70 spots) formed a clear  
441 discordia trending toward the origin. This is interpreted to be caused by recent Pb-loss attributed to surface  
442 weathering. Analytical data for sample BOP1A is presented in Table 8.

443 A regression line fitted to the 70 concordant and discordant spots intersects the isochron at  $2088.5 \pm 8.5$   
444 Ma (MSWD=2.2), with a lower intercept around the origin (-5 Ma; Figure 10A). This corresponds well with a  
445 weighted average  $^{206}\text{Pb}/^{238}\text{U}$  age from the 19 most concordant spots of  $2093 \pm 9.6$  Ma (MSWD=1.6; Figure  
446 10B) and a weighted average  $^{207}\text{Pb}/^{206}\text{Pb}$  age of  $2085 \pm 11$  Ma (MSWD=6.3; Figure 10C). In order to minimize  
447 the rejection of data points the upper discordia intercept of  $2088.5 \pm 8.5$  Ma is interpreted to represent the  
448 age of magmatic emplacement.

449 In addition to the main population, 2 small grain populations show evidence for inheritance of older  
450 material at  $\sim 2200$  Ma and 3000 Ma (Figure 11A and B). Two zircon grains 9 and 22 yield partially concordant  
451 ( $\sim 99\%$ )  $^{206}\text{Pb}/^{238}\text{U}$  ages at  $2209 \pm 34$  Ma and  $2215 \pm 35$  Ma respectively (Figure 9C and D). These yield a  
452 concordia age of  $2226 \pm 13$  Ma (MSWD of 1.4; Figure 11A). CL imaging show bright cores with diffuse  
453 zonation surrounded by a dark 2-10  $\mu\text{m}$  rim. Two grains (zircons 75 and 73; Figure 9E and F) yielded  
454 concordant  $^{206}\text{Pb}/^{238}\text{U}$  ages at  $3000 \pm 120$  and  $3380 \pm 160$  Ma respectively (Figure 11B) and Pb-Pb ages of  
455  $2865 \pm 84$  Ma and  $3152 \pm 94$  Ma. Both the Archaean aged grains are fractured and feature a luminescent,

456 finely zoned core and with a dark rim (Figure 11B). These cores may be the inherited component, with the  
457 dark rim a later overgrowth related to magmatism at ~2 Ga.

458 These new data broadly agree with the published age of emplacement for the Boboti pluton at  $2080.2 \pm$   
459  $0.9$  Ma (Hirdes and Davies, 2002). However, our data show a more protracted period of emplacement with a  
460 more widely distributed age population and additional evidence of inheritance from early magmatism and  
461 possible Archaean material.

## 462 7.2 Balangouma Pluton

### 463 7.2.1 CLIB01

464 Sample CLIB01 from the Balangouma pluton to the north west of the Loulo mine camp is a coarse  
465 grained, mesocratic quartz monzodiorite with coarse (5-7 mm) K-feldspar phenocrysts (Figure 3E). A total of  
466 81 grains were analysed (94 spots in total). The majority of spots produced highly discordant ages. Grains  
467 were stubby, subhedral, fine-grained ( $<150$   $\mu\text{m}$ ) and highly fractured (Figure 9G and H). As with sample  
468 BOP1A, growth zonation appears to bears no relationship to the age or concordance of the grains. Analyses  
469 of the cores and rims of zircons are also consistently within error of each other. Analytical data for sample  
470 CLIB01 is presented in Table 9.

471 A discordia line was fitted to a subset of 43 spots with an upper intercept of  $2105.6 \pm 9.8$  Ma  
472 (MSWD=5.8) and a lower intercept at  $28 \pm 57$  Ma (Figure 12A). The lower intercept near the origin implies  
473 that recent Pb-loss is responsible for the discordance. A weighted mean  $^{207}\text{Pb}/^{206}\text{Pb}$  age of  $2098 \pm 6.3$  Ma  
474 (MSWD=4.6; Figure 12B) corresponds well to the upper intercept age as does a weighted mean  $^{206}\text{Pb}/^{238}\text{U}$   
475 age calculated from the most concordant spots ( $n=7$ ) of  $2097 \pm 25$  Ma (MSWD=3.9; Figure 12C). The age of  
476 magmatic emplacement is best represented by the upper intercept of the discordia, with an age of  $2105.6 \pm$   
477  $9.8$  Ma. This sample showed no evidence of inheritance.

### 478 7.2.2 CLIB05

479 Sample CLIB05 was collected from the Balangouma pluton around 8.5 km south of CLIB01. This sample is  
480 a coarse grained quartz monzonite with K-feldspar phenocrysts (Figure 3F). A total of 69 zircon grains were  
481 analysed (81 spots in total). Grains were subhedral, fractured and fine grained (<150  $\mu\text{m}$ ). Examination under  
482 SEM-CL reveals fine concentric zonation in the majority of zircon grains (Figure 9I and J). Some grains show  
483 small, anhedral cores lacking zoning; spot analyses of these cores tend to yield discordant ages. Analytical  
484 data for sample CLIB05 is presented in Table 10.

485 A significant number of analysed spots produced highly discordant ages, generating a discordia with an  
486 upper intercept of  $2118 \pm 16$  Ma (MSWD=2.3; n=43) and a lower intercept around 100 Ma (Figure 13A). A  
487 weighted average of the 13 most concordant  $^{206}\text{Pb}/^{238}\text{U}$  ages yields a younger age of  $2054 \pm 24$  Ma  
488 (MSWD=0.58; Figure 13B), however the weighted average for the equivalent  $^{207}\text{Pb}/^{206}\text{Pb}$  ages gives an age of  
489  $2096.5 \pm 9.3$  Ma (MSWD=1.4; Figure 13C), which broadly agrees with the upper intercept of the discordia.  
490 This weighted average  $^{207}\text{Pb}/^{206}\text{Pb}$  age remains relatively consistent even if a limited number of analyses are  
491 rejected, giving an average age of  $2103 \pm 20$  Ma, though this does produce a very high MSWD of 26 (n=57;  
492 Figure 13D). On the basis of this broad agreement it seems likely that the upper discordia intercept age of  
493  $2118 \pm 16$  Ma represents the age of magmatic emplacement for this sample.

### 494 7.2.3 CLIB07

495 Sample CLIB07 was collected from an outcrop approximately 1.2 km to the northwest of CLIB05 in the  
496 Balangouma pluton. The sample is a coarse porphyritic monzonite (Figure 3H). A total of 59 zircon grains  
497 were analysed (70 spots in total). Grains are euhedral, fine (<150  $\mu\text{m}$ ) and highly fractured with rare  
498 inclusions of apatite and quartz (Figure 9K and L). As with other samples, growth zonation shows no clear  
499 relationship to the age or concordance of spots. Where cores and rims have been analysed,  $^{206}\text{Pb}/^{238}\text{U}$  ages  
500 are consistently within error of each other. Analytical data for sample CLIB07 is presented in Table 11.

501 The analyzed grains produced highly discordant ages for a large number of spots. A set of 56 spots form  
502 a discordia with an upper intercept at  $2113 \pm 15$  Ma and a lower intercept at 76 Ma (MSWD=1.4; Figure  
503 14A). This corresponds well to the weighted mean  $^{207}\text{Pb}/^{206}\text{Pb}$  age for the same spots of  $2102 \pm 8.2$  Ma

504 (MSWD=7.3; Figure 14B). In addition the weighted mean of the  $^{206}\text{Pb}/^{238}\text{U}$  ages of the 9 most concordant  
505 spots yields an age of  $2086 \pm 23$  Ma (MSWD=0.27; Figure 14C). The upper discordia intercept is accepted as  
506 the most probable age for magmatic emplacement for this sample at  $2113 \pm 15$  Ma. This is on the basis of  
507 the overlapping mean U-Pb and Pb-Pb ages and the minimal rejection of data points in order to construct a  
508 robust discordia. No evidence of inheritance was found in this sample.

509 Given that the overall reproducibility of our method is  $\pm 1.5\%$  (2 RSD), the three ages of emplacement  
510 for the Balangouma pluton are analytically indistinguishable. We therefore favour an unweighted mean age  
511 for each of these units (represented by CLIB01, 05 and 07) of  $2112 \pm 13$  Ma.

## 512 8 Discussion

### 513 8.1 Tectonic setting of the KKI

514 The Falémé Volcanic Belt and the Kofi Series consist of high-K and uppermost calc-alkaline series volcanic  
515 and magmatic rocks with fractionated REE patterns, and immature, siliciclastic sedimentary rocks. This  
516 suggests an island arc or active continental margin setting, an interpretation further supported by persistent  
517 depletion in Nb-Ta relative to HFS elements (Figure 8). This phenomenon is attributed to magmas derived  
518 from partial melting of sub-arc mantle wedge. This is due to the insolubility of Nb and Ta in slab-derived  
519 aqueous fluids and strong partitioning into residual rutile (Brenan et al., 1994; Baier et al., 2008). Calc-  
520 alkaline volcanic and plutonic rocks in the MVB display similar LREE and LILE enrichment, and negative Nb  
521 anomalies (Boher et al., 1992; Dioh et al., 2006; Pawlig et al., 2006) suggesting a similar tectonic setting.

522 The least evolved rocks in the region belong to the Daléma Suite. The tectonic setting in which this unit  
523 formed is unclear; Nb-Ta depletion and high Th/La and positive Ce/Ce\* inherited from subducted sediment  
524 (Plank, 2005; Hastie et al., 2013; Figure 15) all point to a volcanic arc environment. The Dy/Dy\*-Dy/Yb  
525 diagram of Davidson et al. (2013; Figure 16) is of use here as it can represent the shape of a REE pattern in a  
526 single point. This highlights the slight LREE-enriched MORB character in the Daléma samples. LILE

527 enrichment and near-MORB HREE values (Figure 8) suggest a possible extensional (back-arc) setting. Back-  
528 arc rocks commonly feature arc-like chemistries modified by an invading fertile mantle source below the  
529 spreading centre (Taylor and Martinez, 2003).

530 The less evolved rocks, dominantly present in the FVB (typically silica oversaturated syeno-diorites),  
531 show characteristics typical of volcanic arc granites (Figure 17). These include the predominance of  
532 amphibole, biotite and pyroxene in ferromagnesian mineral assemblages, depleted medium to HREE (Figure  
533 8; a function of amphibole fractionation) and metaluminous A/CNK (Figure 7; c.f. Pearce, 1996). Minor  
534 negative P anomalies and enrichment in Zr and Hf compared to other HFS elements (Figure 8E), respectively  
535 indicate minor apatite fractionation and zircon accumulation (Pearce et al., 1984). Th/La-Ce/Ce\* ratios  
536 (Hastie et al., 2013; Figure 16) indicate that the arc rocks in the eastern KKI contain a mix of slab derived  
537 components. These are dominated by volcanic and continental detritus, with minor contribution from  
538 hydrogenous Fe–Mn oxides linked to slow sedimentation rates.

539 The felsic rocks (granites sensu stricto) of the FVB and Kofi Series feature negative Eu, Ti and P  
540 anomalies, not observed in the intermediate lithologies (Figure 8) and classify as syn-collision granites  
541 (Figure 17). Negative Eu anomalism indicates that plagioclase fractionation took place under relatively  
542 reduced conditions (increasing  $\text{Eu}^{2+}/\text{Eu}^{3+}$ ) during magma evolution (Drake, 1975). Similarly, depletions in Ti  
543 and P indicate fractionation of apatite and Ti oxides. The Dy/Dy\*-Dy/Yb diagram (Figure 15) indicates that  
544 felsic rock in the study area have incorporated significant amounts of sediment (Davidson et al., 2013).

545 Overall, the igneous rocks of the south-eastern KKI represent a volcanic arc, developed above a  
546 subducting oceanic plate. This subsequently evolved into a collisional setting. The Dy/Dy\*-Dy/Yb diagram  
547 (Figure 15) adequately represents the evolution of the arc system, with the Daléma igneous rocks plotting in  
548 the E-MORB field and the Balangouma pluton and some of the more intermediate intrusions in the Kofi  
549 showing upper continental crust compositions. The bulk of the data sit along the trend of increasing  
550 sediment incorporation, with the most felsic, peraluminous rocks showing the highest Dy/Yb values. The  
551 Th/La-Ce/Ce\* diagram (Figure 16) shows that the mantle wedge below the arc has a significant contribution



552 of continental detritus and hydrogenous Fe–Mn oxides as well as minor volcanic detritus from the  
553 downgoing slab.

554 The MVB differs significantly from the FVB, due to the presence of a lower sequence of tholeiitic igneous  
555 rocks. It is generally agreed (Abouchami et al., 1990; Diallo, 2001), due to the presence of pillow lavas,  
556 turbidite sequences, a lack of significantly older inherited material and consistently positive  $\epsilon_{\text{Nd}}$  values (+4.9;  
557 Ngom et al., 2009) that these tholeiites are juvenile. However, there is debate over specific tectonic setting  
558 being attributed to either: 1) intra-plate oceanic plateau (Abouchami et al., 1990; Boher et al., 1992; Ngom  
559 et al., 2009); or 2) an immature oceanic island arc (Sylvester and Attoh, 1992; Dia et al., 1997; Diallo, 2001;  
560 Pawlig et al., 2006). Abouchami et al. (1990) and Boher et al. (1991) suggested an oceanic plateau setting  
561 based on low Ti concentrations, LREE depletion and pronounced negative Ce anomalies, placing the MVB  
562 tholeiites between MORB and island arc compositions. Sylvester and Attoh (1992) observed that the Mako  
563 and other Birimian belts show petrogenetic similarities with modern island arcs. The granitic rocks (*sensu*  
564 *lato*; >5 % quartz) in the MVB are characterised by persistent negative Nb-Ta anomalies and LILE enrichment  
565 (Boher et al., 1992; Dioh et al., 2006; Pawlig et al., 2006). Dioh et al. (2006) reported that the majority of  
566 calc-alkaline and high-K intrusive rocks in the MVB classify as volcanic arc granites. A small subset lies along  
567 the divide between volcanic arc and syn-collisional granite, including granites (*sensu stricto*) from the  
568 Kéniéba pluton. These share geochemical characteristics with syn-collisional granites in the FVB and Kofi  
569 Series, including peraluminous A/CNK values (1.03-1.04), negative Eu anomalies (0.72-0.81) and high Dy/Yb  
570 values (~3.2). These points suggest that, despite the absence of tholeiites in the FVB, plutonic rocks in the  
571 western KKI developed in very similar tectonic settings to those in the east, evolving from juvenile volcanic  
572 arc to a collisional setting.

## 573 8.2 Geochronological framework for the Kédougou-Kéniéba Inlier

574 New U-Pb zircon age data presented here show that the Balangouma pluton crystallised at  $2112 \pm 13$   
575 Ma (Table 1; Figure 18). Additionally, evidence of inherited zircon cores from the ~2085 Ma Boboti pluton  
576 (Hirdes and Davis, 2002 and this study), suggest an earlier phase of magmatism in the FVB at ca.  $2226 \pm 13$

577 Ma (Figure 18). This suggests the presence of underlying basement material which predates the SAG in the  
578 Mako Belt at  $2213 \pm 3$  Ma (Gueye et al., 2007).

579 In general, the intermediate to felsic rocks in the KKI are the younger units. They are also the most likely  
580 to yield useable zircons for accurate and precise dating. The geochronological data presented here,  
581 combined with existing data, allows the synthesis of a geochronological framework for the KKI. Much of the  
582 available age data imply diachroneity, with the westernmost MVB containing the oldest units (the SAG and  
583 Badon pluton; Figure 18); the FVB, sedimentary basins and silicic intrusive rocks are generally younger.  
584 Inherited grains found in several units of the FVB indicate that volcanism may have occurred simultaneously  
585 in both the Falémé and MVBs. The following sequence of events can be determined from the available data  
586 (Figure 18):

- 587 1. The intrusion of the SAG and elements of the Badon pluton occurred between  $2213 \pm 3$  Ma and  $2194$   
588  $\pm 4$  Ma (Dia et al., 1997; Gueye et al., 2007). The Mako tholeiitic lavas are assumed to be older.  
589 However, it is possible that tholeiitic volcanism was cogenetic with emplacement of the SAG or  
590 Badon pluton (Pawlig et al., 2006). Inherited zircon grains from the Boboti pluton imply  
591 magmatism may have occurred at some time prior in the FVB at  $\sim 2226$  Ma.
- 592 2. The SLPC intruded the Mako volcanics and the SAG between  $2171 \pm 9$  Ma and  $2158 \pm 8$  Ma (Dia et  
593 al., 1997; Goujou et al., 2010) within the time frame for possible calc-alkaline magmatism in the  
594 FVB at  $2155 \pm 34$  Ma, based on inherited zircon grains from a rhyolite flow (Hirdes and Davis,  
595 2002). Sedimentation began in the westernmost Dialé-Daléma basin at  $2164.7 \pm 0.9$  Ma (Hirdes  
596 and Davis, 2002), coinciding with andesitic volcanism at  $2160 \pm 16$  Ma (Boher et al., 1992).
- 597 3. The southern portion of the MVB was intruded by the Soukouta granite at  $2142 \pm 7$  Ma. The oldest  
598 component of the LKPC was emplaced over 33 Ma, from  $2138 \pm 6$  Ma to  $2105 \pm 8$  Ma (Dia, 1988;  
599 Dia et al., 1987). The latter stages of emplacement overlap with the main phase of magmatism in

600 the FVB. The SAG cooled below 550 °C at  $2112 \pm 12$  Ma (Gueye et al., 2007. Deltaic deposits  
601 began to develop on the western margin of the Kofi basin at  $2125 \pm 27$  Ma (Boher et al., 1992).

602 4. The Falémé plutonic rocks (including the Boboti, Balangouma and South Falémé plutons) were  
603 emplaced into pre-existing volcanic and sedimentary units between  $2112 \pm 13$  Ma and  $2080 \pm$   
604  $0.9$  Ma, coinciding with felsic volcanism at  $2099 \pm 4$  Ma (Hirdes and Davis, 2002). During this  
605 period ( $2103$  to  $2102$  Ma), further granitic plutons intruded the northern MVB (Goujou et al.,  
606  $2010$ ) and rhyodacite units erupt in the Dialé-Daléma Basin ( $2098 \pm 13$  Ma; Delor et al.,  $2010$ ).  
607 Sedimentation in the Kofi basin began at  $2093 \pm 7$  Ma at the latest (Boher et al., 1992). A deltaic  
608 deposit began developing at  $2125 \pm 27$  Ma, as reported by (Boher et al., 1992); however it is  
609 unclear if this deposit belongs to the Kofi Series or the Falémé Belt. In either case, it provides an  
610 argument for syn-volcanic sedimentation.

611 5. The latter stages of magmatism in the FVB and MVB are broadly coincident. The youngest unit of the  
612 LKPC (the Kaourou pluton) and the late calc-alkaline series plutons (Tinkoto and Mamakono) in  
613 the MVB all crystallised between  $2079 \pm 6$  Ma and  $2074 \pm 5$  Ma (Dia et al., 1997; Hirdes and  
614 Davis, 2002; Gueye et al., 2007). A period of felsic volcanism in the FVB between  $2082 \pm 8$  Ma  
615 and  $2064 \pm 30$  Ma (Delor et al., 2010) coincided with calc-alkaline volcanism in the MVB at  $2067$   
616  $\pm 12$  Ma (Gueye et al., 2007) . The Tinkoto pluton cooled below 550 °C by  $2051 \pm 16$  Ma (Gueye  
617 et al., 2007). The Saraya batholith marks the youngest limit for the Dialé-Daléma basin at  $2079 \pm$   
618  $2$  Ma (Hirdes and Davis, 2002). Metamorphic monazites within the batholith formed at  $2064 \pm 4$   
619 Ma and the pluton is interpreted to have cooled below 350 °C by  $2021 \pm 11$  Ma (Gueye et al.,  
620 2007).

621 Sedimentation in the Kofi Series is considered to have ceased by  $2045 \pm 27$  Ma; the best-known age of  
622 crystallisation of the Gamaye pluton (Bassot and Cean-Vachette, 1984).The data summarised in Figure 18  
623 suggest that the development of the volcano-sedimentary belts and sedimentary basins of the KKI occurred  
624 broadly synchronously, with a suite of older units within the westernmost MVB likely representing the

625 earliest development of upper crust in the region (Dia et al., 1997; Geuye et al., 2007). For the older units of  
626 the KKI, Gueye et al. (2007) reported prolonged cooling profiles; with K-Ar from amphibole and biotite  
627 apparently suggest that the plutons took ~80 Ma to cool from 900 to 550 °C and ~100 Ma to cool from 900  
628 to 300 °C, respectively. Smaller, younger plutons such as the Tinkoto granodiorite yielded K-Ar in amphibole  
629 ages within error of the crystallisation age of  $2079 \pm 6$  Ma. Assuming no disturbance of the K-Ar system, this  
630 suggests that the western KKI remained hot (~550°C) until ~2100 Ma. The early magmatism in the KKI  
631 (represented by the SAG, Badon granodiorite and SLPC) likely corresponds to the Eoeburnean/Eburnean I of  
632 Ghana (Allibone et al., 2002; de Kock et al., 2011) and the Tangaeen of Burkina Faso (Tshibubudze et al.,  
633 2009; Hein, 2010). New inherited zircon data in the Boboti pluton, suggests that magmatism occurred at a  
634 similar time in the FVB (~2226 Ma).

635 Sedimentation coincides with the onset of calc-alkaline volcanism and magmatism in both volcanic belts,  
636 supporting derivation from erosion of the arcs (c.f. Roddaz et al., 2007). In general, the more evolved  
637 magmatic rocks (the Saraya batholith, Gamaye pluton and the minor felsic stocks in the FVB) post-date the  
638 intermediate lithologies, either absolutely (through dating) or based on field relationships. This reflects the  
639 temporal evolution of the magmatic systems in the KKI through the arc stage and into the Eburnean  
640 orogeny, when crustal thickening increased the amount of assimilation of crustal material during  
641 emplacement (Figure 15).

642 The Boboti pluton contained two zircon grains which were partially (~95 %) concordant at ~3.0 and 3.4  
643 Ga respectively. Very little Archaean material has previously been reported in Birimian terranes. However,  
644 the Birimian is bounded by older Archaean domains, which may conceivably have been reworked during arc  
645 formation, basin opening and terrane accretion. The Leo-Man Rise, to the south of the KKI contains units  
646 between 3540 to 3050 Ma (Thiéblemont et al., 2004). Inherited material from the Boboti pluton fall within  
647 this age range. Begg et al., (2009) reported tomographic data which suggested the presence of reworked  
648 Archaean crust and subcontinental lithospheric mantle beneath large portions of the West Africa Craton.  
649 Such material may be reworked by melts generated in the lower crust or upper mantle. Alternatively, Lebrun

650 et al. (2015) reported the presence of Archaean derived clasts of banded iron formation within the Birimian  
651 aged Kintinian conglomerates of the Siguiri Basin in Southern Mali. Similar detrital material could  
652 conceivably have been present in the country rocks in to which the Boboti pluton intruded. This material  
653 may then have been incorporated during emplacement. While two zircon grains cannot be considered  
654 statistically significant and contamination cannot be wholly ruled out, there may be scope for future  
655 investigation into possible crustal contamination from Archaean terranes.

### 656 8.3 Temporal constraints on tectonic setting

657 The igneous rocks of the KKI show some distinct variation in their trace, REE and major element  
658 chemistry, which cannot wholly be attributed to the affinity of their host terranes (i.e. belt versus basin-type  
659 plutons). As an example, the minor felsic stocks that intruded the Balangouma and Boboti plutons are  
660 distinctly more evolved than their hosts, with peraluminous A/CNK, fractionated REE patterns and distinct Eu  
661 anomalies. It is therefore necessary to examine these geochemical variations in a temporal rather than  
662 spatial context.

663 In Figure 19 several geochemical parameters have been plotted against absolute ages of plutons from  
664 across the KKI. The data show a distinct positive trend in Dy/Yb values with time indicating an increasing  
665 control on REE patterns by residual garnet in the magma source (Davidson et al., 2013). This indicates  
666 sufficient thickening of the lithosphere to allow garnet to become stable in the magma source region. The  
667 trend of decreasing  $Eu^*$  with time reflects fractional crystallisation of Ca-plagioclase. Higher Nb/Zr and  
668 La/Sm reflect increasing HFSE and LREE enrichment, respectively. The positive trend in these two ratios  
669 represents increase in the concentration of incompatible elements as the magmas become more evolved  
670 and collision begins to take place (c.f. Draut and Clift, 2001). Rb content in magmas is increased by partial  
671 crustal melts, combined with further enhancement due to addition of a Rb-rich volatile component (Pearce  
672 et al., 1984; Pearce, 1996). Increase in the Rb content of igneous rocks in the KKI over time reflects the  
673 transition from volcanic arc to syn-collision magmatism (Figure 17A). The overall positive  $\epsilon_{Nd}(2.1Ga)$  values  
674 may be explained by the juvenile nature of the newly formed Birimian crust (Abouchami et al., 1990; Boher

675 et al., 1992; Pawlig et al., 2006; Ngom et al., 2009). However,  $\epsilon_{\text{Nd}}(2.1\text{Ga})$  data (from Boher et al., 1992; Pawlig  
676 et al., 2006) shows a general trend toward lower positive values, indicating a greater contribution of  
677 continental derived sediment with time (c.f. Draut and Clift, 2001). In addition, the time difference between  
678 Nd model ages (Boher et al., 1992; Pawlig et al., 2006) and absolute ages of crystallisation increases with  
679 time, suggesting that more evolved melts began to stall in the thickened crust (Brown and Rushmer, 2006).

680 While there are some anomalously evolved rocks present in the older Mako sequences, in general Figure  
681 19 shows a trend with time towards more evolved magmas with a greater contribution of sediments. This  
682 represents thickening of the newly formed Birimian crust as the volcanic island arc became accreted and  
683 collisional magmatism set in.

#### 684 8.4 Comparisons to other Birimian terranes

685 The majority of previous research has concluded that the growth of Birimian crust initially took place in  
686 an oceanic setting, with immature island arcs evolving to continental arcs through a process of subduction  
687 generated magmatism and terrane accretion (Sylvester and Attoh, 1992; Abouchami et al., 1990 and Boher  
688 et al., 1992; Salah et al., 1996; Dia et al., 1997; Pawlig et al., 2006; Baratoux et al., 2011; Tshibubudze et al.,  
689 in press). Granitoid rocks in Cote D'Ivoire (Poulet et al., 2006), Burkina Faso (Tapsoba et al., 2012), Niger  
690 (Salah et al., 1996) and Ghana (Sylvester and Attoh, 1992) all display geochemical characteristics consistent  
691 with those described in the KKI (REE fractionation and negative Nb-Ta, P, Ti and Eu anomalies). Many  
692 igneous units throughout the Birimian are described as tonalite–trondhjemite–granodiorite series (TTG; e.g.  
693 Soumaila et al., 2008; Vidal et al., 2009; de Kock et al., 2011; Baratoux et al., 2011; Tapsoba et al., 2012;  
694 Tshibubudze et al., in press). This is not the case for the plutonic rocks in the eastern KKI where tonalitic  
695 compositions result from widespread alkali metasomatism (Figure 5). As described in the MVB, the majority  
696 of Birimian volcanic belts feature a lower sequence of tholeiitic rocks (Abouchami et al., 1990; Sylvester and  
697 Attoh, 1992; Salah et al., 1996; Feybesse et al., 2006). These are entirely lacking in the FVB. The only truly  
698 mafic volcanic to sub-volcanic rocks observed in the south-eastern KKI are those of the Daléma suite. There  
699 is little to compare the Daléma igneous rocks to in the wider Craton, though Dampare (2008) reported a

700 probable back-arc setting for tholeiitic basaltic andesite in the southern Ashanti Belt. Similarly, back-arc  
701 settings have been suggested for Birimian rocks in SW Niger (Soumaila et al., 2008) and in Cote Di'Ivoire  
702 (Vidal and Alric, 1994). This suggests that extensional arc settings are likely to have occurred elsewhere in  
703 the Baoulé-Mossi domain.

704 Though early volcanism in the KKI is not well constrained, inherited zircons in the MVB and FVB suggest  
705 that magmatism took place at ca. 2200 Ma related to coeval volcanism. This agrees with whole rock Sm-Nd  
706 ages of volcanic rocks in Ghana ( $2266 \pm 2$  to  $2132 \pm 3$  Ma; Taylor et al., 1992; Davis et al., 1994; de Kock et  
707 al., 2011) as well as U-Pb zircon data from TTG suites in Burkina Faso ( $2203 \pm 12$  Ma and  $2207 \pm 38$  Ma;  
708 Tshibubudze et al., in press) and in south western Niger ( $2174 \pm 4$  Ma; U-Pb zircon; Soumaila et al., 2008).  
709 Alternatively, these inherited zircons may represent basement material. Crystallisation ages of Pre-Birimian  
710 gneiss in the Oudalan-Gorouol belt in NE Burkina have been reported by Tshibubudze et al.,(2013) at  $2253 \pm$   
711  $9$  Ma to  $2255 \pm 26$  Ma (U-Pb zircon). In addition, detrital zircons in micaschists from south western Niger  
712 indicate the presence of a calc-alkali protolith between 2273 and 2278 Ma (U-Pb ages; Soumaila et al., 2008).

713 In Ghana (Leube et al., 1990; Oberthür et al., 1998; Davis et al., 1994), Burkina Faso (Roddaz et al., 2007;  
714 Baratoux et al., 2011; Tshibubudze et al., in press) and the KKI (Hirdes and Davis, 2002), sedimentation and  
715 belt magmatism overlap , suggesting that the basins are lateral facies equivalents of the volcanic arcs.  
716 Crystallisation of the Badon batholith, SAG and SLPC occurred between 2200 and 2150 Ma, matching the age  
717 range of belt-type plutons in Ghana (White et al., 2014 and references therein) and Burkina Faso  
718 (Tshibubudze et al., in press). The two-phase Eburnean model applied elsewhere in the Birimian (Allibone et  
719 al., 2002; Tshibubudze et al., 2009; Hein, 2010; de Kock et al., 2011) is also applicable in the KKI. Two distinct  
720 peaks in magmatic zircon abundance occur at 2150 and 2075 Ma, the majority of age data for the KKI fall  
721 between these peaks and likely represent the main phase of Eburnean magmatism. An older peak around  
722 2200 Ma may represent the pre-Eburnean event (Eoeburnean, Eburnean I, Tangaeen) described in other  
723 Birimian terranes (Allibone et al., 2002; Tshibubudze et al., 2009; Hein, 2010; de Kock et al., 2011). With the

724 exception of inherited zircons from the Boboti pluton, material of this age is entirely lacking in the area of  
725 the south-eastern KKI studied. In

726 The general trend of increasingly felsic, peraluminous magmatism through time, as a result of crustal  
727 thickening, seems common throughout the Birimian (e.g. Ama Salah et al., 1996; Perrouty et al., 2012;  
728 Tapsoba et al., 2012).

## 729 9 Conclusions

730 The igneous rocks that define the eastern KKI are dominantly of high-K calc-alkaline affinity. Though in  
731 some units, this affinity is masked by albitisation. Nevertheless, use of the Th-Co diagram of Hastie et al.  
732 (2007) shows that all igneous units, prior to albitisation, belonged to the high-K calc-alkaline series. Indeed,  
733 the Falémé Volcanic Belt altogether lacks the tholeiitic igneous units common to other Birimian belts.

734 Fractionated REE patterns and ubiquitous negative Nb-Ta anomalies suggest a tectonic setting analogous  
735 to modern volcanic arcs and active continental margins. Furthermore, changes in trace element ratios, Eu-  
736 anomaly and  $\epsilon_{Nd,t}$  over  $\sim 200$  Ma (Figure 19) reveal the tectonic setting in the KKI to have evolved from a  
737 volcanic arc environment to an active continental margin, with more peraluminous, granitic melts  
738 developing as the crust thickened. The Daléma igneous rocks on the eastern margin of the Dialé-Daléma  
739 basin are highly metaluminous and display limited LILE enrichment, with normalised HREE values close to  
740 unity. These may have formed in an extensional back arc system.

741 New U-Pb zircon age data show that the Boboti and Balangouma plutons were emplaced at  $2088.5 \pm 8.5$   
742 Ma and  $2112 \pm 13$  Ma, respectively. Zircons in the Boboti pluton showed evidence of inherited material from  
743  $2226 \pm 13$  Ma,  $\sim 3.0$  and  $3.4$  Ga. The Palaeoproterozoic age coincides with the oldest dated units in the  
744 Western Mako Belt, whereas the Archaean ages suggest the possible reworking of Archaean material either  
745 within the detrital basins or at depth beneath the Birimian crust. The available data suggest that the south-  
746 eastern KKI is one of the younger terranes in the wider Birimian, lacking any significant component (bar



747 inherited material) that correlates to earlier Birimian events (>2150 Ma) either in the Mako Belt or in Ghana  
748 and Burkina Faso.

749 Acknowledgements

750 The Authors wish to thank Randgold Resources for generously funding this research. Additional thanks  
751 must go to technical staff at Kingston University and to Andrew Miles and Philip Bird who provided helpful  
752 discussion while preparing the manuscript. Constructive reviews by L. Baratoux, K. Hein and the Editor J.  
753 Miller are also gratefully acknowledged.

754 References

755 Abouchami, W., Boher, M., Michard, A. Albarede, F., 1990. A major 2.1 Ga event of mafic magmatism in  
756 West Africa: an early stage of crustal accretion. *Journal of Geophysical Research* 95, 17605-17629.

757 Allibone, A., Teasdale, J., Cameron, G., Etheridge, M., Uttley, P., Soboh, A., Appiah-Kubi, J., Adanu, A.,  
758 Arthur, R., Mamphey, J., Odoom, B., Zuta, J., Tsikata, A., Pataye, F. Famiyeh, S., 2002. Timing and structural  
759 controls on gold mineralisation at the Bogoso gold mine, Ghana, West Africa. *Economic Geology* 97, 949-  
760 969.

761 Baier, J., Audétat, A., Keppler, H., 2008. The origin of the negative niobium tantalum anomaly in  
762 subduction zone magmas. *Earth and Planetary Science Letters* 267, 290-300.

763 Baratoux, L., Metelka, V., Naba, S., Jessell, M. W., Grégoire, M., Ganne, J., 2011. Juvenile  
764 Paleoproterozoic crust evolution during the Eburnean orogeny (~ 2.2–2.0 Ga), western Burkina Faso.

765 *Precambrian Research* 191, 18-45.

766 Bassot, J.P. and Caen-Vachette, M., 1984. Données géochronologiques et géochimiques nouvelles sur les  
767 granitoides de l'Est du Sénégal: implications sur l'histoire géologique du Birrimien de cette région. In: Klerkx,  
768 J. and Michot, J. (Eds.), African Geology. Tervuren, Belgium, pp. 196-209.

769 Bassot, J. P., Dommangeat, A., 1986. Mise en évidence d'un accident majeur affectant le Protérozoïque  
770 inférieur des confins Sénégal-Maliens: new data on an important fault in lower Proterozoic on the borders  
771 of Senegal and Mali, Comptes Rendus De l'Académie Des Sciences. Série 2, Mécanique, Physique, Chimie,  
772 Sciences De l'Univers, Sciences De La Terre 302, 1101-1106.

773 Béziat, D., Bourges, F., Debat, P., Lompo, M., Martin, F. Tollon, F., 2000. A Palaeoproterozoic ultramafic-  
774 mafic assemblage and associated volcanic rocks of the Boromo greenstone belt: fractionates originating  
775 from island-arc volcanic in the West African Craton. Precambrian Research 101, 25-47.

776 Black, L. P., Gulson, B. L., 1978. The age of the mud tank carbonatite, strangways range, northern  
777 territory. BMR Journal of Australian Geology and Geophysics 3, 227-232.

778 Black, L. P., Kamo, S. L., Allen, C. M., Davis, D. W., Aleinikoff, J. N., Valley, J. W., Mundil, R., Campbell, I.  
779 H., Korsch, R. J., Williams, I. S. Foudoulis, C., 2004. Improved  $^{206}\text{Pb}/^{238}\text{U}$  microprobe geochronology by the  
780 monitoring of a trace-element-related matrix effect; SHRIMP, ID-TIMS, ELA-ICP-MS and oxygen isotope  
781 documentation for a series of zircon standards. Chemical Geology 205, 115-140.

782 Boher, M., Abouchami, W., Michard, A., Albarede, F. Arndt, N.T., 1992. Crustal growth in West Africa at  
783 2.1 Ga. Journal of Geophysical Research 97, 345-369.

784 Bonhomme, M., 1962. Contribution à l'étude géochronologique de la plate-forme de l'Ouest africain.  
785 Ph.D. Thesis, University of Clermont-Ferrand, France, 62 pp.

786 Brenan, J. M., Shaw, H. F., Phinney, D. L., Ryerson, F. J., 1994. Rutile-aqueous fluid partitioning of Nb, Ta,  
787 Hf, Zr, U and Th: implications for high field strength element depletions in island-arc basalts. Earth and  
788 Planetary Science Letters 128, 327-339.

789 Brown, M., Rushmer, T., 2006. Evolution and differentiation of the continental crust. Cambridge  
790 University Press, 564 p.

791 Dabo, M., Aïfa, T., 2010. Structural styles and tectonic evolution of the Kolia-Boboti sedimentary Basin,  
792 Kédougou-Kéniéba inlier, eastern Senegal. *Comptes Rendus Geoscience* 342, 796-805.

793 Dampare, S. B., Shibata, T., Asiedu, D. K., Osaë, S., Banoeng-Yakubo, B., 2008. Geochemistry of  
794 Paleoproterozoic metavolcanic rocks from the southern Ashanti volcanic belt, Ghana: petrogenetic and  
795 tectonic setting implications. *Precambrian Research* 162, 403-423.

796 Davidson, J., Turner, S., Plank, T., 2013. Dy/Dy\*: variations arising from mantle sources and petrogenetic  
797 processes. *Journal of Petrology* 54, 525-537.

798 Davis, D.W., Hirdes, W., Schaltegger, U. Nunoo, E.A., 1994. U-Pb age constraints on deposition and  
799 provenance of Birimian and gold-bearing Tarkwaian sediments in Ghana, West Africa. *Precambrian Research*  
800 67, 89-107.

801 De Kock, G. S., Armstrong, R. A., Siegfried, H. P., Thomas, E. 2011. Geochronology of the Birim  
802 Supergroup of the West African craton in the Wa-Bolé region of west-central Ghana: Implications for the  
803 stratigraphic framework. *Journal of African Earth Sciences* 59, 1-40.

804 Debat, P., Diallo, D. P., Ngom, P. M., Rollet, M., Seyler, M., 1984. La série de Mako dans ses parties  
805 centrale et méridionale (Sénégal oriental, Afrique de l'Ouest). précisions sur l'évolution de la série  
806 volcanosédimentaire et données géochimiques préliminaires sur les formations magmatiques post-  
807 tectoniques', *Journal of African Earth Sciences* 2 , 71-79.

808 Delor, C., Couëffé, R., Goujou, J. C., Diallo, D. P., Théveniaut, H., Fullgraf, T., Ndiaye, P.M., Dioh, E., Blein  
809 O., Barry, T.M.M., Le Métour, J., Martelet, G., Sergeev, S., Wemmer, K., 2010. Notice explicative de la carte  
810 géologique à 1/200 000 du Sénégal, feuille Saraya-Kédougou Est. Ministère des Mines, de l'Industrie, de  
811 l'Agro-Industrie et des PME, Direction des Mines et de la Géologie, Dakar.

- 812 Dia, A., 1985. Le complexe plutonique de lamina: Un exemple d'associations acide - basique dans le  
813 massif de granitoids de Kakadian (Sénégal est), 13<sup>th</sup> Colloquium of African Geology, Abstracts 13, 64.
- 814 Dia, A. 1988. Caractères et significations des complexes magmatiques et métamorphiques du secteur de  
815 Sandikounda–Lamina (nord de la boutonnière de Kédougou, est Sénégal). un modèle géodynamique du  
816 birimien de l'Afrique de l'Ouest, Unpublished PhD Thesis, University of Dakar, Sénégal, .
- 817 Dia, A., Van Schmus, W.R. Kröner, A., 1997. Isotopic constraints on the age and formation of a  
818 Palaeoproterozoic volcanic arc complex in the Kédougou inlier, eastern Senegal, West Africa. Journal of  
819 African Earth Sciences 24, 197-213.
- 820 Diallo, D.P., 2001. Le paléovolcanisme de la bordure occidentale de la boutonnière de Kédougou,  
821 Paléoprotérozoïque du Sénégal oriental: incidences géotectoniques. Journal of African Earth Sciences 32,  
822 919-940.
- 823 Dioh, E., Béziat, D., Debat, P., Grégoire, M. Ngom, P.M., 2006. Diversity of the Palaeoproterozoic  
824 granitoids of the Kédougou inlier (eastern Senegal): Petrographical and geochemical constraints. Journal of  
825 African Earth Sciences 44, 351-371.
- 826 Dommanget, A., Milesi, J.P. Diallo, M., 1993. The Loulo gold and tourmaline-bearing deposit. Mineralium  
827 Deposita 28, 253-263.
- 828 Drake, M. J., 1975. The oxidation state of europium as an indicator of oxygen fugacity. Geochimica et  
829 Cosmochimica Acta 39, 55-64.
- 830 Draut, A. E., Clift, P. D. 2001. Geochemical evolution of arc magmatism during arc-continent collision,  
831 South Mayo, Ireland. Geology 29, 543-546.

832 Feybesse, J. Milési, J.P., 1994. The Archaean/Proterozoic contact zone in West Africa: a mountain belt of  
833 decollement thrusting and folding on a continental margin related to 2.1 Ga convergence of Archean  
834 cratons? *Precambrian Research* 69, 199-227.

835 Feybesse, J., Billa, M., Guerrot, C., Duguey, E., Lescuyer, J., Milési, J.P. Bouchot, V., 2006. The  
836 Palaeoproterozoic Ghanaian province: Geodynamic model and ore controls, including regional stress  
837 modelling. *Precambrian Research* 149, 149-196.

838 Ganne, J., De Andrade, V., Weinberg, R. F., Vidal, O., Dubacq, B., Kagambega, N., Naba, S., Baratoux, L.,  
839 Jessell, M. Allibon, J., 2011. Modern-style plate subduction preserved in the Palaeoproterozoic West African  
840 craton. *Nature geoscience* 5, 60-65.

841 Goujou, J. C., Buscaïl, F., Théveniaut, H., Dioh, E., Delor, C., Blein, O., Diallo, D.P., Ndiaye, P.M., Le  
842 Métour, J., Fullgraf T., Caby, R., Couëffé, R., Martelet, G., Sergeev, S., Tegye, M., Villeneuve, M., Wemmer,  
843 K., 2010. Notice explicative de la carte géologique à 1/200 000 du Sénégal, feuille Kossanto-Dalafi Est, 2010,  
844 Ministère des Mines, de l'Industrie, de l'Agro-Industrie et des PME. Direction des Mines et de la Géologie,  
845 Dakar. Gueye, M., Siegesmund, S., Wemmer, K., Pawlig, S., Drobe, M., Nolte, N. Layer, P., 2007. New evidence  
846 for an early Birimian evolution in the West African Craton: an example from the Kédougou-Kéniéba inlier,  
847 southeast Senegal. *South African Journal of Geology* 110, 511-534.

848 Gueye, M., Ngom, P.M., Diene, M., Thiam, Y., Siegesmund, S., Wemmer, K. Pawlig, S., 2008. Intrusive  
849 rocks and tectono-metamorphic evolution of the Mako Palaeoproterozoic belt (Eastern Senegal, West Africa).  
850 *Journal of African Earth Sciences* 50, 88-110.

851 Hastie, A. R., Kerr, A. C., Pearce, J. A., Mitchell, S. F., 2007. Classification of altered volcanic island arc  
852 rocks using immobile trace elements: development of the Th–Co discrimination diagram. *Journal of*  
853 *Petrology* 48, 2341-2357.

854 Hastie, A. R., Mitchell, S. F., Treloar, P. J., Kerr, A. C., Neill, I., Barfod, D. N., 2013. Geochemical  
855 components in a Cretaceous island arc: The Th/La-(Ce/Ce\*)Nd diagram and implications for subduction  
856 initiation in the inter-American region. *Lithos* 162, 57-69.

857 Hein, K. A., 2010. Succession of structural events in the Goren greenstone belt (Burkina Faso):  
858 implications for West African tectonics. *Journal of African Earth Sciences* 56, 83-94.

859 Hirdes, W. Davis, D.W., 2002. U-Pb Geochronology of Palaeoproterozoic rocks in the southern part of the  
860 Kédougou-Kéniéba inlier, Senegal, West Africa: evidence for diachronous accretionary development of the  
861 Eburnean Province. *Precambrian Research* 118, 83-99.

862 Hirdes, W., Davis, D.W. Eisenlohr, B.N., 1992. Reassessment of Proterozoic granitoid ages in Ghana on  
863 the basis of U/Pb zircon and monazite dating. *Precambrian Research* 56, 89-96.

864 Hirdes, W., Davis, D.W., Ludtke, G., Konan, G., 1996. Two generations of Birimian (Paleoproterozoic)  
865 volcanic belts in northeastern Cote d'Ivoire (West Africa): consequences for the 'Birimian controversy'.  
866 *Precambrian Research* 80, 173-191.

867 Jackson, S.E., Pearson, N.J., Griffin, W.L., Belousova, E.A., 2004. The application of laser ablation-inductively  
868 coupled plasma-mass spectrometry to in situ U-Pb zircon geochronology. *Chemical Geology* 211, 47-69.

869

870 John, T., Klemd, R., Hirdes, W. Loh, G., 1999. The metamorphic evolution of the Palaeoproterozoic  
871 (Birimian) volcanic Ashanti belt (Ghana, West Africa). *Precambrian Research* 98, 11-30.

872 Junner, N.R., 1940. Geology of the Gold Coast and Western Togoland. Gold Coast Geological Survey  
873 Bulletin 11, 1-40.

874 Lawrence, D.M., Treloar P.J., Rankin, A.H., Harbidge, P., Holliday, J., 2013a The Geology and Mineralogy  
875 of the Loulo Mining District, Mali, West Africa: Evidence for Two Distinct Styles of Orogenic Gold  
876 Mineralization. *Economic Geology* 108, 199-227.

877 Lawrence, D.M., Treloar, P.J., Rankin, A.H., Boyce, A., Harbidge, P., 2013b, A fluid inclusion and stable  
878 isotope study at the Loulo mining district, Mali, West Africa: Implications for multifluid sources in the  
879 generation of orogenic gold deposits. *Economic Geology* 107, 229–257.

880 Le Maitre, R. W. 1989. A classification of igneous rocks and glossary of terms. Recommendations of the  
881 International Union of Geological Sciences, Sub-commission on the Systematics of Igneous rocks: Oxford,  
882 Blackwell.

883 Lebrun, E., Thébaud, N., Miller, J., Bourget, J., Ulrich, S., Terblanche, O., 2015. Geochronology and  
884 lithostratigraphy of the Siguiiri district: implications for gold mineralisation in the Siguiiri Basin (Guinea, West  
885 Africa). 13<sup>th</sup> SGA Biennial Meeting, Nancy, France, 1-4. Ledru, P., Pons, J., Milesi, J. P., Feybesse, J. L. Johan, V.,  
886 1991. Transcurrent tectonics and polycyclic evolution in the lower Proterozoic of Senegal-Mali, *Precambrian*  
887 *Research* 50, 337-354.

888 Leube, A., Hirdes, W., Mauer, R., Kesse, G.O. 1990. The early Proterozoic Birimian Supergroup of Ghana  
889 and some aspects of its associated gold mineralisation. *Precambrian Research* 46, 139-165.

890 Loh, G., Hirdes, W., Anani, C., Davis, D.W., Vetter, U., 1999. Explanatory notes for the geological map of  
891 Southwest Ghana 1: 100,000. *Geologisches Jahrbuch B* 93, 150.

892 Ludwig, K. R., 2003. User's manual for Isoplot 3.00: A geochronological toolkit for Microsoft Excel (No. 4).  
893 Kenneth R. Ludwig, 76 .p

894 Maniar, P.D., Piccoli, P.M., 1989. Tectonic discrimination of granitoids. *Geological Society of America*  
895 *Bulletin* 101, 635-643.

896 Milési, J.P., Feybesse, J.L., Ledru, P., Dommaget, A., Ouedrago, M., Marcoux, E., Prost, A., Vinchon, C.,  
897 Sylvain, J.P., Johan, V., Tegye, M., Calvez, J.Y. Lagny, P., 1989. West African gold deposits in their Lower  
898 Proterozoic lithostructural setting. *Chronique de la Recherche Minière* 497, 3-98.

899 Müller, W., Shelley, M., Miller, P., Broude, S., 2009. Initial performance metrics of a new custom-  
900 designed ArF excimer LA-ICPMS system coupled to a two-volume laser-ablation cell. *Journal of Analytical*  
901 *Atomic Spectrometry* 24, 209-214.

902 Ngom, P. M., Cordani, U. G., Teixeira, W. Janasi, V. A., 2009. Sr and nd isotopic geochemistry of the early  
903 ultramafic–mafic rocks of the Mako bimodal volcanic belt of the Kedougou-Kéniéba Inlier (Senegal). *Arabian*  
904 *Journal of Geosciences* 3 , 49-57.

905 Oberthür, T., Vetter, U., Davis, D.W. Amanor, J.A., 1998. Age constraints on gold mineralisation and  
906 Palaeoproterozoic crustal evolution in the Ashanti belt of southern Ghana. *Precambrian Research* 89, 129-  
907 143.

908 Parra-Avila, L. A., Belousova, E., Fiorentini, M. L., Baratoux, L., Davis, J., Miller, J., McCuaig, T. C., 2015.  
909 Crustal evolution of the Paleoproterozoic Birimian terranes of the Baoulé-Mossi domain, southern West  
910 African Craton: U–Pb and Hf-isotope studies of detrital zircons. *Precambrian Research*.  
911 [doi:10.1016/j.precamres.2015.09.005](https://doi.org/10.1016/j.precamres.2015.09.005).

912 Paton, C., Woodhead, J. D., Hellstrom, J. C., Hergt, J. M., Greig, A., Maas, R., 2010. Improved laser  
913 ablation U-Pb zircon geochronology through robust downhole fractionation correction. *Geochemistry,*  
914 *Geophysics, Geosystems* 11, Q0AA06, doi:10.1029/2009GC002618.

915 Pawlig, S., Gueye, M., Klisches, R., Schwarz, S., Wemmer, K. Siegesmund, S., 2006. Geochemical and Sr-  
916 Nd isotopic data on the Birimian of the Kédougou-Kéniéba Inlier (Eastern Senegal): Implications on the  
917 Palaeoproterozoic evolution of the West African Craton. *South African Journal of Geology* 109, 411-427.

918 Pearce, J. A., 1996. Sources and settings of granitic rocks. *Episodes* 19, 120-125.



- 919 Pearce, J. A., 2008. Geochemical fingerprinting of oceanic basalts with applications to ophiolite  
920 classification and the search for Archean oceanic crust. *Lithos* 100, 14-48.
- 921 Pearce, J.A., Harris, N.B. Tindle, A.G., 1984. Trace element discrimination diagrams for the tectonic  
922 interpretation of granitic rocks. *Journal of Petrology* 25, 956-983.
- 923 Pearce, J. A., Peate, D. W., 1995. Tectonic implications of the composition of volcanic arc magmas.  
924 *Annual Review of Earth and Planetary Sciences* 23, 251-286.
- 925 Perrouty, S., Aillères, L., Jessell, M. W., Baratoux, L., Bourassa, Y., Crawford, B., 2012. Revised Eburnean  
926 geodynamic evolution of the gold-rich southern Ashanti Belt, Ghana, with new field and geophysical  
927 evidence of pre-Tarkwaian deformations. *Precambrian Research* 204, 12-39.
- 928 Plank, T., 2005. Constraints from thorium/lanthanum on sediment recycling at subduction zones and the  
929 evolution of the continents. *Journal of Petrology* 46, 921-944.
- 930 Pouclet, A., Doumbia, S. Vial, D.S., 2006. Geodynamic setting of the Birimian volcanism in central Ivory  
931 Coast (western Africa) and its place in the Palaeoproterozoic evolution of the Man Shield. *Bulletin Societe*  
932 *Geologique de France* 177, 105-121.
- 933 Rickwood, P.C., 1989. Boundary lines within petrologic diagrams which use oxides of major and minor  
934 elements. *Lithos* 22, 247-263.
- 935 Roddaz, M., Debat, P. Nikiéma, S., 2007. Geochemistry of Upper Birimian sediments (major and trace  
936 elements and Nd–Sr isotopes) and implications for weathering and tectonic setting of the Late  
937 Palaeoproterozoic crust. *Precambrian Research* 159, 197-211.
- 938 Salah, I. A., Liegeois, J. P., Pouclet, A., 1996. Evolution d'un arc insulaire océanique birimien précoce au  
939 Liptako nigérien (Sirba): géologie, géochronologie et géochimie. *Journal of African Earth Sciences* 22, 235-  
940 254.

- 941 Schwartz, M.O. Melcher, F., 2004. The Falémé Iron District, Senegal. *Economic Geology* 99, 917-939.
- 942 Sláma, J., Košler, J., Condon, D. J., Crowley, J. L., Gerdes, A., Hanchar, J. M., Horstwood, M. S. A., Morris,  
943 G. A., Nasdala, L., Norberg, N., Schaltegger, U., Schoene, B., Tubrett, M. N. Whitehouse, M. J., 2008.  
944 Plešovice zircon—a new natural reference material for U–Pb and Hf isotopic microanalysis. *Chemical*  
945 *Geology* 249, 1-35.
- 946 Soumaila, A., Henry, P., Garba, Z., Rossi, M., 2008. REE patterns, Nd-Sm and U-Pb ages of the  
947 metamorphic rocks of the Diagorou-Darbani greenstone belt (Liptako, SW Niger): implication for Birimian  
948 (Palaeoproterozoic) crustal genesis. Geological Society, London, Special Publications 297, 19-32.
- 949 Sun, S.S. McDonough, W. F., 1989. Chemical and isotope systematics of oceanic basalts: implications for  
950 mantle composition and processes, in: SAUNDERS, A. D. and NORRY, M. J. (Eds.) *Magmatism in the Ocean*  
951 *Basins*. Geological Society, London, Special Publications 42, 313-345.
- 952 Sylvester, P.J. Attoh, K., 1992. Lithostratigraphy and composition of 2.1 Ga greenstone belts of the West  
953 African Craton and their bearing on crustal evolution and the Archean-Proterozoic boundary. *Journal of*  
954 *Geology* 100, 377-393.
- 955 Tapsoba, B., Lo, C. H., Jahn, B. M., Chung, S. L., Wenmenga, U., Iizuka, Y., 2013. Chemical and Sr–Nd  
956 isotopic compositions and zircon U–Pb ages of the Birimian granitoids from NE Burkina Faso, West African  
957 Craton: Implications on the geodynamic setting and crustal evolution. *Precambrian Research* 224, 364-396.
- 958 Taylor, B., Martinez, F., 2003. Back-arc basin basalt systematics. *Earth and Planetary Science Letters* 210,  
959 481-497.
- 960 Taylor, P.N., Moorbath, S., Leube, A. Hirdes, W., 1992. Early Proterozoic crustal evolution in the Birimian  
961 of Ghana: constraints from geochronology and isotope geochemistry. *Precambrian Research* 56, 97-111.

- 962 Thiéblemont, D., Goujou, J. C., Egal, E., Cocherie, A., Delor, C., Lafon, J. M., Fanning, C. M., 2004. Archean  
963 evolution of the Leo Rise and its Eburnean reworking. *Journal of African Earth Sciences* 39, 97-104.
- 964 Treloar, P. J., Lawrence, D. M., Senghor, D., Boyce, A., Harbidge, P., 2014. The Massawa gold deposit,  
965 Eastern Senegal, West Africa: an orogenic gold deposit sourced from magmatically derived fluids? *Geological*  
966 *Society, London, Special Publications* 393, SP393-12.
- 967 Tshibubudze, A., Hein, K. A., Marquis, P., 2009. The Markoye Shear Zone in NE Burkina Faso. *Journal of*  
968 *African Earth Sciences* 55, 245-256. Tshibubudze, A., Hein, K. A. A., Peters, L. F. H., Woolfe, A. J., McCuaig, T.  
969 C., 2013. Oldest U-Pb crystallisation age for the West African craton from the Oudalan-Gorouol Belt of  
970 Burkina Faso. *South African Journal of Geology* 116, 169-181.
- 971 Tshibubudze, A., Hein, K. A., McCuaig, T. C. (In Press). The relative and absolute chronology of strato-tectonic  
972 events in the Gorom-Gorom granitoid terrane and Oudalan-Gorouol belt, northeast Burkina Faso. *Journal*  
973 *of African Earth Sciences*.
- 974 Vidal, M. Alric, G., 1994. The Palaeoproterozoic (Birimian) of Haute-Comoé in the West African Craton,  
975 Ivory Coast: a transtensional back-arc basin. *Precambrian Research* 65, 207-229.
- 976 Vidal, M., Gumiaux, C., Cagnard, F., Pouclet, A., Ouattara, G., Pichon, M., 2009. Evolution of a  
977 Paleoproterozoic “weak type” orogeny in the West African Craton (Ivory Coast). *Tectonophysics* 477, 145-  
978 159.
- 979 White, A., Burgess, R., Charnley, N., Selby, D., Whitehouse, M., Robb, L., Waters, D., 2014. Constraints on  
980 the timing of late-Eburnean metamorphism, gold mineralisation and regional exhumation at Damang mine,  
981 Ghana. *Precambrian Research* 243, 18-38.
- 982 Wiedenbeck, M., Hanchar, J. M., Peck, W. H., Sylvester, P., Valley, J., Whitehouse, M., Kronz, A.,  
983 Morishita, Y., Nasdala, L., Fiebig, J., Franchi, I., Girard, J.-P., Greenwood, R.C., Hinton, R., Kita, N., Mason,  
984 P.R.D., Norman, M., Ogasawara, M., Piccoli, P.M., Rhede, D., Satoh, H., Schulz-Dobrick, B., Skår, O., Spicuzza,

985 Mj., Terada, K., Tindle, A., Togashi, S., Vennemann, T., Xie, Q. Zheng, Y.-F., 2004. Further Characterisation of  
986 the 91500 Zircon Crystal. *Geostandards and Geoanalytical Research* 28, 9–39.

987 Figures

988 Figure 1. Geological map of the Kédougou-Kéniéba Inlier, including units of the Mako belt referred to in  
989 the text (modified after Lawrence, 2010).

990 Figure 2. Detailed geology of the Falémé Volcanic Belt and Kofi Series, locations of whole-rock  
991 geochemistry samples are indicated.

992 Figure 3. Hand specimen photographs of: A) medium grained diorite (BP31); B) porphyritic basaltic  
993 andesite (CLIB08); C) phaneritic gabbroic diorite (CLIB09); D) coarse gabbroic diorite with biotite phenocrysts  
994 (CLIB10); E) sheared quartz monzodiorite from near the sheared contact between the FVB and Kofi series  
995 (CLIB01); F) a coarse grained quartz monzonite with K-feldspar phenocrysts (CLIB05); G) an aplite dyke  
996 (CLIB06) that cross-cuts the Balangouma pluton; H) a coarse porphyritic monzonite (CLIB07).

997 Figure 4. Hand specimen photographs of: A) coarse porphyritic quartz monzodiorite (BOP1A); B)  
998 porphyritic monzogranite (BOP2 and 3); C) porphyritic pyroxene-bearing quartz diorite (BOP4); D) hand  
999 specimen of coarse grained quartz diorite (BO4); E) hand specimen of medium grained quartz diorite (BO5);  
1000 F) pink, medium-grained monzogranite (PTG1); G) equigranular monzogranite (MAD01); H) biotite-quartz-  
1001 feldspar porphyry (FDGI01).

1002 Figure 5. A)  $K_2O$  versus Silica diagram (Rickwood, 1989) showing the plutonic and volcanic units of the  
1003 eastern KKI, note the 'upper trend' represents unaltered samples of high-K calc-alkaline affinity and the  
1004 'lower' calc-alkaline to tholeiitic trend represents albitised samples, see text for details; B) Th-Co  
1005 discrimination diagram (Hastie et al., 2007) showing albitised and fresh samples plotting in the high-K and  
1006 upper calc-alkaline series.

1007 Figure 6. Geochemical samples plotted on total alkali silica (TAS) classification diagram (after Le Maitre  
1008 et al., 1989) showing lithology names for: A) intrusive-plutonic samples and B) extrusive (volcanic) from the  
1009 FVB and Kofi Series.

1010 Figure 7. A/NK versus A/CNK diagram (after Maniar and Piccoli, 1989) for igneous rocks from the eastern  
1011 KKI. Albitised samples are highlighted in red, note that albitisation results in lower A/NK values due to  
1012 increase in overall  $N_2O$ .

1013 Figure 8. N-MORB normalised REE patterns for A) the Daléma Igneous rocks from the eastern margin of  
1014 the Diale-Dalema Basin; B) the intermediate composition (diorite to granodiorite) igneous rocks of the FVB  
1015 and Kofi Series (see key); C) the granitic rocks of the FVB and Kofi Series. N-MORB normalised trace element  
1016 diagrams of for D) the Daléma Igneous rocks from the eastern margin of the Diale-Dalema Basin; E) the  
1017 intermediate composition (diorite to granodiorite) igneous rocks of the FVB and Kofi Series (see key); F) the  
1018 granitic rocks of the FVB and Kofi Series, note the consistent depletion of Nb-Ta compared to other HFSE.  
1019 Albitised samples were excluded from multi-element plots (D, E and F) due to extreme perturbation of the  
1020 trace element patterns.

1021 Figure 9. Representative SEM-CL images of: A) and B) zircons from sample BOP1A of the Boboti Pluton;  
1022 C) and D) zircons BOP1A-09 and BOP1A-22 from the Boboti pluton with U-Pb ages indicated inheritance at  
1023  $\sim 2200$  Ma (BOP1A; ages given are from  $^{206}\text{Pb}/^{238}\text{U}$ ); E) and F) zircons BOP1A-73 and BOP1A-75 with ablation  
1024 spots marked; G) and H) zircons from sample CLIB01 of the Balangouma Pluton; I) and J) zircons from sample  
1025 CLIB05 of the Balangouma Pluton K) and L) zircons from sample CLIB07 of the Balangouma Pluton

1026 Figure 10. A) Concordia diagram showing discordia plotted from 70 concordant and discordant grains  
1027 from sample BOP1A of the Boboti pluton, the discordia trends toward the origin and is likely a result of  
1028 recent Pb-loss; B) Diagram of the weighted mean  $^{206}\text{Pb}/^{238}\text{U}$  age of 19 concordant grains from BOP1A and; C)  
1029 the weighted mean  $^{207}\text{Pb}/^{206}\text{Pb}$  age of the same 19 grains from BOP1A.

1030 Figure 11. Evidence for inherited material in the Boboti pluton: A) two partially concordant grains at  
 1031 ~2230 Ma, corresponding to early volcanic activity in the Falémé Belt; B) two partially concordant Archaean  
 1032 U-Pb ages from zircons BOP1A-73 and BOP1A-75 in the Boboti pluton.

1033 Figure 12. Diagrams of A) discordia plotted from 43 ablation spots in sample CLIB01 trending toward the  
 1034 origin indicating recent Pb-loss, age of intercept is indicated; B) weighted mean of  $^{206}\text{Pb}/^{238}\text{U}$  ages from the 7  
 1035 most concordant grains; C) weighted mean  $^{207}\text{Pb}/^{206}\text{Pb}$  ages for 43 grains from CLIB01. Weighted mean ages  
 1036 and MSWD values are indicated.

1037 Figure 13. Diagrams of A) discordia plot constructed from 43 concordant and discordant grains from  
 1038 sample CLIB05, upper intercept age is indicated; B) a weighted average of the 13 most concordant  $^{206}\text{Pb}/^{238}\text{U}$   
 1039 ages from CLIB05 yielding a younger age than the discordia intercept in A; C) a weighted average of the 13  
 1040 equivalent  $^{207}\text{Pb}/^{206}\text{Pb}$  ages; D) a weighted average of 57  $^{207}\text{Pb}/^{206}\text{Pb}$  ages with 9 outliers rejected.

1041 Figure 14. Diagrams of A) discordia plotted from 56 discordant and concordant spots from CLIB07 with  
 1042 the upper intercept indicated; B) a weighted average  $^{207}\text{Pb}/^{206}\text{Pb}$  age of the same 56 spots with 6 outliers  
 1043 rejected; C) a weighted average  $^{206}\text{Pb}/^{238}\text{U}$  age calculated from the 9 most concordant spots from CLIB07.

1044 Figure 15. Th/La–(Ce/Ce\*)Nd diagram after Hastie et al. (2013) showing the affinity of slab derived  
 1045 components in the igneous rocks of the FVB and Kofi Series, albitised samples not plotted. Th/La values are  
 1046 generally inherited from subducting slab sediments, which typically have Th/La > island arc lavas and N-  
 1047 MORB.  $(\text{Ce}/\text{Ce}^*)_{\text{Nd}} = \text{Ce}_{\text{CN}}/(\text{La}_{\text{CN}}^{2/3} \times \text{Nd}_{\text{CN}}^{1/3})$ ; this reflects enrichment of Ce relative to other REEs, which  
 1048 relates to different oxidation states in the marine environment. Subducting marine sediment end members:  
 1049 SSC-HD = slow sediment clay-hydrogenous and SSC-FH = slow sediment clay-fish debris/hydrothermal, as  
 1050 described in Hastie et al., (2013).

1051 Figure 16. Dy/Dy\* vs Dy/Yb diagram of Davidson et al. (2013), this diagram describes the slope (Dy/Yb)  
 1052 and curvature (Dy/Dy\*) of REE patterns as a single point for any given sample. MORB field includes N-MORB  
 1053 and E-MORB data from the East Pacific Rise. Decreasing Dy/Dy\* values below the MORB array are largely

1054 controlled by fractionation of clinopyroxene and amphibole, whereas increasing Dy/Yb reflects increasing  
1055 control of residual garnet on REE patterns. PM, primitive mantle; DM, depleted mantle; GLOSS, average  
1056 global subducting sediment; see Davidson et al., (2013) for details. Note that data for the Dalema rocks falls  
1057 within the field for LREE enriched MORB, whereas the majority of the plutonic rocks in the FVB and Kofi plot  
1058 toward bulk crustal values or along a trend of increasing sediment contamination. The most felsic,  
1059 peraluminous units display the highest Dy/Yb values.

1060 Figure 17. The A) Rb versus (Y+Nb) and B) Ta versus Nb diagrams of Pearce et al. (1984) for  
1061 discriminating the tectonic environment of granitic rocks. Albitised samples are highlighted in red.

1062 Figure 18. Summary diagram of published age data for the KKI. Data source is indicated by the numbers  
1063 below the Belt-Series labels (1) Bassot and Caen-Vachette (1984); (2) Dia (1988); (3) Milesi et al. (1989); (4)  
1064 Calvez et al. (1990); (5) Boher et al. (1992); (6) Dia et al. (1997); (7) Hirdes and Davis (2002); (8) Gueye et al.  
1065 (2007); (9) Goujou et al., (2010); (10) Delor et al., (2010).

1066 Figure 19. Tectonic evolution of the KKI defined by the trace element chemistry and isotope  
1067 geochemistry of plutonic rocks in the FVB, Mako Belt, Saraya Batholith and Kofi Series.  $\epsilon Nd_{(2.1Ga)}$  becomes  
1068 less positive with time, indicating an increasing influence of continent derived material. Higher Nb/Zr and  
1069 La/Sm reflect increasing HFSE and LREE enrichment, respectively. Decreasing  $Eu^*$  reflects fractional  
1070 crystallisation of Ca-rich plagioclase. Increasing Dy/Yb reflects greater control on REE pattern by residual  
1071 garnet as a result of slab sediment melting. Error bars for the x-axis are  $2\sigma$ . Trace element and  
1072 geochronological data are from this study with the additional geochemical, isotopic and geochronological  
1073 data compiled from Boher et al., (1992), Pawlig et al., (2006), Dioh et al., (2006) Bassot and Caen-Vachette  
1074 (1984); Dia et al. (1997); Hirdes and Davis (2002); Gueye et al. (2007).

1075 Tables

1076 Table 1 – A summary of published geochronological data from the Kédougou-Kéniéba Inlier. Published  
1077 sources are referenced in the table.

1078 Table 2 - LA-ICPMS instrumental parameters.

1079 Table 3 – LA-MC-ICP-MS data for analyses of standard zircon materials GJ-1, Temora-2, 91500, Mud Tank  
1080 and Plešovice.

1081 Table 4 – A summary whole rock geochemical data collected from the South-eastern KKI as part of this  
1082 study.

1083 Table 5 – A summary whole rock geochemical data collected from the South-eastern KKI as part of this  
1084 study.

1085 Table 6 – A summary whole rock geochemical data collected from the South-eastern KKI as part of this  
1086 study.

1087 Table 7 – A summary whole rock geochemical data collected from the South-eastern KKI as part of this  
1088 study.

1089 Table 8 - LA-MC-ICP-MS data for analyses of sample BOP1A - Boboti pluton, quartz monzodiorite  
1090 porphyry.

1091 Table 9 - LA-MC-ICP-MS data for analyses of sample CLIB01 - Balangouma pluton, quartz monzodiorite  
1092 porphyry.

1093 Table 10 - LA-MC-ICP-MS data for analyses of sample CLIB05 – Balangouma pluton, quartz monzonite  
1094 porphyry.

1095 Table 11 - LA-MC-ICP-MS data for analyses of sample CLIB07 - Balangouma pluton, monzonite porphyry.

1096



1096 Table.1

Terrane	Unit	Method	Date (Ma)	± (Ma)	Event	Reference
Mako volcanic Belt	Badon granodiorite	Ar-Ar (biotite)	2098	20	Cooling below 300 °C	Gueye et al., (2007)
		K-Ar (biotite)	2090	9	Cooling below 300 °C	Gueye et al., (2007)
		Pb-Pb (zircon)	2213	3	Inherited core	Gueye et al., (2007)
		Pb-Pb (zircon)	2198	2	Magmatic emplacement (rim)	Gueye et al., (2007)
	SAG dioritic gneiss	Pb-Pb (zircon)	2202	6	Protolith crystallisation	Gueye et al., (2007)
	SAG tonalitic gneiss	Ar-Ar (hornblende)	2112	12	Cooling below 550 °C	Gueye et al., (2007)
		K-Ar (hornblende)	2118	31	Cooling below 550 °C	Gueye et al., (2007)
		Pb-Pb (zircon)	2194	4	Protolith crystallisation	Dia et al., (1997)
		Pb-Pb (zircon)	2194	4	Protolith crystallisation	Gueye et al., (2007)
	SLP complex diorite	Pb-Pb (zircon)	2158	8	Magmatic emplacement	Dia et al., (1997)
		SLP complex migmatite	U-Pb (zircon)	2171	9	Migmatisation
	LKP granodiorite gneiss	Pb-Pb (zircon)	2138	12	Protolith crystallisation	Dia et al., (1997)
	LKP Kaourou Pluton	Pb-Pb (zircon)	2079	6	Magmatic emplacement	Dia et al., (1997)
		Rb-Sr (WR)	2189	23	Possible inheritance	Dia et al., (1997)
	LKP Laminia Pluton	Pb-Pb (zircon)	2105	8	Magmatic emplacement	Dia (1988)
		U-Pb (zircon)	2127	6	Magmatic emplacement	Dia et al., (1997)
	Mamakono rhyolite	Pb-Pb (zircon)	2067	12	Eruption	Gueye et al., (2007)
	Mamakono granodiorite	U-Pb (zircon)	2076	3	Magmatic emplacement	Hirdes and Davis (2002)
	Granite	U-Pb (zircon)	2102	8	Magmatic emplacement	Goujou et al., (2010)
	Granite	U-Pb (zircon)	2103	11	Magmatic emplacement	Goujou et al., (2010)
	Granite	U-Pb (zircon)	2142	7	Magmatic emplacement	Delor et al., (2010)
	Andesite lava	Sm-Nd (WR)	2160	16	Eruption	Boher et al., (1992)
	Tinkoto granodiorite	Ar-Ar (hornblende)	2051	16	Cooling below 550 °C	Gueye et al., (2007)
		K-Ar (biotite)	2064	20	Cooling below 300 °C	Gueye et al., (2007)
		Pb-Pb (zircon)	2074	5	Magmatic emplacement	Gueye et al., (2007)
	Dialé-Daléma Series	Metasedimentary rocks	U-Pb (zircon)	2164.7	0.9	Upper age of sedimentation
Saraya Batholith		Ar-Ar (muscovite)	2022	12	Cooling below 350 °C	Gueye et al., (2007)
		K-Ar (muscovite)	2021	11	Cooling below 350 °C	Gueye et al., (2007)
		U-Pb (monazite)	2079	2	Magmatic emplacement	Hirdes and Davis (2002)
		U-Pb (monazite)	2064	4	Metamorphic overprint	Hirdes and Davis (2002)
		U-Pb (zircon)	2072	10	Magmatic emplacement	Delor et al., (2010)
		U-Pb (zircon)	2061	15	Magmatic emplacement	Delor et al., (2010)
		U-Pb (zircon)	2075	10	Magmatic emplacement	Goujou et al., (2010)
		Metasedimentary rocks	Pb-Pb (zircon)	2096	8	Upper age of sedimentation
		Pb-Pb (zircon)	2156	10	Upper age of sedimentation	Milesi et al., (1989)
		Andesite dyke	Pb-Pb (zircon)	2070	10	Crystallisation
		Pb-Pb (zircon)	2072	9	Crystallisation	Calvez et al., (1990)
		Rhyodacite	U-Pb (zircon)	2098	13	Eruption or crystallisation
		Balanguouma pluton	U-Pb (zircon)	2118	16	Magmatic emplacement

		U-Pb (zircon)	2105	9.8	Magmatic emplacement	This study
		U-Pb (zircon)	2113	15	Magmatic emplacement	This study
	Boboti granodiorite	U-Pb (zircon)	2080.2	0.9	Magmatic emplacement	Hirdes and Davis (2002)
		U-Pb (zircon)	2088.5	8.5	Magmatic emplacement	This study
		U-Pb (zircon)	3000	120	Inherited core	This study
		U-Pb (zircon)	3380	160	Inherited core	This study
		U-Pb (zircon)	2218	83	Inherited core	This study
	South Falémé tonalite	U-Pb (zircon)	2081.5	1.1	Magmatic emplacement	Hirdes and Davis (2002)
	Rhyolite lava	U-Pb (zircon)	2099	4	Eruption	Hirdes and Davis (2002)
	Rhyolite lava	U-Pb (zircon)	2155	34	Inheritance	Hirdes and Davis (2002)
	Bofeto rhyolite	U-Pb (zircon)	2082	8	Eruption or crystallisation	Delor et al., (2010)
	Rhyolite lava	U-Pb (zircon)	2064	30	Eruption	Delor et al., (2010)
Kofi Series	Tourmalinised quartz wacke	Pb-Pb (zircon)	2093	7	Upper age of sedimentation	Boher et al., (1992)
	Deltaic deposits	U-Pb (zircon)	2125	27	Upper age of sedimentation	Boher et al., (1992)
	Gara Au deposit	U-Pb (mon-xen)	2028	10	Mineralisation	Vielriecher (2006)
	Gamaye pluton	Rb-Sr (WR)	2045	27	Magmatic emplacement	Bassot and Caen-Vachette (1984)

1097

1098

1098 Table. 2

Laboratory & Sample Preparation	
Laboratory name	Dept. of Earth Science, Royal Holloway University of London (LA-ICPMS analyses)
Sample type/mineral	Igneous zircons
Laser ablation system	
Make, Model & type	Resonetics / ASI RESolution M-50 with Compex 110
Ablation cell & volume	Laurin two-volume cell (M-50), upper volume ~2 cm <sup>3</sup>
Laser wavelength (nm)	193nm
Pulse width (ns)	20 ns
Fluence (J.cm <sup>-2</sup> )	3 J/cm <sup>-2</sup>
Repetition rate (Hz)	5Hz
Ablation duration (secs)	30 s, 15 s background before and after
Signal smoothing	'Squid' signal smoothing device included
Spot size (µm)	34 µm
Sampling mode	Spot ablation
Carrier gas	He only through LA cell; N <sub>2</sub> & Ar carrier-gas combined before squid
Cell carrier gas flow (l/min)	850 ml/min He
ICPMS Instrument	
Make, Model & type	Agilent 7500ce
Sample introduction	Laser ablation only
RF power (W)	1200W
Carrier gas flow (l/min)	450 ml/min Ar, 6 ml/min N <sub>2</sub>
Detection system	Dual-stage detector
Masses measured	m/z = 29, 31, 139, 140, 141, 172, 175, 177, 206, 207, 208, 232, 238
Dwell time per peak (ms)	5 – 60 ms
Total sweep time per reading (ms)	202 ms
Th/ThO, <sup>232</sup> Th/ <sup>238</sup> U	<0.25%, >93 %
Data Processing	
	See text for details

1099

1100

1100 For all tables: Alb = albitised lithologies; Unalt = unaltered lithologies

1101 Table 4

Pluton/Area Sample	Alb	Alb	Unalt	Unalt	Unalt	Unalt	Unalt	Unalt	Unalt	Unalt
	LR4	WP174	CLIB05	CLIB06	CLIB07	LR5	R35	R36	R37	R41
	Balangouma									
SiO <sub>2</sub>	64.5	75.7	64.3	73.3	62.3	63.7	64.0	55.7	58.6	62.3
TiO <sub>2</sub>	0.5	0.1	0.7	0.1	0.7	0.8	0.4	0.6	0.8	0.7
Al <sub>2</sub> O <sub>3</sub>	16.2	14.7	15.6	14.9	14.9	15.6	15.6	13.9	16.4	15.4
Fe <sub>2</sub> O <sub>3</sub> T	2.2	0.1	5.0	0.6	6.0	5.7	3.8	5.0	6.6	5.3
MnO	0.0	0.0	0.1	0.0	0.1	0.1	0.1	0.1	0.1	0.1
MgO	3.1	0.1	2.2	0.2	3.4	3.1	1.7	2.5	3.5	2.7
CaO	2.8	0.2	3.5	0.8	4.6	4.4	5.1	3.8	5.1	4.2
Na <sub>2</sub> O	8.5	8.2	4.4	4.4	3.8	4.1	4.1	3.5	4.5	4.1
K <sub>2</sub> O	0.3	0.2	3.7	4.6	3.2	2.4	2.6	2.7	2.2	3.0
P <sub>2</sub> O <sub>5</sub>	0.2	0.1	0.2	0.0	0.2	0.2	0.2	0.2	0.2	0.2
LOI	0.8	0.3	0.6	0.5	0.6	0.9	1.3	11.0	1.0	0.8
Total	99.2	99.6	100.2	99.4	99.6	100.9	99.0	98.9	99.1	98.8
Sample	LR4	WP174	CLIB05	CLIB06	CLIB07	LR5	R35	R36	R37	R41
V	67.2	3.7	67.8	5.9	103.0	87.6	55.3	88.5	124.4	78.0
Cr	88.9	32.8	79.2	16.2	146.2	92.3	42.9	79.4	101.1	78.2
Co	7.2	0.0	7.2	0.0	12.5	16.6	11.7	16.6	21.7	14.5
Ni	11.8	4.1	21.8	4.9	42.0	37.6	10.7	35.2	45.5	34.3
Ga	21.7	20.9	21.8	20.9	20.6	25.0	28.7	29.7	32.7	26.5
Rb	7.1	7.5	228.3	268.3	164.9	142.5	120.6	121.2	108.1	128.0
Sr	205.8	47.2	341.2	213.1	398.7	381.6	453.0	419.0	538.4	377.1
Y	14.0	2.7	17.8	6.6	21.4	11.2	9.6	16.2	16.4	16.5
Zr	149.2	73.0	268.8	79.9	201.5	195.8	131.5	252.9	212.2	190.4
Nb	7.6	7.6	12.5	7.8	10.1	12.1	6.6	12.2	10.6	13.0
Ta	0.9	1.6	0.6	1.9	1.5	1.2	0.9	1.1	1.0	1.1
Mo	1.0	0.0	0.2	1.3	0.3	3.2	2.4	2.1	1.6	5.3
Cs	0.1	0.2	16.9	9.1	9.2	6.8	1.9	5.0	7.9	4.8
Ba	183.2	36.1	534.8	543.1	663.8	359.8	490.7	668.1	590.8	588.8
La	29.3	2.8	32.0	19.7	35.3	24.9	24.7	35.5	35.0	32.2
Ce	52.1	9.0	72.5	39.6	74.9	51.4	47.9	69.0	64.9	62.1
Pr	6.4	1.2	7.8	4.7	8.7	5.8	5.3	7.7	7.3	6.9
Nd	22.3	5.0	26.1	15.4	29.9	21.8	20.9	28.8	29.3	25.9
Sm	4.1	1.2	4.9	3.1	5.8	3.2	3.3	5.0	5.6	4.7
Eu	1.1	0.2	1.1	0.7	1.3	1.1	1.0	1.3	1.5	1.2
Gd	3.5	1.0	4.0	2.3	4.8	3.4	3.1	4.8	5.2	4.2
Tb	0.5	0.1	0.5	0.3	0.6	0.5	0.4	0.6	0.6	0.6
Dy	2.8	0.5	2.9	1.2	3.6	2.2	1.8	3.4	3.4	2.8
Ho	0.5	0.0	0.6	0.2	0.7	0.5	0.4	0.6	0.6	0.5
Er	1.6	0.2	1.5	0.4	1.8	1.2	1.0	1.7	1.7	1.5
Tm	0.0	0.0	0.2	0.1	0.3	0.0	0.0	0.2	0.2	0.2
Yb	1.5	0.2	1.6	0.5	1.7	1.2	1.1	1.5	1.6	1.4
Lu	0.2	0.0	0.3	0.1	0.3	0.2	0.2	0.3	0.2	0.2
Hf	3.9	2.5	7.3	3.1	5.3	5.6	3.6	6.3	5.1	5.0
Th	10.4	9.4	18.1	9.5	13.2	9.4	2.9	11.3	7.7	13.7
U	5.1	2.3	5.8	8.5	3.2	5.1	1.4	3.3	2.3	2.6

1102

1103 Table 5

Alb	Alb	Unalt	Unalt	Unalt	Unalt	Unalt	Unalt	Unalt	Unalt
-----	-----	-------	-------	-------	-------	-------	-------	-------	-------

Pluton/Area Sample	Baqata			Boboti				Daléma			
	BAQ01	BP08	BOP1A	BOP1B	BOP2	BOP3	BOP4	CLIB08	CLIB09	CLIB10	
SiO <sub>2</sub>	72.4	65.0	60.9	61.7	74.0	74.8	60.0	51.8	49.9	52.1	
TiO <sub>2</sub>	0.1	0.5	0.8	0.8	0.1	0.1	1.0	2.2	1.2	1.1	
Al <sub>2</sub> O <sub>3</sub>	16.4	17.5	14.4	14.4	14.2	13.9	15.2	14.3	15.0	14.8	
Fe <sub>2</sub> O <sub>3</sub> T	0.3	0.9	6.2	6.2	0.8	0.6	8.4	14.6	12.0	9.8	
MnO	0.0	0.0	0.1	0.1	0.0	0.0	0.1	0.2	0.1	0.1	
MgO	0.3	1.5	3.7	3.7	0.2	0.1	3.7	4.1	6.9	7.5	
CaO	0.3	3.0	4.1	4.1	0.7	0.6	5.4	8.0	8.3	7.9	
Na <sub>2</sub> O	8.7	9.8	3.8	3.7	4.1	4.0	3.6	3.1	2.8	3.4	
K <sub>2</sub> O	0.5	0.5	3.8	3.9	4.8	5.1	2.9	1.6	1.6	1.7	
P <sub>2</sub> O <sub>5</sub>	0.0	0.2	0.2	0.2	0.1	0.0	0.2	0.4	0.4	0.3	
LOI	0.5	0.8	0.6	0.5	0.4	0.4	0.3	0.0	1.0	1.1	
Total	99.4	99.7	98.5	99.4	99.4	99.5	100.8	100.3	99.3	99.5	

Sample	BAQ01	BP08	BOP1A	BOP1B	BOP2	BOP3	BOP4	CLIB08	CLIB09	CLIB10
V	0.1	28.3	104.8	106.8	0.8	2.8	139.5	241.5	245.1	224.0
Cr	10.1	39.1	206.6	206.2	20.2	11.7	120.9	37.1	224.2	321.1
Co	0.0	0.0	15.6	15.4	0.0	0.0	20.7	37.4	27.9	30.8
Ni	4.1	6.1	74.4	71.8	4.1	4.1	66.3	7.2	40.2	93.1
Ga	13.3	18.5	21.5	21.2	23.8	21.0	20.5	22.1	23.0	21.8
Rb	5.6	9.2	224.4	231.4	304.4	232.2	150.5	51.2	47.0	61.1
Sr	137.3	114.5	317.8	320.2	95.9	107.2	339.9	440.4	495.5	498.7
Y	3.2	16.5	20.2	20.3	5.3	9.5	19.9	33.1	33.8	29.1
Zr	41.3	176.7	241.2	213.8	59.6	53.6	151.8	169.2	99.4	153.0
Nb	0.3	7.5	13.4	13.2	5.6	3.9	9.4	14.9	6.4	4.9
Ta	0.0	0.7	1.3	1.4	1.2	1.2	0.9	0.7	0.0	0.2
Mo	0.0	0.7	3.4	3.7	1.2	0.0	2.3	0.7	0.0	0.0
Cs	0.0	0.1	12.1	13.2	18.4	9.1	8.3	2.0	4.1	32.3
Ba	128.9	258.2	696.8	727.4	301.8	426.0	527.5	636.6	462.6	461.1
La	2.6	30.8	45.7	40.9	16.2	27.0	35.8	27.4	19.6	18.1
Ce	3.3	68.9	103.1	94.1	35.9	54.7	74.9	65.7	53.6	51.9
Pr	0.6	8.2	11.3	10.4	3.8	6.1	8.8	8.3	7.8	7.5
Nd	1.9	28.7	38.8	35.9	12.3	18.7	31.1	32.8	34.0	32.1
Sm	0.4	5.0	6.7	6.6	2.7	3.4	6.0	7.1	7.7	7.6
Eu	0.1	1.3	1.4	1.5	0.4	0.6	1.5	2.3	2.0	1.9
Gd	0.5	3.8	5.4	5.2	1.7	2.6	5.0	6.8	7.1	6.3
Tb	0.0	0.5	0.7	0.7	0.2	0.3	0.7	1.0	1.0	0.9
Dy	0.4	2.8	3.5	3.6	0.8	1.6	3.7	5.7	5.7	5.0
Ho	0.0	0.5	0.7	0.7	0.1	0.2	0.7	1.2	1.2	1.0
Er	0.2	1.4	1.7	1.8	0.4	0.7	1.8	2.9	3.1	2.6
Tm	0.0	0.2	0.3	0.3	0.1	0.1	0.3	0.4	0.5	0.4
Yb	0.1	1.4	1.5	1.6	0.3	0.7	1.6	2.7	2.9	2.6
Lu	0.0	0.2	0.3	0.3	0.0	0.1	0.3	0.4	0.5	0.4
Hf	1.4	4.8	6.7	5.9	2.7	1.9	4.7	4.8	3.2	4.1
Th	0.4	5.6	15.7	15.0	8.2	12.7	14.2	3.7	1.4	1.9
U	0.5	2.3	4.4	4.7	4.1	6.0	4.3	1.2	0.7	0.7

1104

1105 Table 6

Pluton/Area Sample	Unalt	Alb	Alb	Alb	Unalt	Unalt	Unalt	Unalt	Unalt	Alb
	Fadougou FDGI01	BP31	Falémé Volcanics BP29	BO8	BP32	Gamaye MAD01	MOU02	LD23	Gara LD9	Kolya BO1
SiO <sub>2</sub>	71.2	59.8	57.4	63.5	54.8	72.1	70.9	53.1	48.0	74.9
TiO <sub>2</sub>	0.2	0.7	0.7	0.5	0.8	0.3	0.0	0.8	0.5	0.1
Al <sub>2</sub> O <sub>3</sub>	14.9	14.8	13.3	15.4	13.0	15.2	16.9	18.1	8.9	14.2
Fe <sub>2</sub> O <sub>3</sub> T	2.4	3.8	5.4	1.5	11.7	1.5	0.1	9.2	8.8	0.2
MnO	0.0	0.0	0.0	0.0	0.0	0.0	0.0	0.0	0.1	0.0

52

MgO	0.5	6.7	7.7	3.0	8.5	0.5	0.0	6.7	12.5	0.0
CaO	1.6	3.7	5.5	6.1	1.1	0.8	0.3	1.1	6.4	0.1
Na2O	4.0	7.4	6.2	8.9	3.2	4.7	4.6	3.8	0.1	8.0
K2O	4.4	0.3	1.2	0.1	4.4	4.2	4.3	2.1	1.4	0.1
P2O5	0.0	0.3	0.3	0.1	0.3	0.3	1.2	0.3	0.2	0.0
LOI	0.5	1.3	1.1	0.7	1.6	0.4	0.9	4.5	12.6	0.5
Total	99.7	98.7	98.7	99.9	99.3	100.0	99.1	99.8	99.4	98.1

Sample	FDGI01	BP31	BP29	BO8	BP32	MAD01	MOU02	LD23	LD9	BO1
V	13.5	125.5	132.4	88.0	137.7	15.4	31.8	141.2	136.8	3.3
Cr	22.8	331.0	475.0	124.9	438.6	28.9	16.0	224.9	214.8	15.4
Co	0.0	3.5	23.0	0.0	16.7	0.0	214.6	17.6	16.8	0.0
Ni	5.7	119.7	213.3	35.2	328.9	4.1	110.2	14.6	10.3	4.1
Ga	20.8	19.4	19.7	20.1	23.2	26.3	25.4	28.2	28.0	20.4
Rb	188.2	0.9	42.4	0.0	264.8	641.1	269.2	54.3	55.4	0.0
Sr	222.7	155.6	216.1	162.8	103.4	232.1	236.3	451.8	455.1	26.6
Y	10.3	18.2	15.6	13.8	14.7	4.7	8.0	10.2	10.3	15.2
Zr	141.1	167.7	148.5	131.6	131.7	200.4	176.6	136.8	139.3	59.7
Nb	9.6	6.8	5.9	6.0	3.5	13.3	13.2	8.8	11.5	4.9
Ta	0.9	0.4	0.8	0.7	0.2	2.2	1.7	0.6	0.7	1.1
Mo	1.1	0.0	24.9	0.6	0.6	0.0	1.2	2.4	4.7	0.0
Cs	3.0	0.0	1.2	0.0	4.7	484.5	70.3	1.7	1.9	0.0
Ba	622.4	59.8	88.7	38.0	260.4	825.2	745.7	566.3	594.7	23.6
La	30.6	18.0	50.7	12.8	8.8	63.4	49.2	12.1	11.6	19.7
Ce	66.6	46.1	108.8	40.5	22.0	123.5	110.4	25.4	26.1	44.1
Pr	7.6	6.3	11.9	5.3	2.7	12.4	10.2	3.2	3.3	5.3
Nd	26.1	26.5	41.6	20.5	10.4	37.4	30.8	12.6	12.4	19.5
Sm	4.7	5.8	7.2	4.2	2.5	5.1	4.7	2.8	2.9	4.2
Eu	0.9	1.5	2.2	1.2	0.9	0.7	0.9	0.7	0.7	0.5
Gd	3.2	4.7	5.3	3.3	2.5	3.0	3.2	2.5	2.6	3.4
Tb	0.4	0.6	0.6	0.5	0.4	0.2	0.3	0.4	0.4	0.4
Dy	1.8	3.2	3.0	2.5	2.4	1.0	1.5	2.1	1.8	2.5
Ho	0.3	0.6	0.5	0.4	0.5	0.1	0.2	0.4	0.4	0.5
Er	0.8	1.6	1.3	1.2	1.3	0.3	0.6	1.2	1.2	1.3
Tm	0.1	0.2	0.2	0.2	0.2	0.0	0.1	0.0	0.0	0.2
Yb	0.8	1.5	1.2	1.2	1.3	0.3	0.6	1.4	1.5	1.3
Lu	0.1	0.2	0.2	0.2	0.2	0.0	0.1	0.2	0.2	0.2
Hf	4.5	4.6	4.1	3.6	3.9	5.5	5.1	3.7	3.9	2.3
Th	9.3	5.5	5.2	3.8	4.4	35.4	23.6	4.6	4.8	10.1
U	4.1	1.9	1.5	1.8	1.7	6.3	5.4	1.8	1.7	3.6

1106

1107 Table 7

Pluton/Area Sample	Alb	Alb	Alb	Alb	Alb	Unalt	Unalt	Unalt	Alb	Unalt
	BO4	Kabe West BO5	BP21	Karekeane R21	R25	North Gara R42	R43	South Falémé FDGI02	Yalea UYP1	Yatea PTG1
SiO2	52.4	53.9	59.3	61.1	58.8	76.2	74.3	65.1	60.0	69.5
TiO2	1.0	0.8	0.6	0.5	0.6	0.0	0.0	0.5	0.7	0.3
Al2O3	15.4	16.4	15.5	15.5	16.2	13.7	13.8	14.7	14.6	15.4
Fe2O3T	5.4	8.8	2.9	3.0	3.4	0.4	0.5	4.2	4.6	1.9
MnO	0.0	0.0	0.0	0.0	0.0	0.0	0.0	0.0	0.0	0.0
MgO	4.1	4.6	2.8	2.6	3.2	0.1	0.1	3.5	3.1	0.8
CaO	5.7	4.6	5.9	5.3	6.2	0.3	0.4	2.7	2.7	1.5
Na2O	5.2	6.1	8.5	8.8	7.8	3.5	4.2	4.3	7.5	5.2
K2O	2.0	1.3	0.1	0.1	0.6	5.4	4.9	3.4	0.7	3.1
P2O5	0.1	0.1	0.2	0.1	0.3	0.0	0.0	0.2	0.2	0.1
LOI	8.6	2.7	3.6	3.2	3.6	0.8	0.7	0.7	4.8	0.9
Total	100.0	99.4	99.5	100.3	100.7	100.3	98.9	99.3	99.0	98.7

53

Sample	BO4	BO5	BP21	R21	R25	R42	R43	FDGI02	UYP1	PTG1
V	196.4	168.4	94.3	59.3	84.5	1.9	2.7	68.7	96.9	25.9
Cr	18.0	74.3	48.0	39.4	59.5	11.3	15.8	198.2	123.1	18.8
Co	0.0	18.8	36.7	11.7	11.9	1.8	2.0	9.1	14.3	4.2
Ni	25.7	44.5	38.1	16.7	33.1	5.4	3.7	75.3	54.3	8.0
Ga	18.1	20.3	19.8	16.6	15.9	21.6	23.7	20.5	18.4	34.4
Rb	38.1	30.0	4.7	2.0	26.3	265.8	270.8	133.4	10.1	79.1
Sr	105.8	151.7	140.0	93.4	234.0	53.4	74.6	496.9	104.0	691.5
Y	21.7	23.9	15.4	12.2	21.2	7.8	4.4	14.6	13.4	5.8
Zr	115.8	92.5	133.7	107.6	146.0	38.4	28.4	187.3	143.3	120.4
Nb	6.4	2.9	5.4	6.0	6.4	8.3	8.6	8.4	8.4	6.0
Ta	0.4	0.0	0.7	0.6	0.5	1.4	1.7	0.9	0.7	0.5
Mo	0.0	0.0	1.9	26.4	0.0	1.5	3.0	2.2	0.8	1.2
Cs	0.1	0.0	0.1	0.3	2.2	3.3	13.6	2.9	0.6	2.6
Ba	226.8	221.3	23.4	14.5	80.7	133.2	164.0	807.5	31.3	954.9
La	17.9	19.2	12.6	6.1	15.9	20.6	7.3	43.1	32.7	25.1
Ce	35.5	36.9	34.2	15.9	50.7	30.0	13.6	95.0	77.7	49.6
Pr	4.7	4.9	4.3	2.8	8.0	4.1	1.7	10.4	10.1	5.8
Nd	18.4	19.0	17.9	14.0	36.0	14.6	6.5	35.5	40.2	22.8
Sm	4.0	4.2	4.3	3.7	7.9	2.5	1.7	5.7	7.8	4.1
Eu	1.2	1.3	1.1	1.0	2.4	0.4	0.3	1.4	2.1	1.0
Gd	4.1	4.3	3.6	3.1	6.5	2.5	1.4	4.2	6.3	3.1
Tb	0.7	0.6	0.5	0.4	0.9	0.3	0.2	0.5	0.7	0.3
Dy	3.8	3.9	2.8	2.4	4.9	1.5	0.8	2.6	3.6	1.4
Ho	0.8	0.8	0.5	0.5	0.8	0.2	0.2	0.5	0.5	0.2
Er	2.0	2.1	1.3	1.3	2.2	0.6	0.4	1.2	1.2	0.6
Tm	0.3	0.3	0.2	0.2	0.3	0.0	0.0	0.2	0.0	0.0
Yb	2.0	1.9	1.2	1.2	1.9	0.5	0.4	1.3	1.0	0.5
Lu	0.3	0.3	0.2	0.2	0.2	0.1	0.1	0.2	0.2	0.1
Hf	3.5	2.4	3.8	3.2	3.6	1.8	1.8	5.3	3.6	3.1
Th	3.5	3.8	4.2	4.8	4.4	6.4	15.4	13.4	3.8	4.8
U	1.1	0.9	1.2	1.9	2.1	2.7	2.8	4.4	1.2	1.7

1108

1109











% conc4

Accepted Manuscript



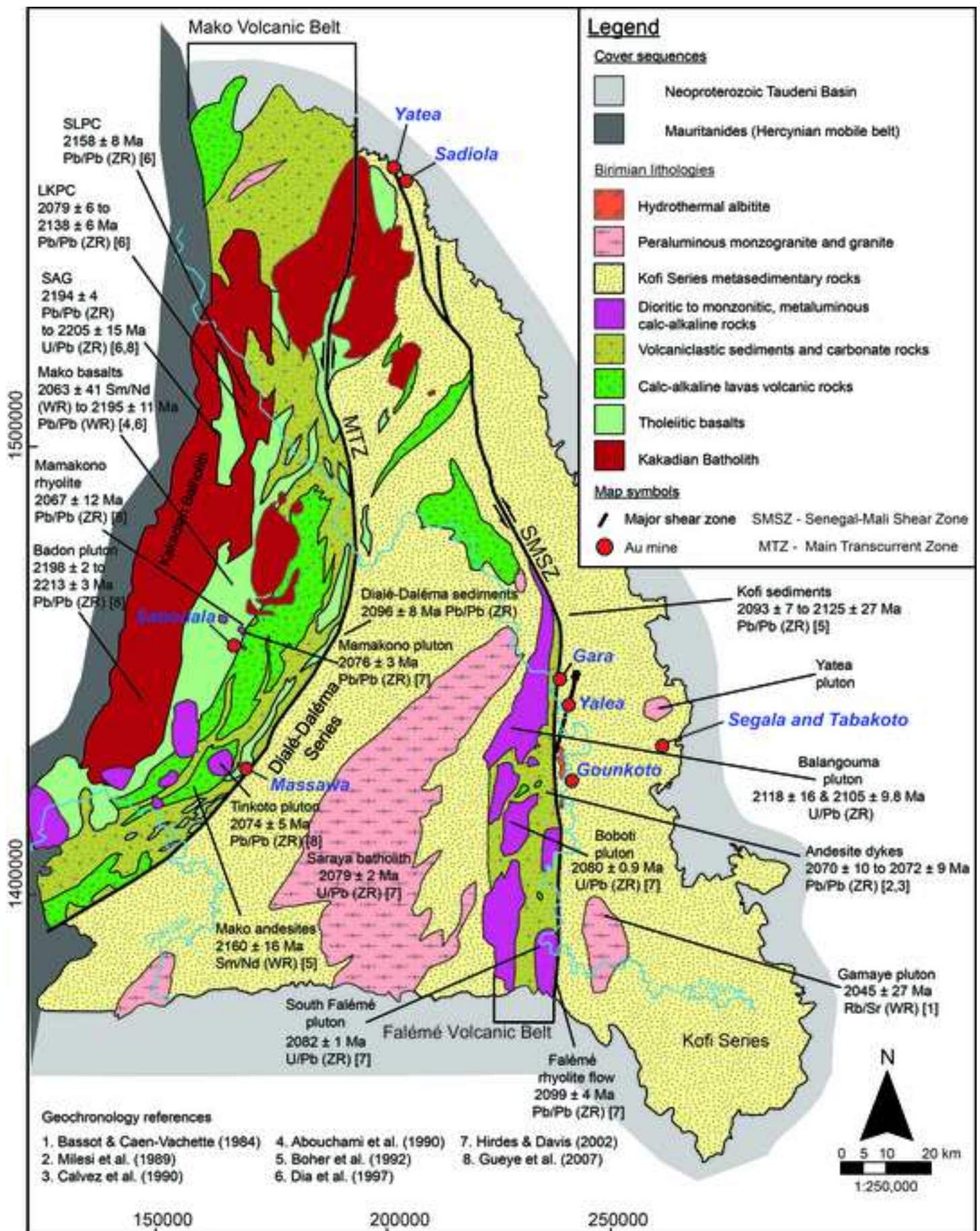
CLIB01 - 89	5.48	0.14	0.2921	0.0085	0.83642	0.1363	0.002	0.25526	0.1105	0.004	1888	23	1648	42	2117	72	2175	27	149.3	6.2	77.2	3.1	76	2.5	1.939	0.037
CLIB01 - 90	2.838	0.058	0.1514	0.0041	0.86624	0.1365	0.0016	0.57207	0.0732	0.0023	1362	16	908	23	1428	44	2178	21	470	32	185	11	121.8	7.6	2.518	0.025
CLIB01 - 91	6.23	0.18	0.3241	0.0068	0.90309	0.1389	0.002	-0.57257	0.1158	0.0066	2001	25	1808	33	2200	120	2206	25	317	12	184	7.5	177.9	3.7	1.736	0.014
CLIB01 - 92	3.77	0.35	0.1247	0.0081	0.99516	0.2179	0.0056	-0.85757	0.143	0.018	1556	60	753	44	2680	300	2950	39	832	44	377	22	508	87	2.231	0.022
CLIB01 - 93	1.084	0.023	0.06523	0.0011	0.49365	0.1205	0.0022	0.059487	0.02916	0.0011	743	11	407.3	6.8	581	21	1951	33	554	36	408	26	106.9	7.1	1.3582	0.0093
CLIB01 - 94	8.06	0.17	0.4276	0.0077	0.76996	0.1362	0.0019	-0.12656	0.1551	0.0071	2232	18	2293	35	2910	120	2172	24	112.1	2.2	59.3	1.6	83.8	4	1.909	0.028
CLIB01 - 96	4.94	0.15	0.236	0.012	0.88355	0.1575	0.0039	0.84761	0.1125	0.0042	1801	26	1358	60	2153	76	2408	42	258	35	129	17	127	16	1.961	0.025
CLIB01 - 97	4.15	0.055	0.2316	0.0042	0.7372	0.1301	0.0012	0.26639	0.0806	0.0025	1662	11	1342	22	1566	46	2098	16	461	19	219.5	8.8	158.2	5.4	2.099	0.014
CLIB01 - 98	9.5	0.15	0.4258	0.0071	0.72164	0.1614	0.0017	-0.05288	0.2489	0.0098	2384	15	2286	32	4480	160	2469	18	203.1	9	84.9	3.8	191.6	9.6	2.395	0.017
CLIB01 - 99	7.24	0.1	0.4075	0.0064	0.45324	0.1292	0.0017	0.23774	0.1191	0.004	2140	13	2202	29	2274	72	2080	24	106.5	3.3	46.7	1.5	50.4	1.4	2.285	0.021
CLIB01 - 10	7.16	0.11	0.4013	0.0067	0.46324	0.1291	0.0019	0.27676	0.1217	0.0042	2128	14	2176	31	2326	76	2081	26	73.7	2.6	56	2.1	61.4	1.7	1.321	0.015
CLIB01 - 10	4.26	0.14	0.1454	0.0052	0.89535	0.2137	0.0029	0.28923	0.2077	0.01	1673	28	873	29	3800	170	2930	22	304	26	106	10	179.2	8.9	2.942	0.036
CLIB01 - 10	6.42	0.12	0.3586	0.007	0.68951	0.1297	0.0017	0.12268	0.1129	0.0044	2030	17	1974	33	2160	79	2089	24	117	5.8	43.5	2.2	44.1	1.5	2.694	0.03
CLIB01 - 10	3.276	0.073	0.0917	0.0025	0.18455	0.2669	0.0091	0.74821	0.1082	0.0046	1473	17	565	15	2073	84	3250	55	877	34	525	21	511.3	9.2	1.668	0.014
CLIB01 - 10	5.77	0.15	0.2842	0.0085	0.93156	0.1474	0.0014	0.18669	0.1057	0.0042	1939	22	1609	43	2029	77	2313	17	371	24	229	17	221	12	1.672	0.016
CLIB01 - 10	6.761	0.067	0.3744	0.0056	0.39451	0.1309	0.0012	0.3773	0.1172	0.0041	2079.3	8.8	2050	26	2238	74	2107	16	250.5	5.4	98.6	2.7	108.7	1.9	2.543	0.026

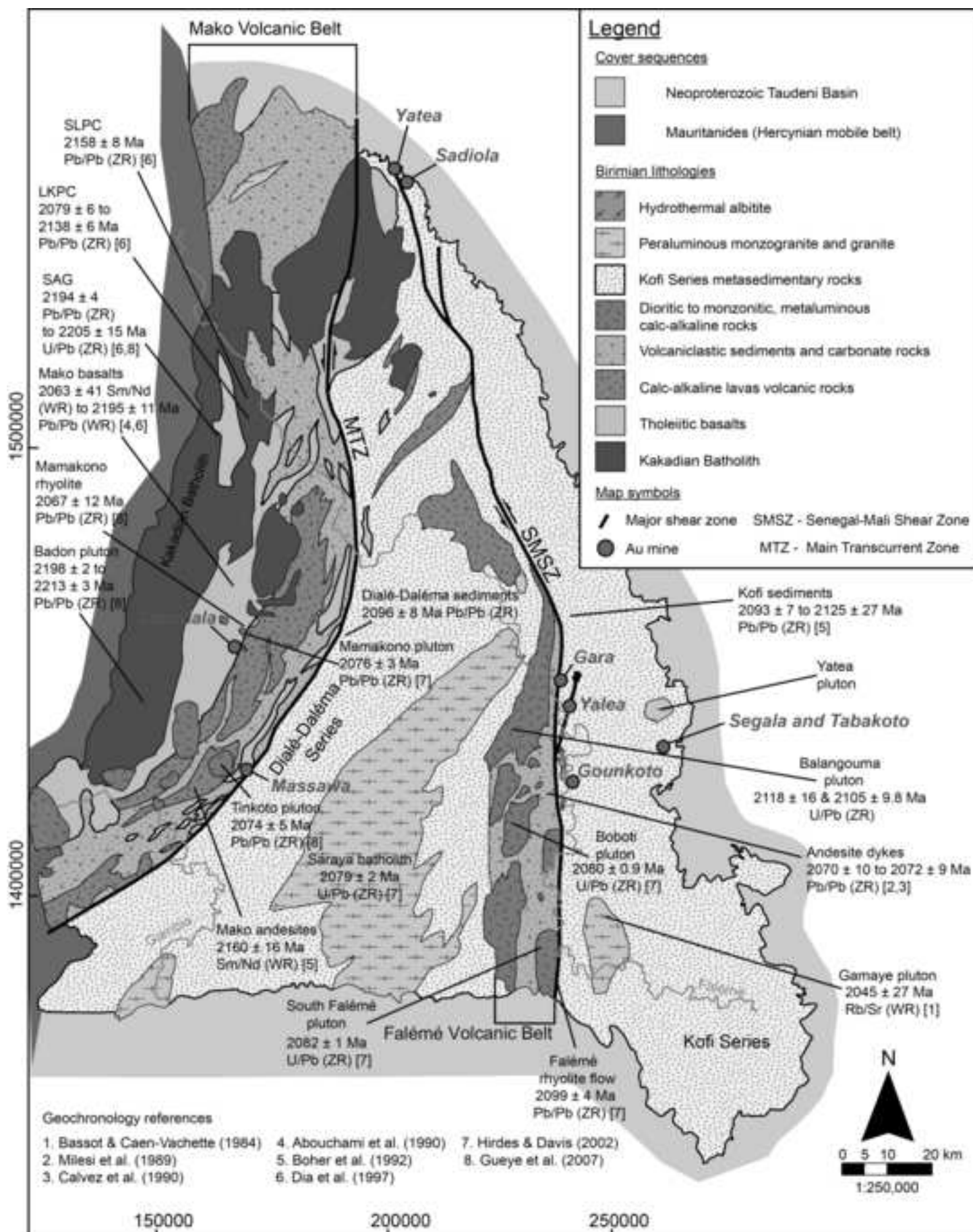
Accepted Manuscript

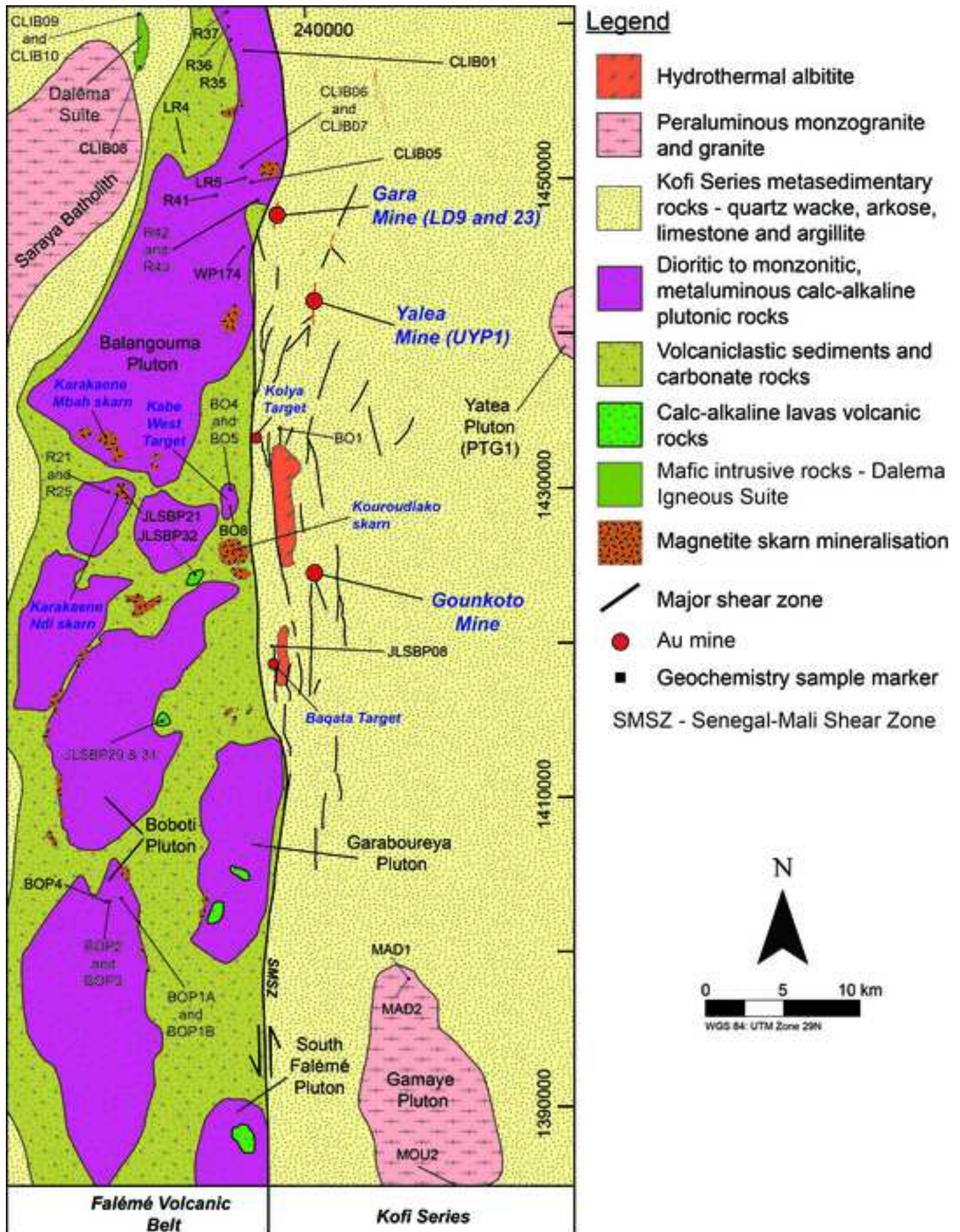


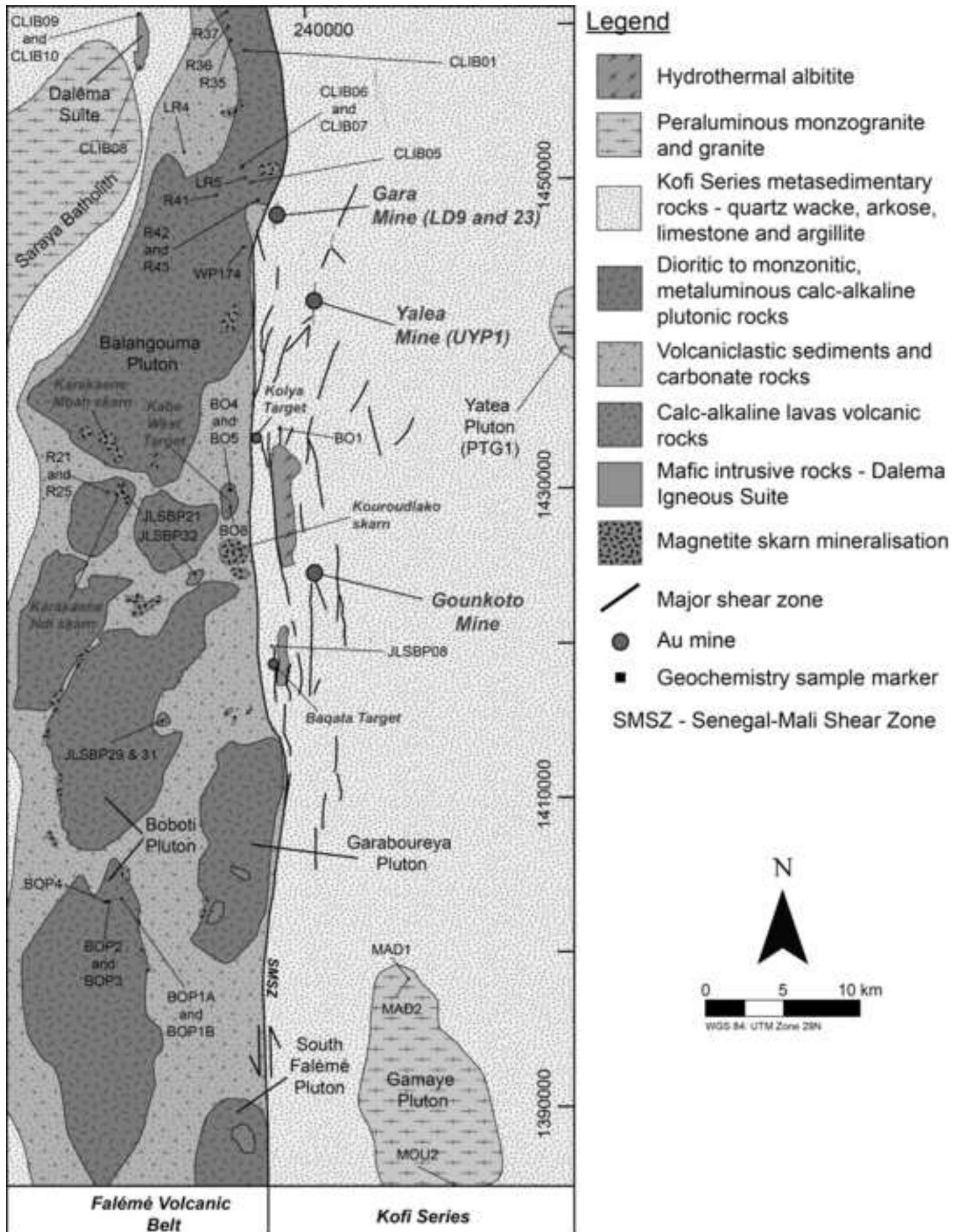


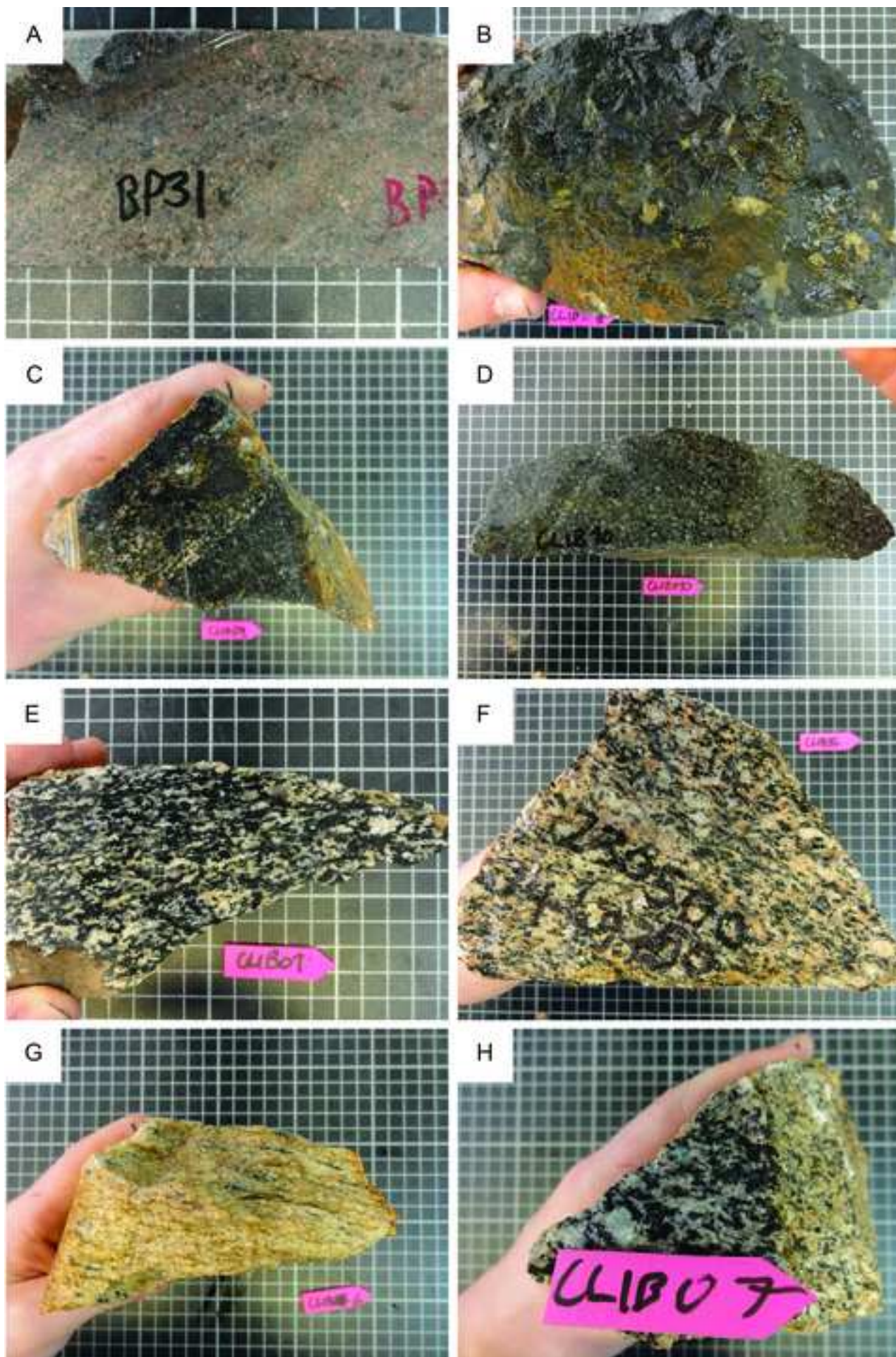


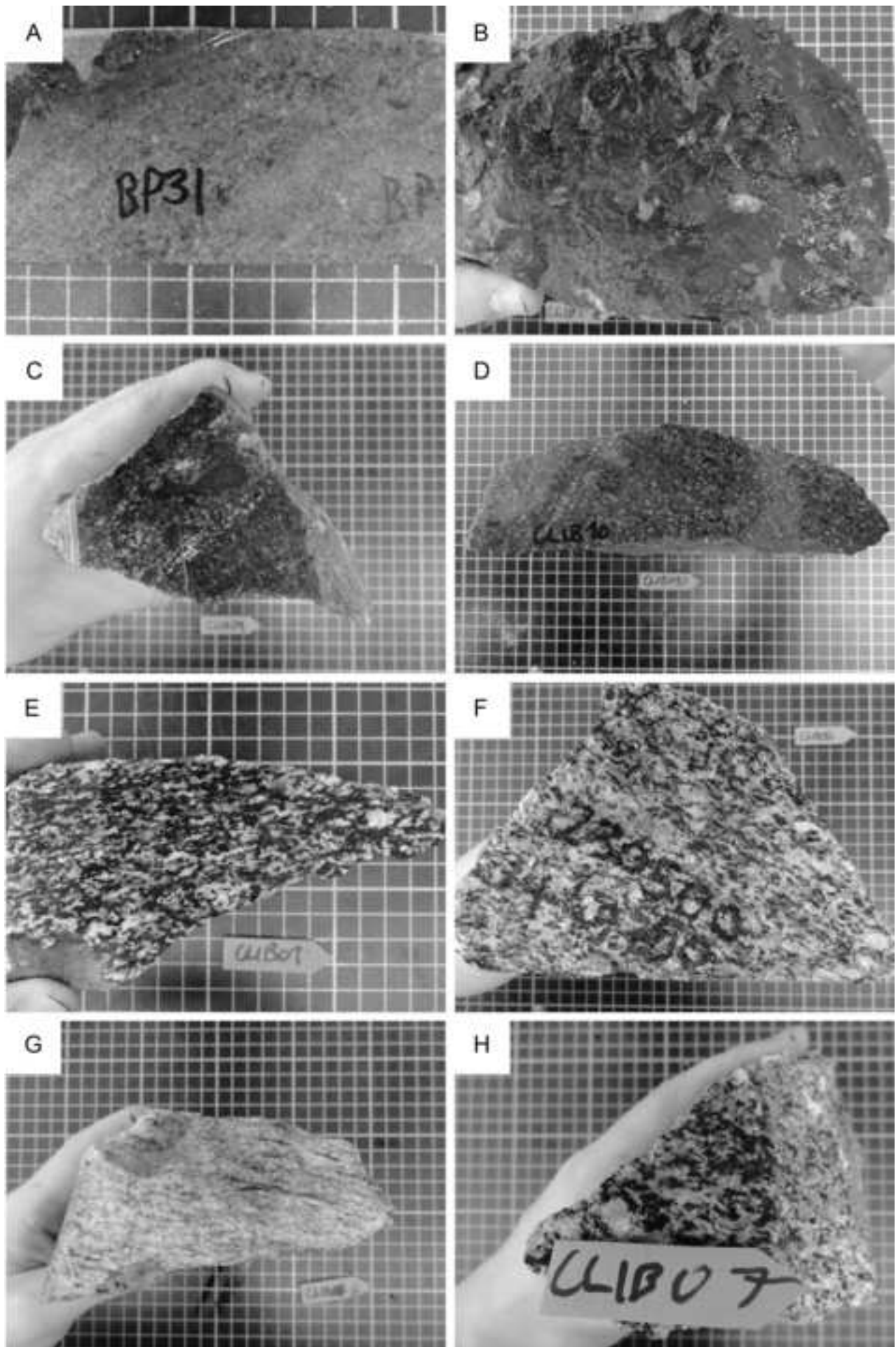


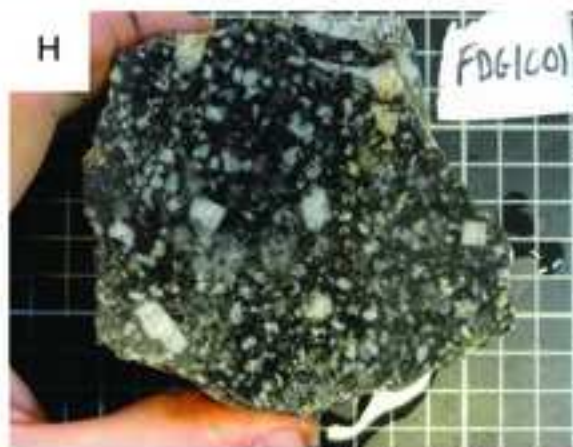
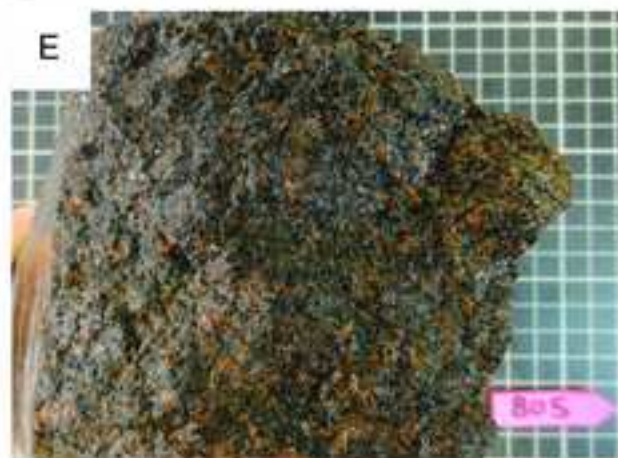
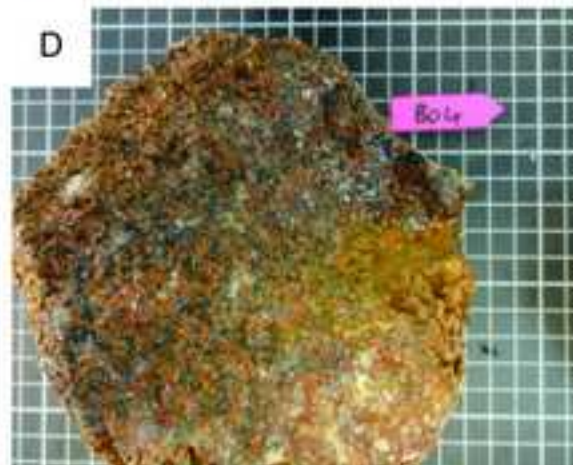
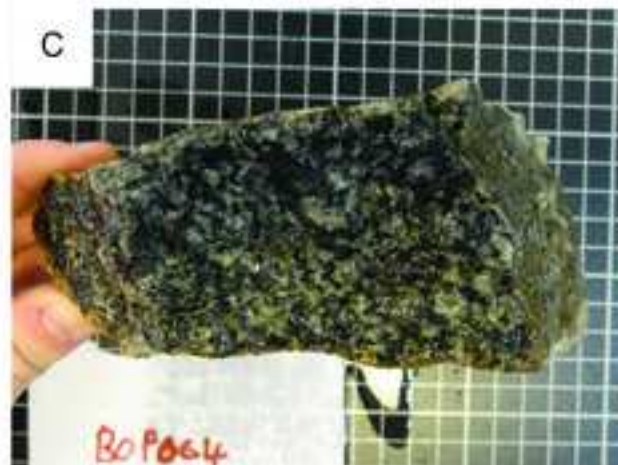
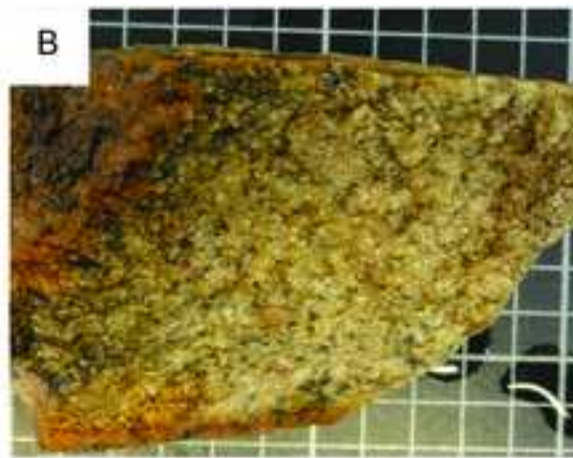


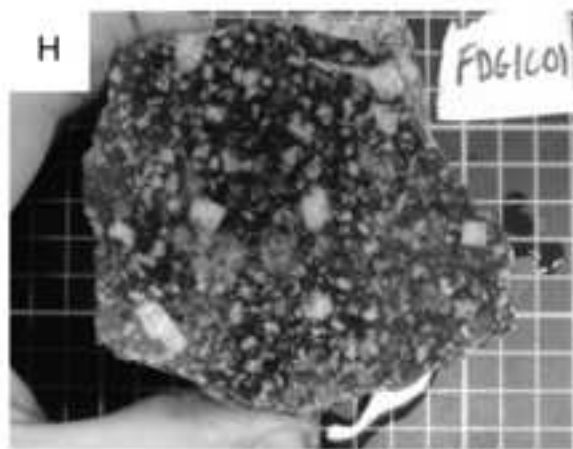
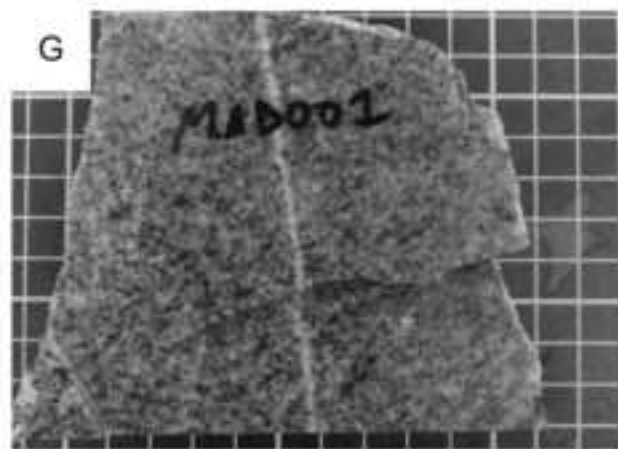
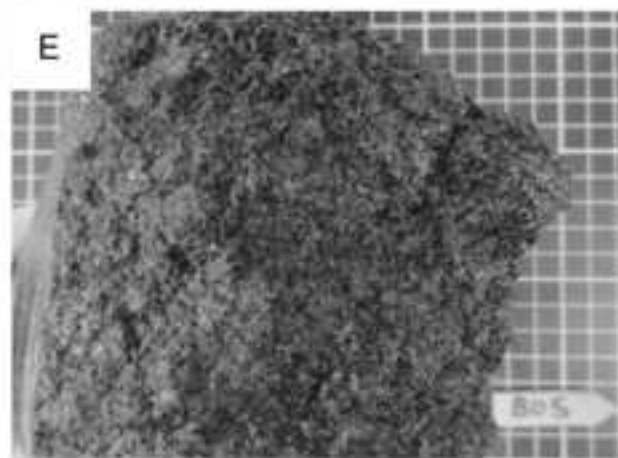
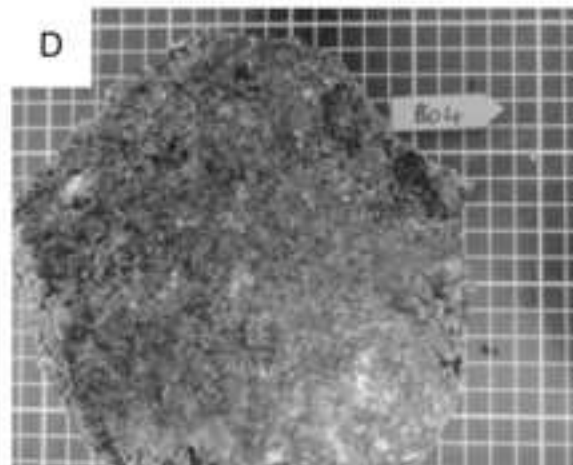
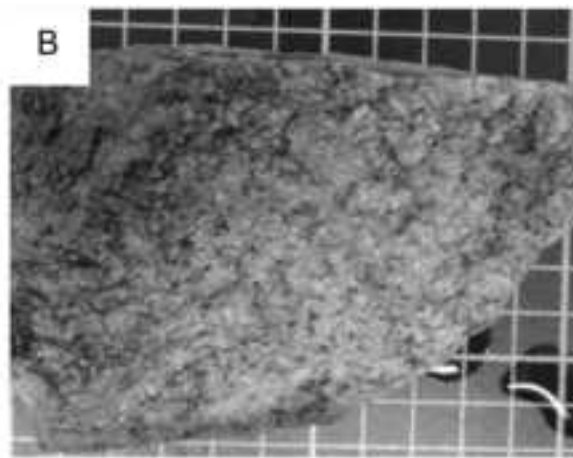
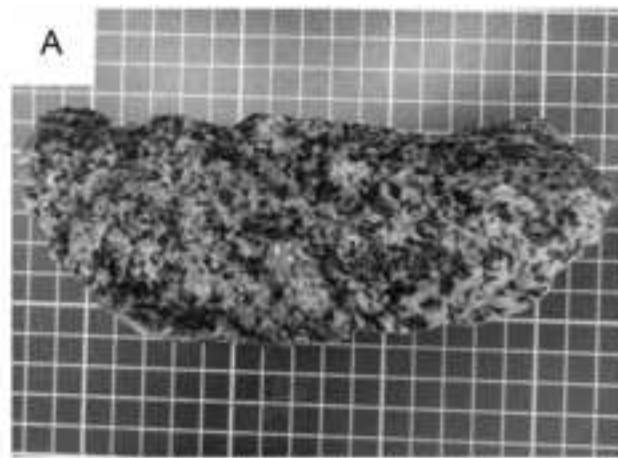




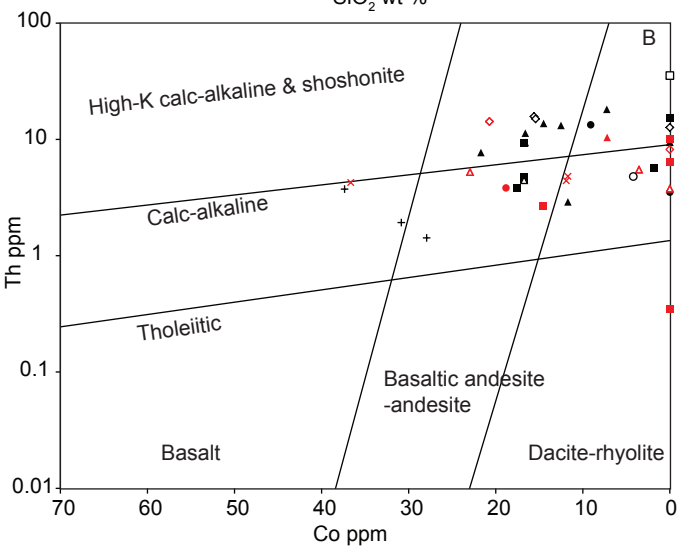
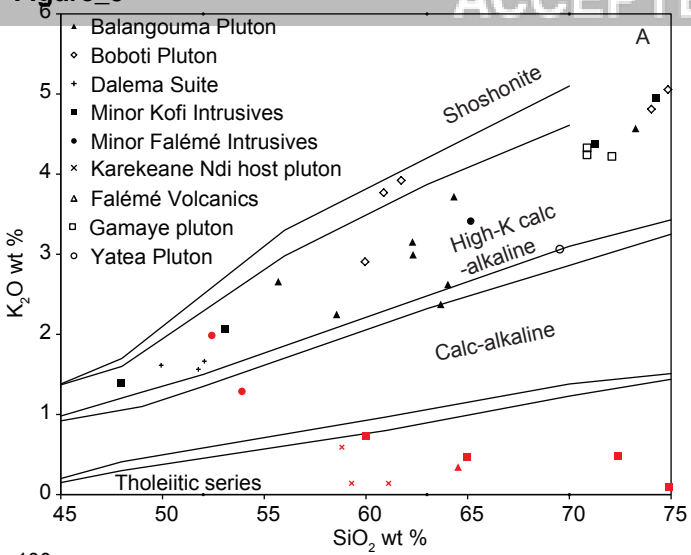


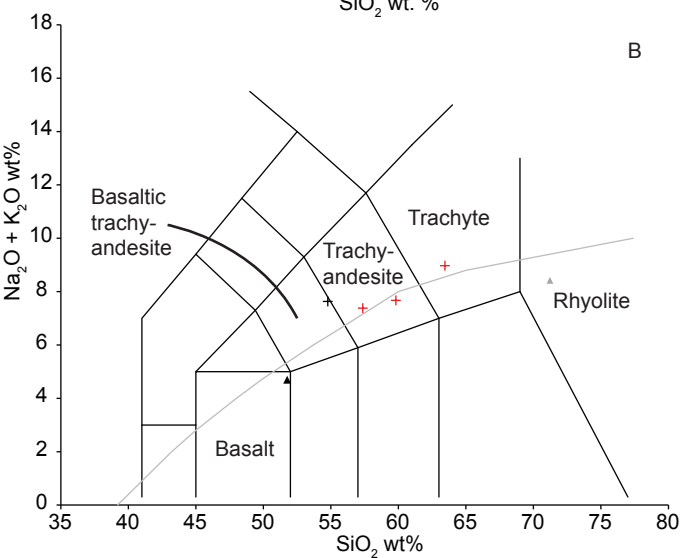
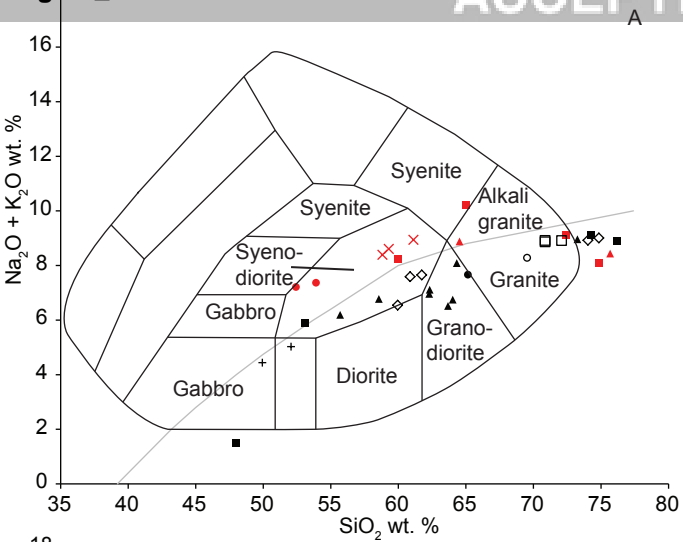












Legend

*Plutonic rocks*

▲ Balangouma

◇ Boboti

+ Dalema Suite

■ Minor Kofi Intrusives

● Minor Falémé Intrusives

□ Gamaye pluton

— Alkali-Sub-alkali division

× Karekeane Ndi host pluton

○ Yatea

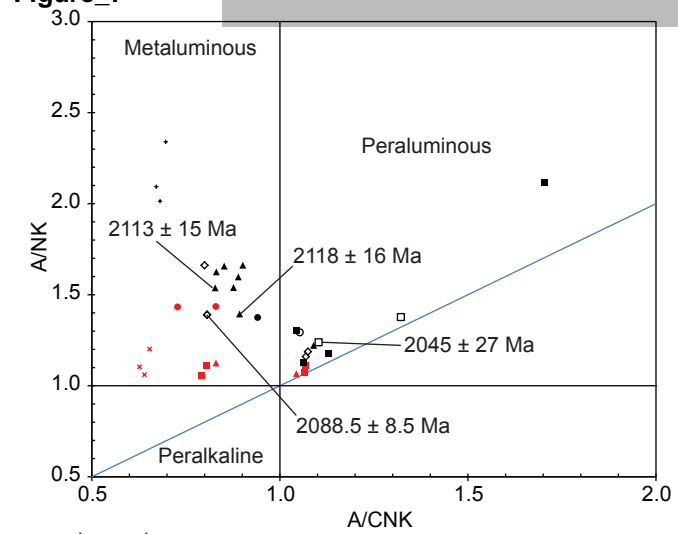
*Volcanic rocks*

▲ Dalema Suite

▲ Fadougou rhyolite

+ Falémé Volcanics

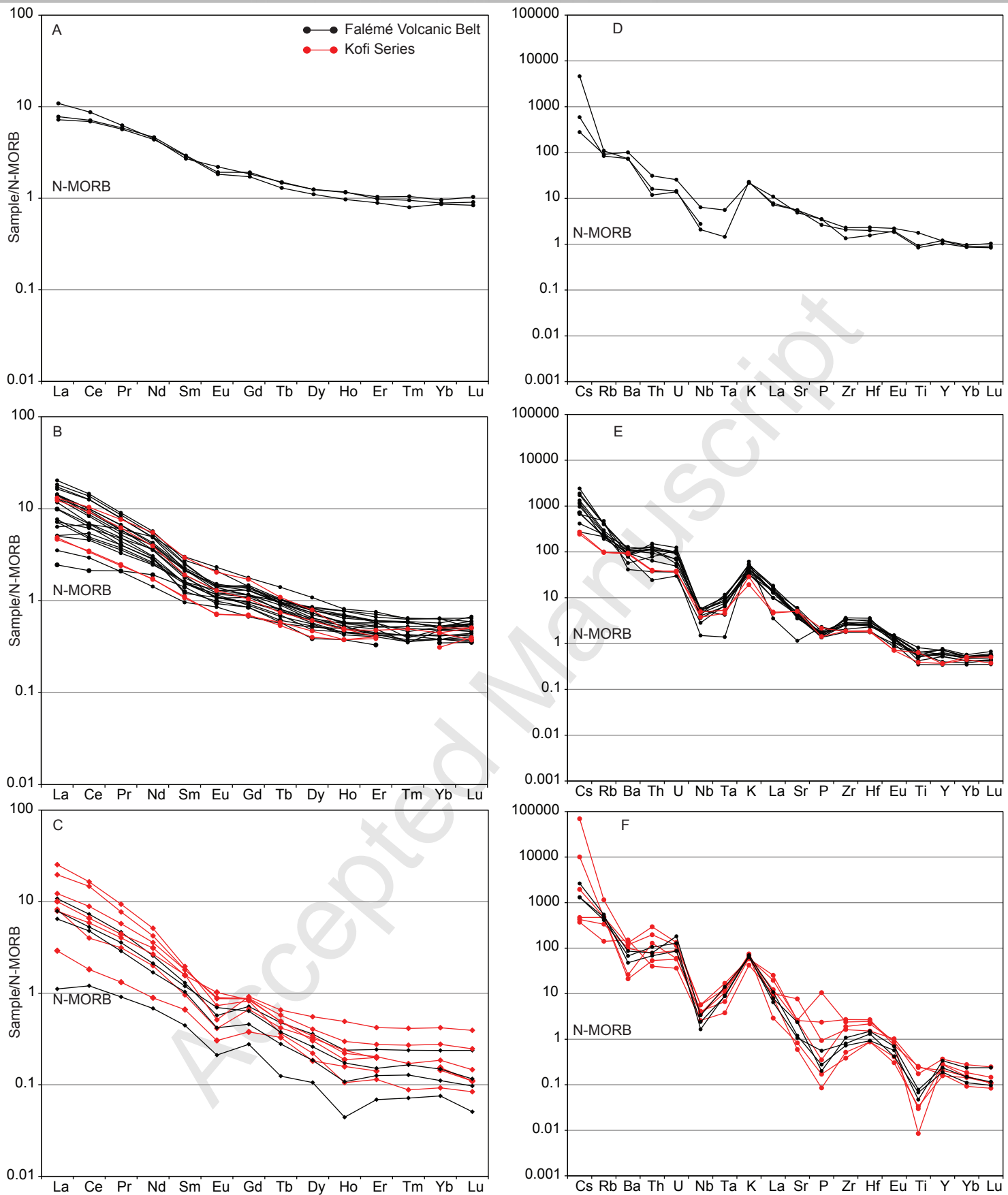
Figure\_7

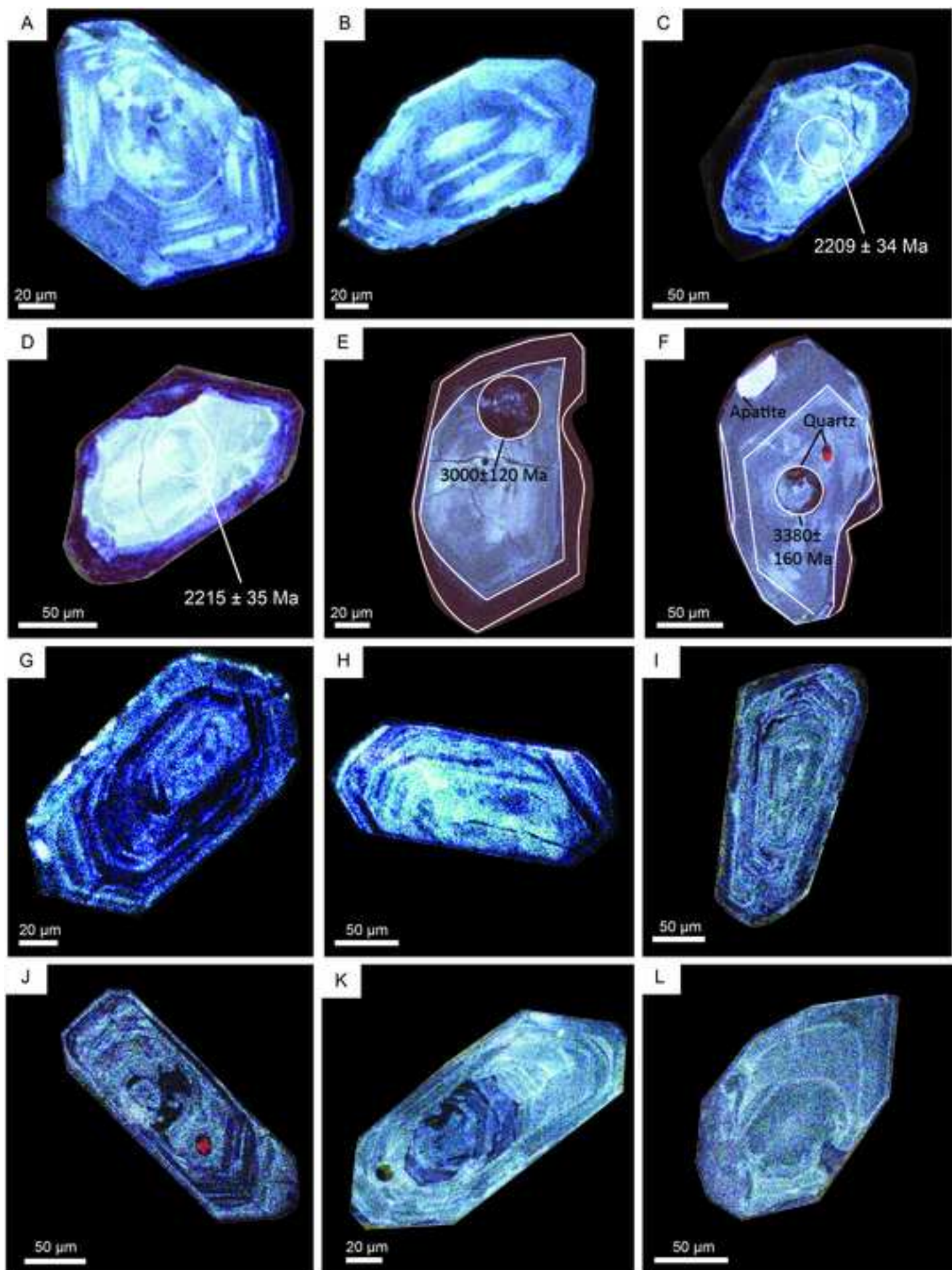


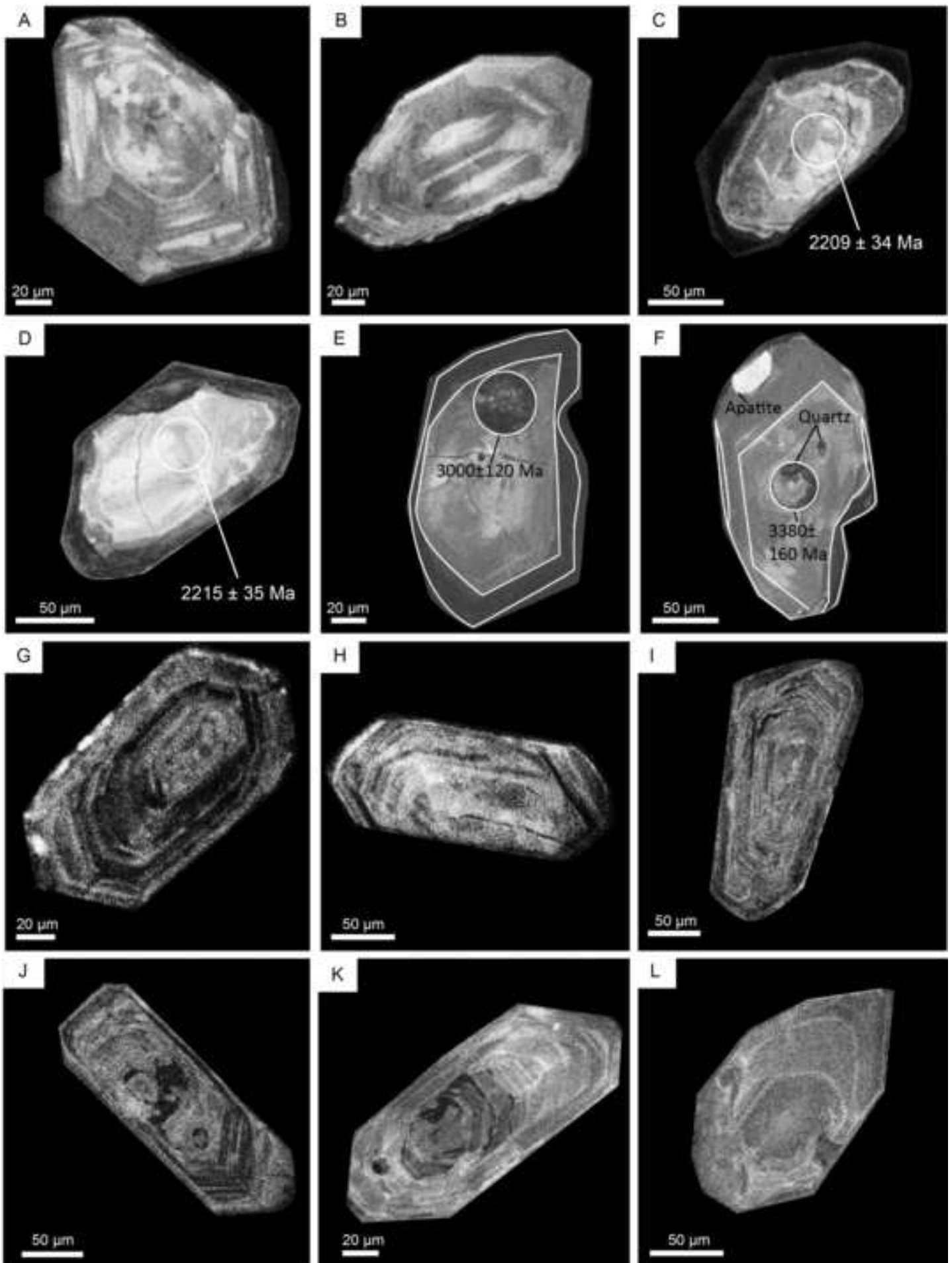
## Legend

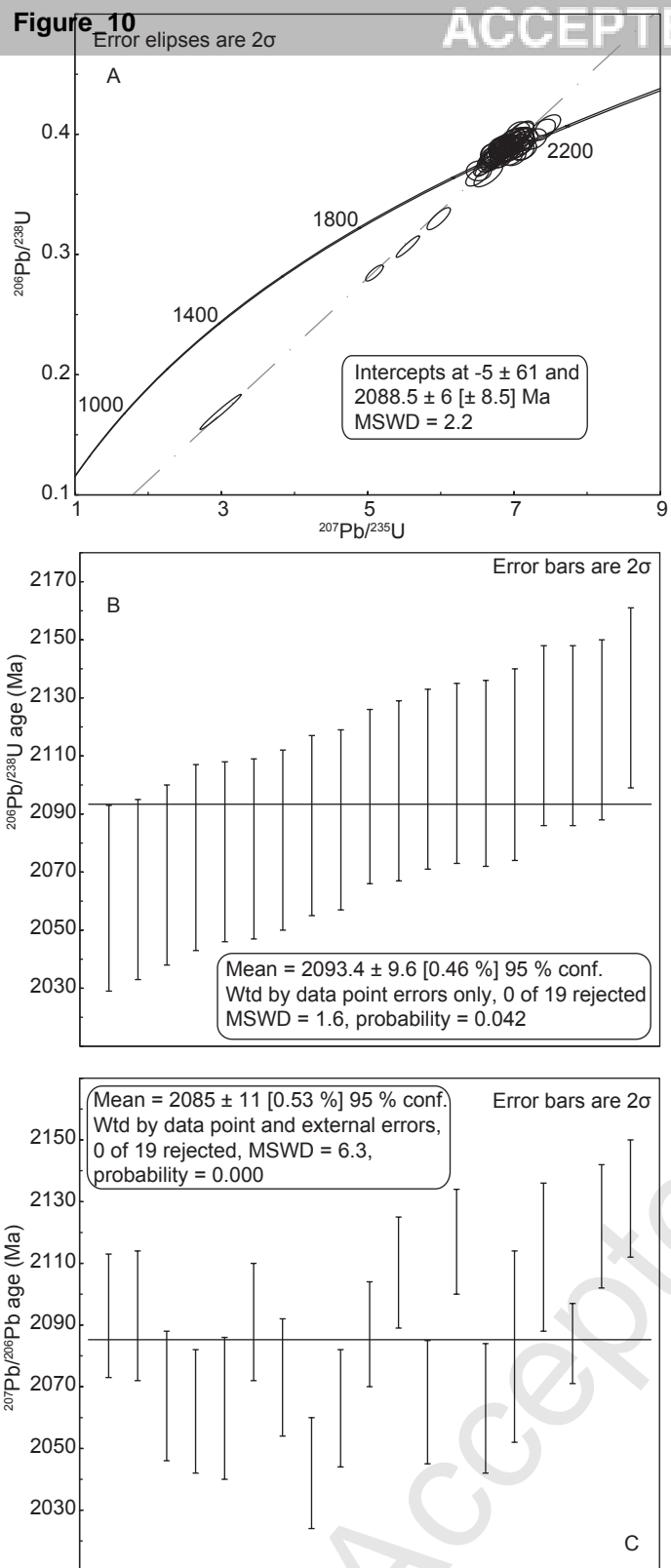
- ▲ Balangouma Pluton    ● Minor Falémé Intrusives
- ◇ Boboti Pluton        □ Gamaye pluton
- + Dalema Suite        × Karekeane Ndi host pluton
- Minor Kofi Intrusives    ○ Yatea Pluton

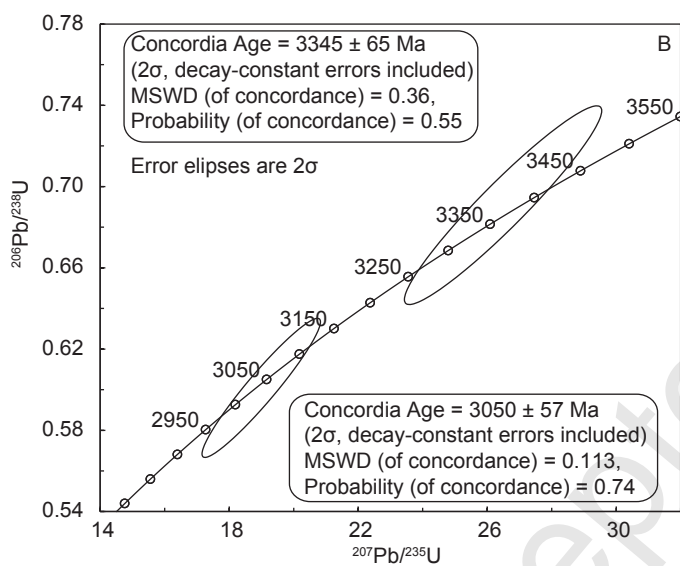
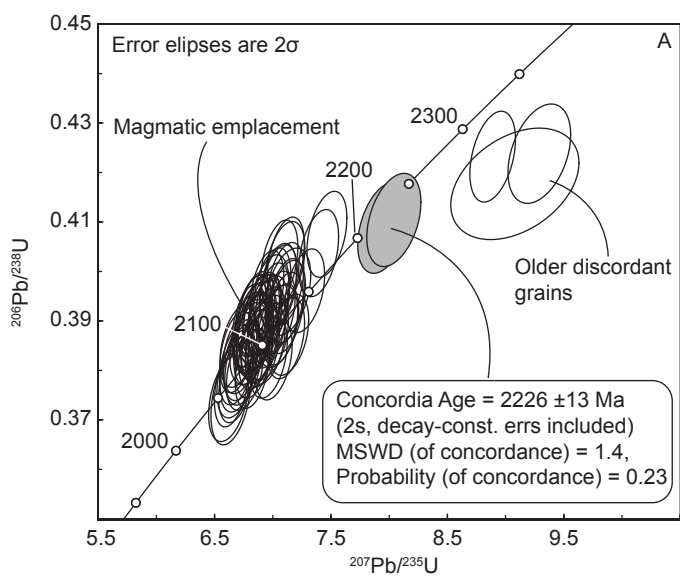
ACCEPTED MANUSCRIPT



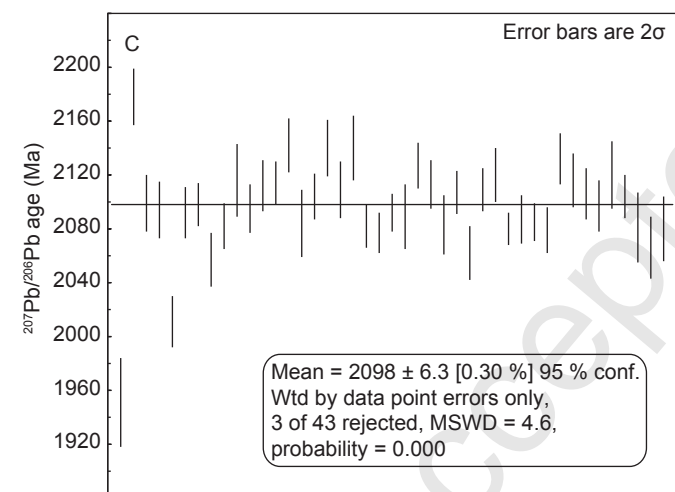
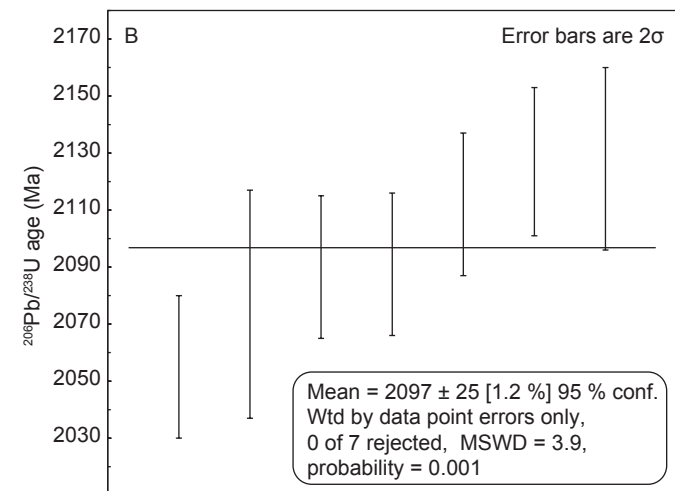
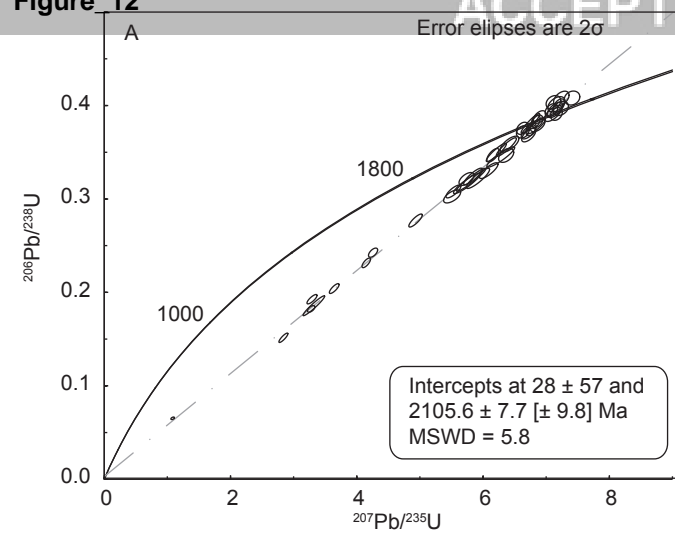


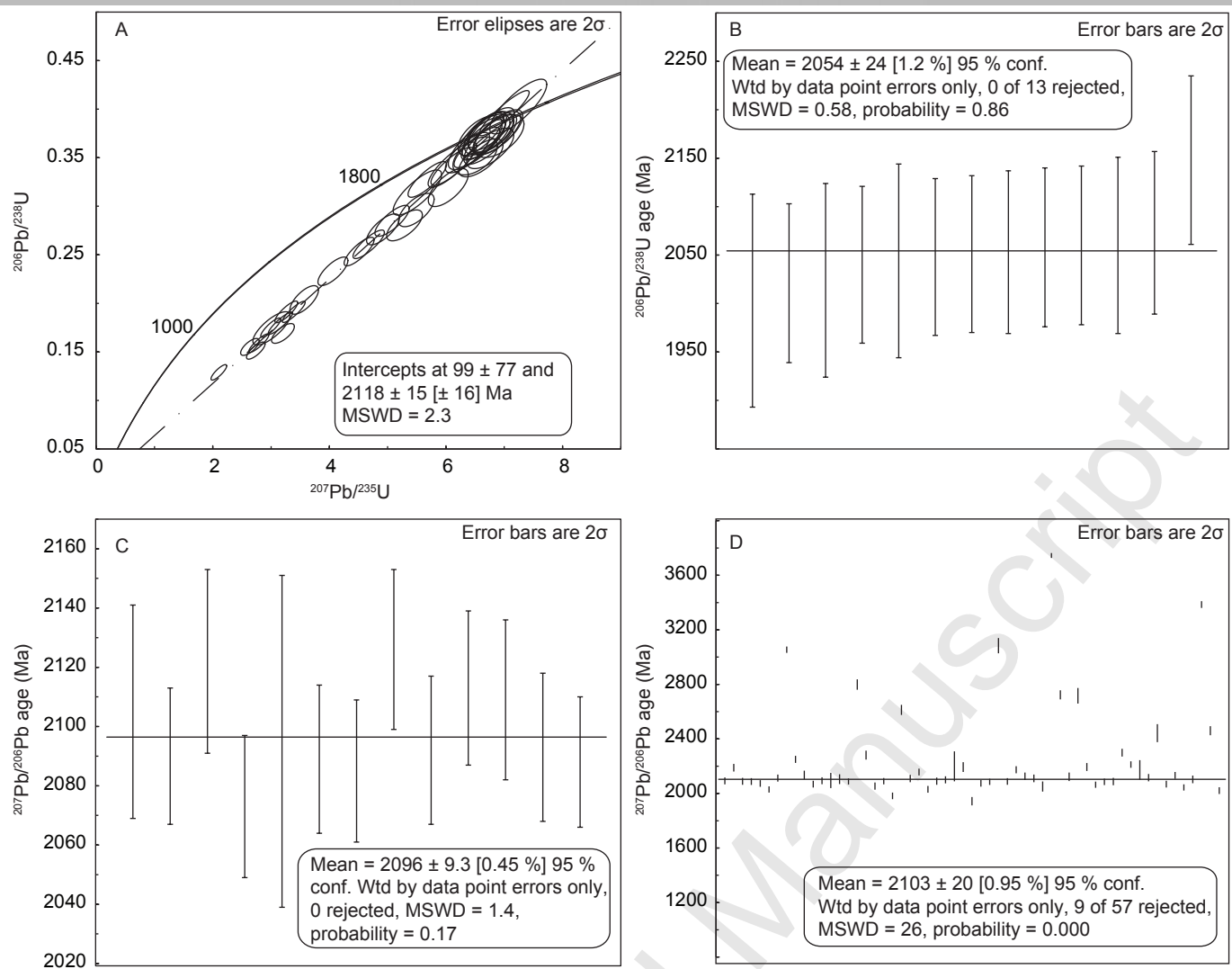


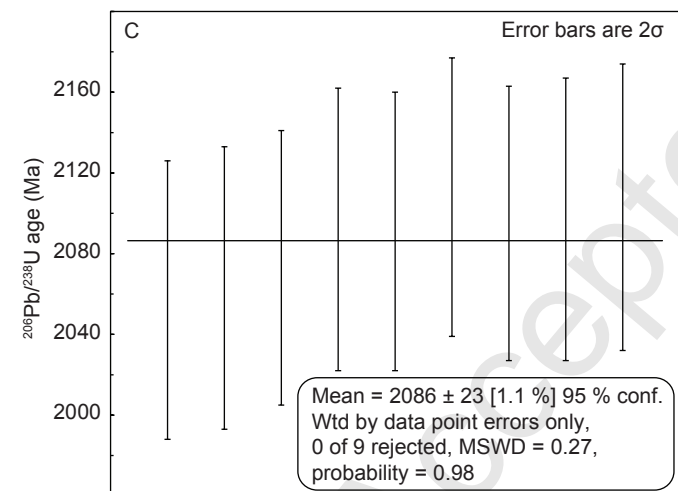
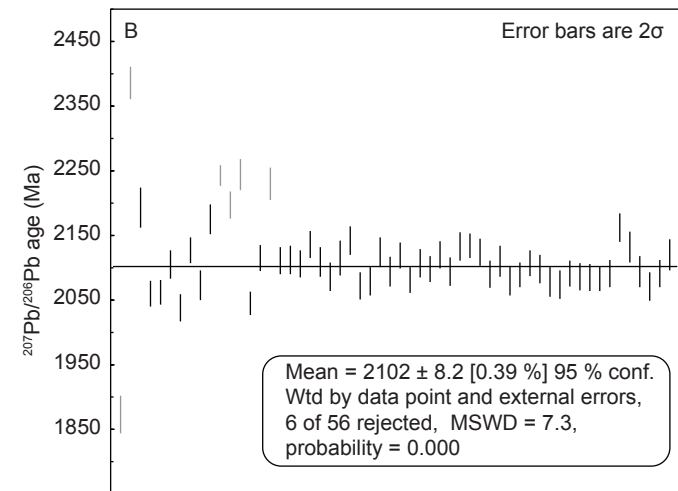
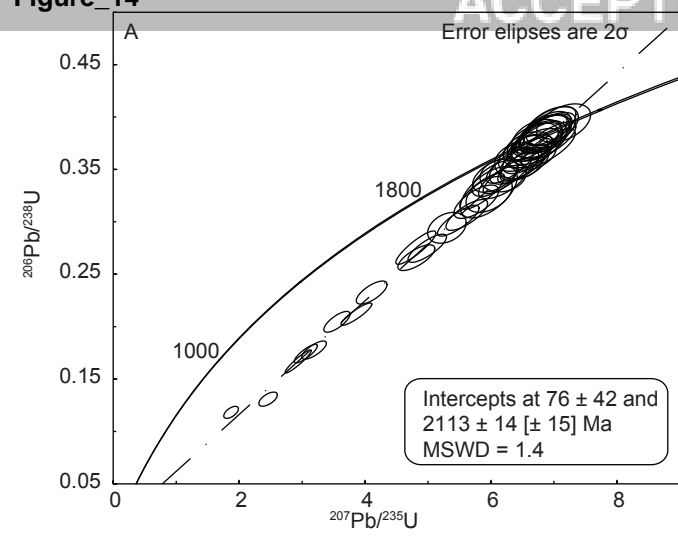


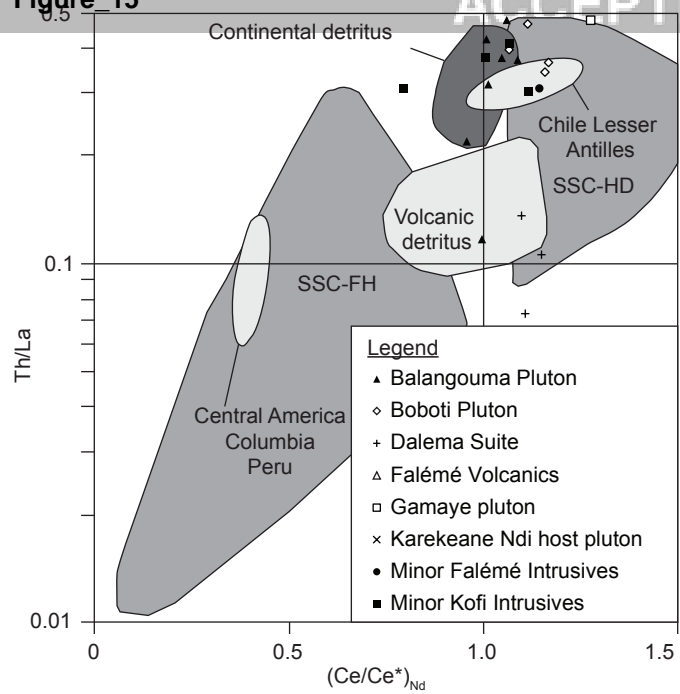




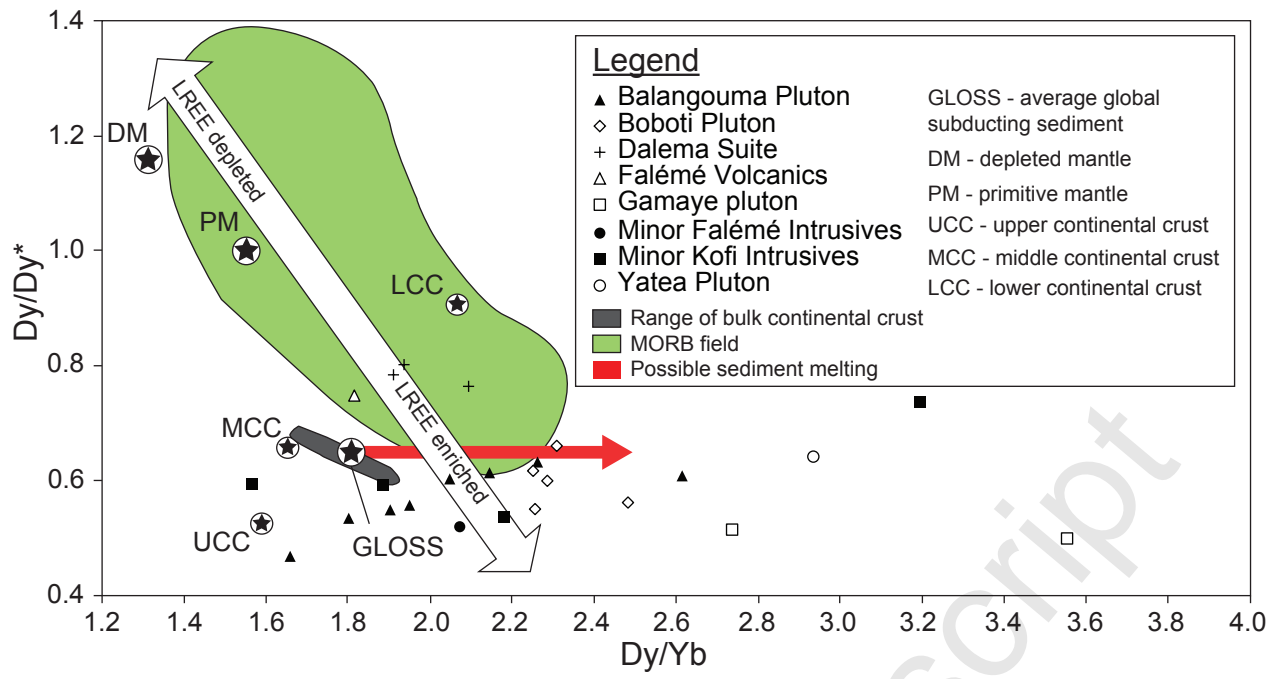


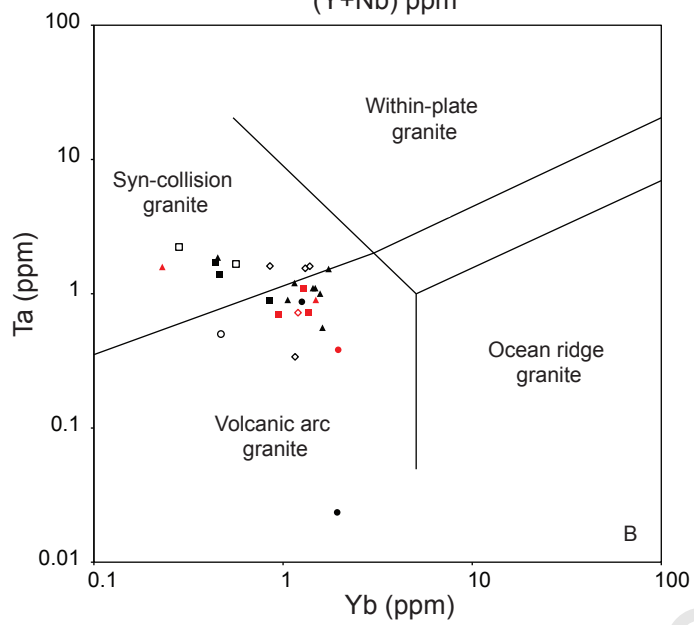
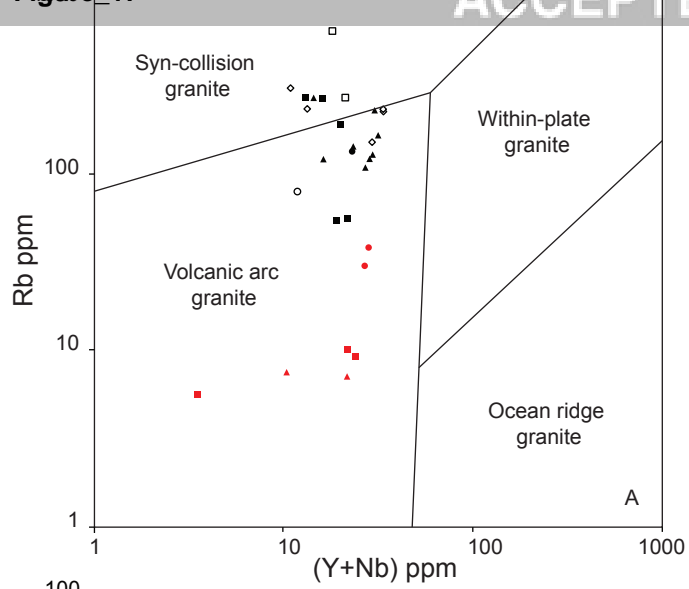






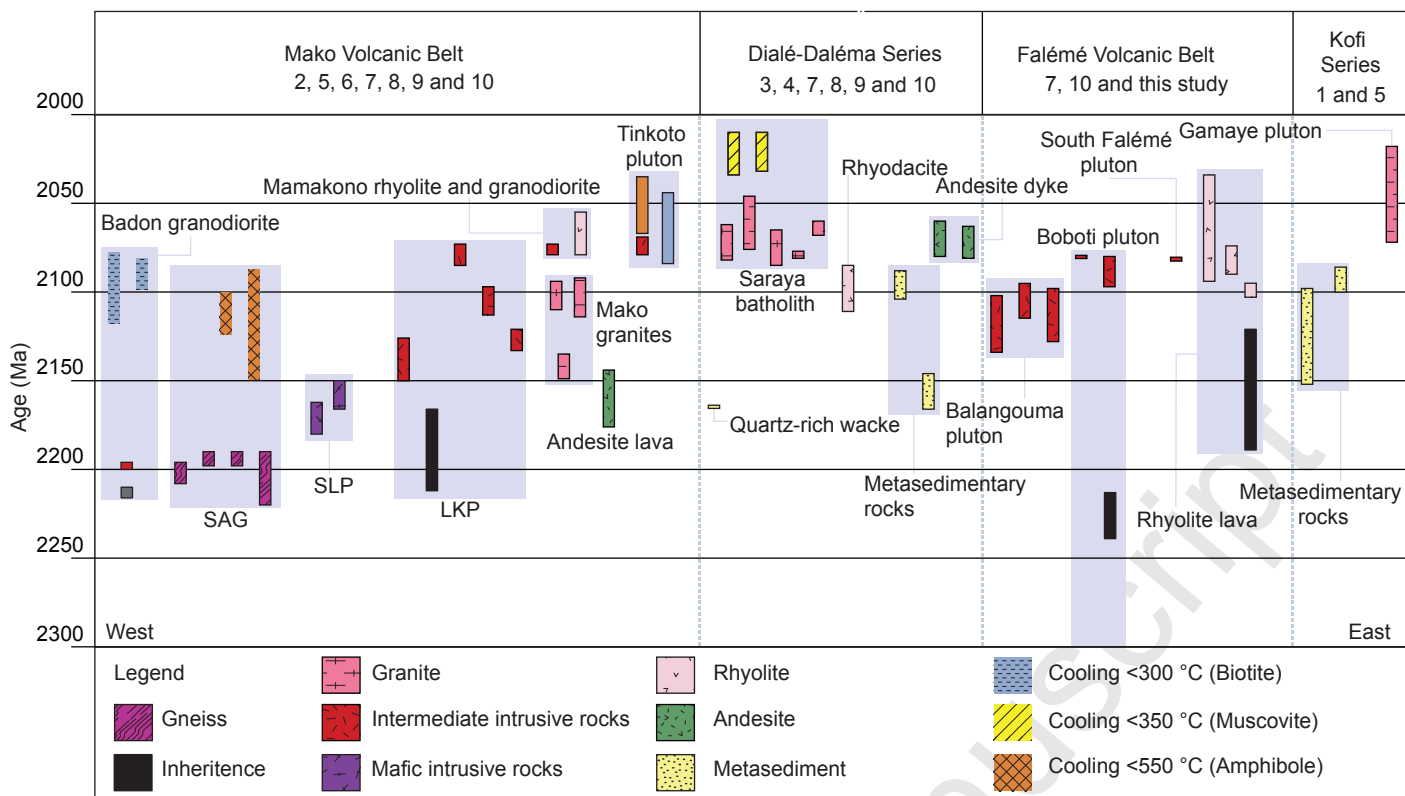
ACCEPTED MANUSCRIPT

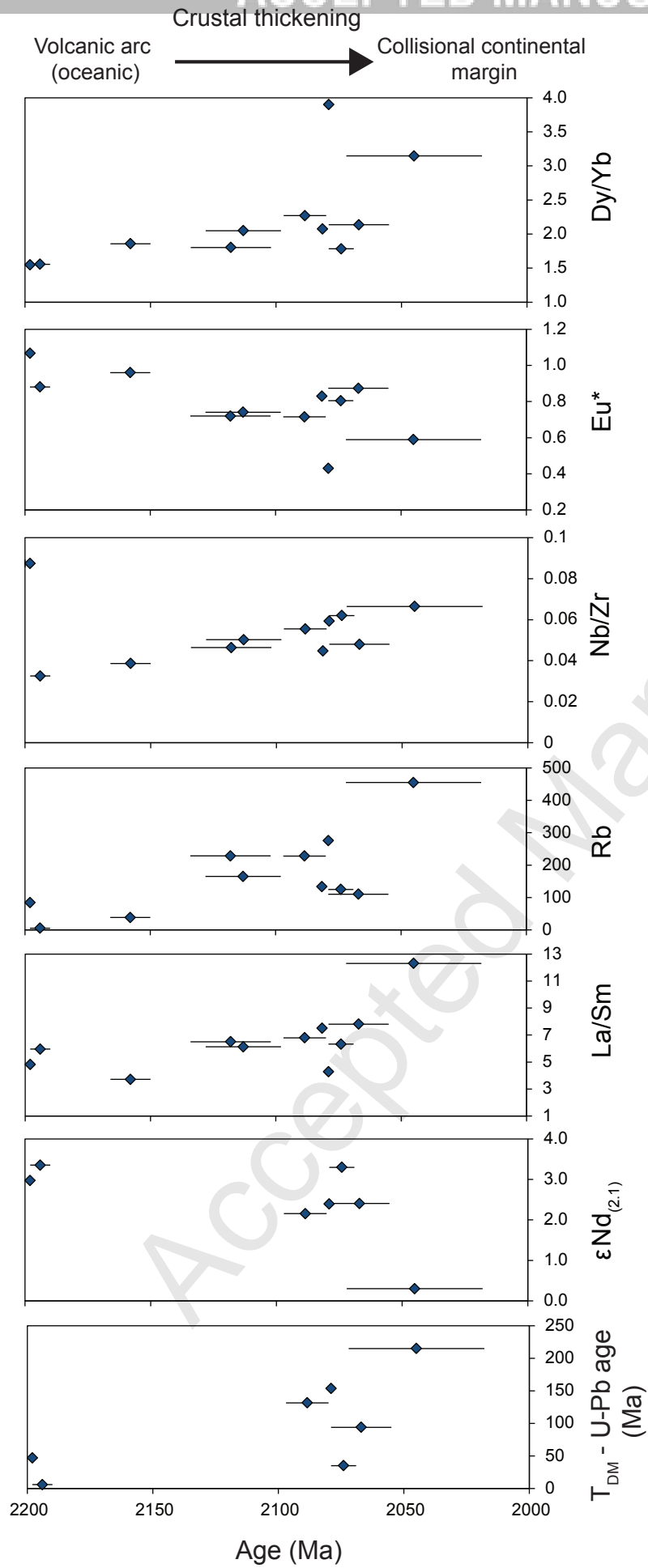




**Legend**

- |                     |                           |
|---------------------|---------------------------|
| ▲ Balangouma Pluton | ● Minor Falémé Intrusives |
| ◇ Boboti Pluton     | ■ Minor Kofi Intrusives   |
| □ Gamaye pluton     | ○ Yatea Pluton            |







- Highlights
- New U-Pb age data indicate the Balangouma pluton crystallised at  $2112 \pm 13$  Ma.
- Inherited zircons indicate magmatic activity in the Falémé Belt at  $2226 \pm 13$  Ma.
- The KKI evolved from a volcanic island arc environment to an active continental margin.
- Crustal thickening generated peraluminous, granitic melts with a crustal component.
- The Daléma igneous rocks may have formed in an extensional back arc setting.

Accepted Manuscript